

MULTIFERROIC DEVICES: MODELING, ANALYSIS, AND APPLICATIONS

by

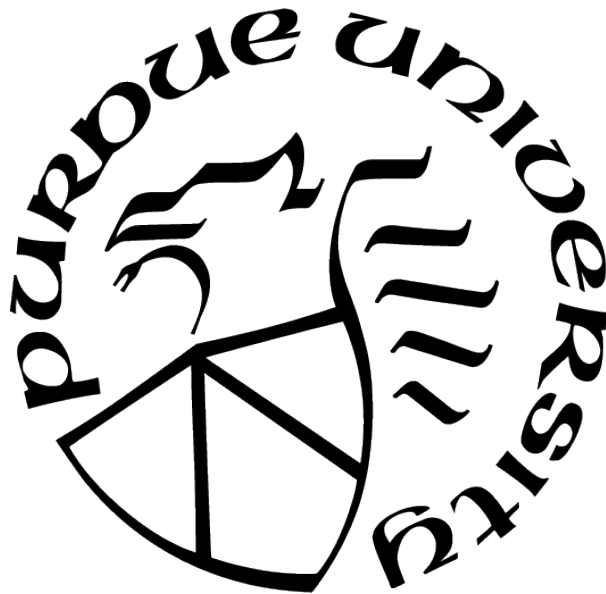
Robert Andrawis

A Dissertation

Submitted to the Faculty of Purdue University

In Partial Fulfillment of the Requirements for the degree of

Doctor of Philosophy



School of Electrical and Computer Engineering

West Lafayette, Indiana

December 2020

**THE PURDUE UNIVERSITY GRADUATE SCHOOL
STATEMENT OF COMMITTEE APPROVAL**

Dr. Kaushik Roy, Chair

School of Electrical and Computer Engineering

Dr. Anand Raghunathan

School of Electrical and Computer Engineering

Dr. Byunghoo Jung

School of Electrical and Computer Engineering

Dr. Sumeet Gupta

School of Electrical and Computer Engineering

Approved by:

Dr. Dimitrios Peroulis

To my parents and my wife.

ACKNOWLEDGMENTS

I want to thank my advisor Professor Kaushik Roy. His guidance was the light in my way. I am grateful to have him as my advisor. He has always been supportive. I learned a lot from him not only on the scientific side but also on the personal level.

I want to thank my doctoral dissertation committee: Professor Anand Raghunathan, Professor Byunghoo Jung, and Professor Sumeet Gupta. Their guidance and feedback were valuable and essential to improve my research. Professor Sumeet Gupta has always been willing to dedicate time to answer my questions.

I want to thank Professor Amir Atiya. He was the one that encouraged me to join Purdue University and start my Ph.D. journey. He was my master's degree advisor at Cairo University. He is a great scientist and a dedicated educator. I want to thank Dr. Akhilesh Jaiswal, for guiding me at the beginning of my Ph.D. journey.

The research was funded in part by C-BRIC, one of six centers in JUMP, a Semiconductor Research Corporation (SRC) program sponsored by DARPA, the National Science Foundation, Intel Corporation and Vannevar Bush Faculty Fellowship.

TABLE OF CONTENTS

LIST OF TABLES	9
LIST OF FIGURES	10
ABSTRACT	15
1 INTRODUCTION	16
1.1 Multiferroic Tunnel Junctions	18
2 THE FIRST PRINCIPLE CALCULATIONS OF THE FM/FE INTERFACE . . .	23
2.1 Simulation Procedure and Parameters	24
2.2 DFT Simulation Results	27
3 MFTJS SIMULATION FRAMEWORK	28
3.1 The Magnetization Dynamics	28
3.1.1 The LLG Equation	29
3.1.2 The Effective Magnetic Field	29
3.1.3 The Thermal Fluctuations	30
3.1.4 The spin transfer torque	30
3.2 The Ferroelectric Dynamics	30
3.3 Quantum Transport: Non-equilibrium Green's Function modeling of MFTJ .	31
3.4 Time-dependent Formulation of Exchange interaction Coefficient based on Time-dependent Perturbation Theory	35
3.5 Simulation Procedure and Parameters selection	36

4	SIMULATION RESULTS AND ANALYSIS	39
4.1	Comparison with Experimental MFTJ Characteristics	39
4.2	Analysis of Various MFTJ Parameters	40
4.3	MFTJ Dynamic Characteristics	45
5	ANTIFERROELECTRIC TUNNEL JUNCTIONS AS ENERGY-EFFICIENT COU- PLED OSCILLATORS: MODELING, ANALYSIS, AND APPLICATION TO SOLV- ING COMBINATORIAL OPTIMIZATION PROBLEMS	48
5.1	AFTJ physics	50
5.1.1	The antiferroelectric dynamics	50
5.1.2	The electrostatic potential	52
5.1.3	Tunneling current	55
5.1.4	Simulation results and discussion	56
5.2	Biasing AFTJ as an Oscillator	59
5.3	AFTJ based coupled-oscillator network	63
5.4	The Approximate AFTJ Based coupled-oscillator network model	65
6	A NEW OSCILLATOR COUPLING FUNCTION FOR IMPROVING THE SO- LUTION OF GRAPH COLORING PROBLEM	71
6.1	Stability analysis	77
6.2	Simulation Results and Discussion	78
7	PROPOSAL FOR AN AREA-EFFICIENT NON-VOLATILE FLIP-FLOP BASED ON SPIN HALL EFFECT	83

7.1	The SHE-MTJ Device	85
7.2	The Proposed SHE-MTJ based NVFF	87
7.2.1	Normal operation	87
7.2.2	Backup operation	88
7.2.3	Restore operation	88
7.2.4	Results and analysis	89
8	FUNCTIONAL READ ENABLING IN-MEMORY COMPUTATIONS IN 1TRAN- SISTOR - 1RESISTOR MEMORY ARRAYS	92
8.1	Proposed Sensing Scheme for Bit-wise In-Memory operations	93
8.1.1	Simultaneous Row Activation	93
8.1.2	Proposed Staggered Memory Cell Activation	97
8.2	Simulation Results and Discussions	98
9	DESIGN AND COMPARATIVE ANALYSIS OF SPINTRONIC MEMORIES BASED ON CURRENT AND VOLTAGE DRIVEN SWITCHING	106
9.1	Coupled model for magnetization dynamics and electron transport	111
9.2	Study overview	114
9.3	PMA and IMA based bit-cells	116
9.4	VCMA based bit-cells	118
9.5	SHE based memory	122
9.6	ME based memory	124
9.7	Sense amplifier	127

9.8	Results and analysis	128
9.8.1	Write Power and Bit-Cell area	128
9.8.2	Read Performance	131
9.8.3	Sense Amplifier and Read Energy	135
10	SUMMARY	137
	REFERENCES	140
	VITA	156

LIST OF TABLES

5.1	The list of the parameters values used for AFTJ simulations.	60
5.2	A comparison of different emerging oscillators with respect to power, area and frequency.	62
5.3	The results of the reduced model for practical graph coloring problem.	70
6.1	The results of the proposed model compared to the Kuramoto model.	82
7.1	The summary of the simulations results.	90
9.1	Parameters used in s-LLGs simulations.	116
9.2	Summary of the bit-cells write bias. The VCMA has two voltage pulses P1 and P2.	121

LIST OF FIGURES

1.1	The layer structure of MTJ, FTJ, and MFTJ.	18
1.2	The electrostatics of different tunnel junctions. (a) The electrostatic potential and density of states of MTJ. (b) The charge and electrostatic potential of FTJ. (c) The electrostatic potential and magnetization dependent density of states of MFTJ.	20
2.1	The atomic structure of LAMO/BTO interface that is used for supercell simulation. The structure consists of 4.5 unit cells of LAMO and 5.5 unit cells of BTO. The dependence of the magnetic configuration of LAMO on the electric polarization of BTO is illustrated. At the left interface, the second Mn site in LAMO exhibits AFM and <i>FM</i> alignment in case of positive and <i>negative</i> electric polarization of BTO, respectively.	24
2.2	The atomic structure of Co/BTO interface that is used for supercell simulation. The structure consists of 5.5 unit cells of BTO and 4.5 unit cells of Co. The Co magnetization exhibits constant magnetization independent of the electric polarization of BTO.	25
2.3	The atomistic and macroscopic potential of LAMO/BTO structure.	26
2.4	The atomistic and macroscopic potential of Co/BTO structure.	26
3.1	The MFTJ structure with the spin based NEGF meshing projected. The Hamiltonian definitions along with magnetization directions and DOS. . . .	32
3.2	The self-consistent simulation procedure.	36
4.1	The current of LSMO-LCMO-BTO-LSMO MFTJ is illustrated at different applied bias voltages V_a for the four MFTJ states. The experimental data for the same device is demonstrated in [11]. The simulation parameters are $m_{ch}^* = 0.8m_0$, $m_L^* = 0.9m_0$, $m_R^* = 0.9m_0$, m_0 is the free electron mass, $\mu_L = 3$ eV, $\mu_R = 3$ eV, $\Delta_L = 2.4$, $\Delta_R = 2.4$ eV, $U_B = 3.1$ eV, $\phi_{BI} = 1$ eV, $t_{FE} = 2$ nm, $T = 80K$ [11], and the MFTJ radius is $8.5 \mu m$. The screening lengths of the electrodes used in NEGF simulation are estimated by DFT, as illustrated in section 2.	40
4.2	The current of LSMO/BTO/Co FTJ is illustrated at different applied bias voltages V_a . The experimental data for the same device is demonstrated in [5]. The simulation parameters are $m_{ch}^* = 0.8m_0$, $m_L^* = 0.9m_0$, $m_R^* = 2m_0$, $\mu_L = 3$ eV, $\mu_R = 2.9$ eV, $\Delta_L = 2.4$, $\Delta_R = 1.8$ eV, $U_B = 3.16$ eV, $\phi_{BI} = 1.2$ eV, $t_{FE} = 3$ nm, m_0 is the free electron mass, $T = 300K$ [23], and the FTJ radius is 350 nm. The screening lengths of the electrodes used in NEGF simulation are estimated by DFT, as illustrated in section 2.	41
4.3	The resistance of LSMO/LCMO/BTO/LSMO MFTJ is illustrated under the effect of external magnetic field.	42

4.4	The TER of the MFTJ as a function of splitting energy Δ_L	42
4.5	The TER as a function of the built-in potential ϕ_{BI}	43
4.6	The TER of the MFTJ as a function of the screening lengths ratio δ_1/δ_2 . . .	44
4.7	The current and TER of the MFTJ as a function of barrier height U_B	44
4.8	The electric polarization, the transition probability $ a(t) ^2$ and the z component of the magnetization of the second Mn atom away from the LAMO/BTO interface.	46
4.9	The current of the MFTJ as a function of time.	46
5.1	The electric polarization of antiferroelectric material.	51
5.2	The layered structure of AFTJ and the electrostatic potential at different states of electric polarization.	53
5.3	The electrostatic potential at $P = 0$ and $P < 0$. For the case of $P = 0$, the red triangular is added and the green one is subtracted. In the case of $P < 0$, the red triangular is subtracted and the green one is added. (a) Direct tunneling in both polarization states. (b) Direct tunneling in case of $P = 0$ and Fowler-Nordheim in case of $P < 0$. (C) Fowler-Nordheim tunneling current dominates in both polarization states.	57
5.4	The simulation results and the experimental I-V characteristics of the AFTJ. The experimental I-V characteristic are published by M. Alexe <i>et al</i> [61]. . .	59
5.5	The AFTJ based coupled-oscillator network.	61
5.6	The AFTJ and the transistor M_1 I-V characteristics at different values of the bifurcation parameter. (a) The system has a single closed loop. (b) The system has two different cyclic paths ACD and ACB'. (c) The system has one stable fixed point.	62
5.7	The hspice circuit simulation results for simple graph coloring problem using AFTJ based coupled-oscillator network. (a) Fully connected graph of three nodes. (b) Sparse graph of four nodes. (c) Fully connected graph of four nodes. .	64
5.8	Sparse pairwise connected graph of eight nodes. (a) The coupled-oscillator network solution of the coloring problem. (b) The coupled-oscillator network solution of the same problem with extra virtual node is added to the graph. .	66
5.9	(a) Graph connections of myciel3. (b) AFTJ based coupled-oscillator simulation result for the graph myciel3.	67
5.10	The approximate coupled-oscillator model. The AFTJ is replaced by an average resistance r_l and r_h for the low and high resistance states, respectively. .	68
5.11	The myciel5 and queen6_6 graphs contain 47 nodes and 36 nodes, respectively. .	69

6.1	The final oscillator density (6.4) relative to a frame of reference is rotating with angular velocity ω	73
6.2	The oscillator density function and the coupling function. (a) Even coupling function. (b) Odd coupling function.	76
6.3	The graph coloring results for QUEEN8 that contains 64 nodes, 728 edges, and chromatic number of 9 colors. The parameters used are the same for both results. (a) The Kuramoto model has no clear separation between classes. (b) The proposed model has a clear 9 distinct classes.	79
6.4	The simulation results of the graph myciel3. (a) The results of the proposed coupling function where $C_{ik} = 0$ for unconnected nodes and $C_{ik} = -16$ for connected nodes. (b) The results of the Kuramoto model where $C_{ik} = 23$ for unconnected nodes and $C_{ik} = -16$ for connected nodes. (c) The results of the Kuramoto model where $C_{ik} = 24$ for unconnected nodes and $C_{ik} = -16$ for the connected nodes.	81
7.1	The proposed circuit of the NVFF. The SHE-MTJ is included as inset. The V_{dd} is 1.1 V.	86
7.2	(a) The time diagram of the backup operation of '0' and '1'. The diagram is the result of 1000 samples of Monte Carlo simulations. (b) The time diagram of the restore operation of '0' and '1'. The diagram is the result of 1000 samples Hspice Monte Carlo simulations.	87
8.1	The circuit schematic of simultaneous memory activation scheme.	94
8.2	The time diagram of simultaneous memory activation schema that is simulated by Hspice Monte Carlo for 1000 samples.	95
8.3	The circuit schematic of staggered memory activation schema.	96
8.4	The time diagram of staggered memory activation schema for '01' simulated by Hspice Monte Carlo for 1000 samples. The charge sharing and charge injection happen due to switching off the transmission gates are marked by the green oval.	100
8.5	The time diagram of staggered memory activation schema for '00' simulated by Hspice Monte Carlo for 1000 samples. The charge sharing and charge injection happen due to switching off the transmission gates are marked by the green oval.	101
8.6	The number of failing cases for staggered and simultaneous memory activation schemes as a function of different ON-OFF resistance ratios $25^{\circ}C$	102
8.7	The number of failing cases for staggered and simultaneous memory activation schemes at $50^{\circ}C$	103
8.8	The number of failing cases for staggered and simultaneous memory activation schemes at 10% lower supply voltage.	104

8.9	The distribution of the threshold voltage variations and the voltage input of the transistor M1.	104
8.10	The distribution of the threshold voltage variations and the voltage input of the transistor M2.	105
9.1	The energy as function of the angle θ between the pinned layer and free layer magnetization.	109
9.2	The density of states of MTJ in the case of the parallel alignment of magnetization and antiparallel alignment of magnetization.	110
9.3	The schematic of 1T-1MTJ bit-cell at writing logic '0' and writing logic '1'. The source degeneration problem happens in the case of write '1' (switching to antiparallel state).	112
9.6	The overview of the study flow and the criterion of selecting the device parameters.	116
9.7	The magnetization trajectory of the PMA and IMA. The starting point is marked by the green plus sign, and the end point is marked by a red circle. The parameters used in this calculations are listed in Table 9.1.	118
9.8	The layout of the 1T-1MTJ bit-cell. The width is 2 metal line limited of 12λ . The total area is $48F^2$	118
9.9	The VCMA write operation [134]. (a) The magnetization trajectory of the VCMA write mechanism. The blue line is the VCMA dominated phase. The green line is the STT dominated phase. (b) The supply voltage during the VCMA and STT dominated pulses.	120
9.10	The schematic of SHE based MTJ stack and the schematic of SHE based memory bit-cell.	123
9.11	The layout of SHE based memory bit-cell. The total area is $66 F^2$	123
9.12	ME based memory bit-cell with the read and write paths are annotated on ME stack.	125
9.13	The magnetization trajectory of ME based memory. The start and end points are marked by the green plus sign and red circle, respectively. The parameters used for this simulation is listed in Table 9.1.	126
9.14	The schematic diagram of the differential voltage sense amplifier.	128
9.15	The simulation waveform of the differential voltage sense amplifier in case of $C1 \gg C2$. The simulation is done using SPICE. The OUT1 and OUT2 have the correct read output.	129
9.16	The average write power and layout area for the various bit-cells in units of (F^2).	130

9.17	The TMR ratio for single fin and single IMA based MTJ versus oxide thickness at a constant supply voltage of 0.25 V. The time constant of the memory cell assuming 25 fF column metal line capacitance is plotted on the secondary axis.	132
9.18	The CTMR ratio of a single fin and single IMA based MTJ versus oxide thickness at constant supply voltage of 0.25 V.	132
9.19	The RDM, and CTMR ratios calculated with RDM is kept limited between 50-60%.	133
9.20	The parallel and antiparallel read current difference for single fin and single IMA based MTJ versus oxide thickness at constant supply voltage 0.25 V. .	134
9.21	The parallel and antiparallel read current difference, the input voltage of the differential voltage sense amplifier, and the average read energy per single bit read using the differential voltage sense amplifier at constant RDM of 50 – 60%.	134

ABSTRACT

Recently, multiferroic-based devices have gained significant spotlight in the literature due to its non-volatility and high on/off current ratio. In order to analyze such devices and to have an insightful understanding of their characteristics, there is a need for developing a multi-physics modeling and simulation framework. The simulation framework discussed in this study is motivated by the scarcity of such multi-physics studies in the literature. In this thesis, a theoretical analysis of multiferroic tunnel junctions (MFTJs) is demonstrated using self-consistent analysis of spin-based non-equilibrium Green's function (NEGF) method to estimate the tunneling current, Landau-Khalatnikov (LK) equation to model the ferroelectric polarization dynamics, together with Landau-Lifshitz-Gilbert's (LLG) equations to capture the magnetization dynamics. The spin-based NEGF method is equipped with a magnetization dependent Hamiltonian that eases the modeling of the tunneling electro-resistance (TER), tunneling magneto-resistance (TMR), and the magnetoelectric effect (ME) in MFTJs. Moreover, we apply the first principle calculations to estimate the screening lengths of the MFTJ electrodes that are necessary for the estimation of tunneling current. These multiferroic-based devices show significant performance improvement in many applications. In this study, we demonstrate the use of these multiferroic-based devices for in-memory computing and combinatorial optimization problems. The simulation results of these applications show significant performance improvement compared to conventional computing schema.

1. INTRODUCTION

Over the last few decades, the complementary metal-oxide-semiconductor (CMOS) technology has been continuously downscaled following Moore’s law [1]. However, the static power dissipation and the threshold voltage variations of downscaled short channel transistor have become dominating factors that limit the static random access memory (SRAM) performance [2]–[4]. Consequently, the high static power dissipation of SRAM inspired the exploration of alternative memory technologies like spin transfer torque magnetic memory (STT-MRAM). However, the limited tunneling magneto-resistance (TMR) of magnetic tunnel junction (MTJ) together with the threshold voltage fluctuations of the short channel access transistor affect the STT-MRAM read error rate. Therefore, the read performance of STT-MRAM has become a fundamental limiting factor in its applicability. Consequently, a new family of tunnel junctions, called ferroelectric tunnel junctions (FTJs), have emerged in literature [5]–[7].

An FTJ consists of a ferroelectric insulator sandwiched between two different metal electrodes, as illustrated in Fig. 1.1. The information is stored in the electric polarization of the insulator. The FTJ resistance is a function of the electric polarization of the insulator. The electric polarization of the ferroelectric insulator modulates the FTJ resistance, and hence the information can be extracted by sensing the FTJ resistance. The tunneling electro-resistance (TER) of FTJ is defined as $TER = \frac{|R_{\rightarrow} - R_{\leftarrow}|}{\min(R_{\rightarrow}, R_{\leftarrow})}$, where R_{\rightarrow} and R_{\leftarrow} are the resistance of positive and negative electric polarization states, respectively [8]. The physical origin of TER is discussed in detail in section 1.1. The charge current of FTJ consists of three main components: Fowler–Nordheim tunneling, direct tunneling, and thermionic emission [9].

On the other hand, the multiferroic tunnel junctions (MFTJ) is a nonvolatile tunnel junction that consists of two ferromagnetic layers separated by a ferroelectric insulator, as illustrated in Fig. 1.1. Intuitively, from the structure of an MFTJ, we can predict that an MFTJ combines the resistive switching mechanism of FTJ and MTJ to constitute a four-state device. However, it turns out that the MFTJ has more advantages over its constituent devices due to the magnetoelectric effect (ME). The ME effect at the FM/FE interface

is observed in LaSrMnO₃(LSMO)-LaCaMnO₃(LCMO)-BaTiO₃(BTO)-LSMO MFTJ [9]. It originates from the modulation of the screening charges at the LCMO side by the bound charges at the BTO interface. The change in the electron concentration at the LCMO interface affects the LCMO magnetic configuration. The magnetic alignment of the LCMO layer is switched from the ferromagnetic (FM) to the antiferromagnetic (AFM) alignment due to the change in electron concentration [10], [11]. The transition to the AFM alignment shifts the density of states (DOS) of the majority spin carriers to higher energy levels, and hence limits the majority spin current. In brief, the overall influence of the ME effect is to improve the TER ratio, as explained in detail in section 1.1 and section 2.

A detailed review of the state of the art in FTJs and MFTJs could be found in [6], [7]. However, a brief review of the progress in FTJs and MFTJs literature is provided in the following discussion. Although the FTJ has been predicted by Esaki *et al.* [8] in 1971 with the name "polar switch", the FTJ has not been realized until recently. The lack of the knowledge of fabrication techniques of ferroelectric ultra-thin films had prevented the FTJ realization. However, due to the breakthrough that has been achieved by Zembilgotov *et al.* [12], the ferroelectric ultra-thin film has been realized followed by many other experimental studies [13], [14]. Zhuravlev *et al.* [15], [16] have explained the dependence of the barrier height on electric polarization with the help of Thomas-Fermi equation and Landau tunneling current formula [17]. The Wenzel-Kramer-Brillouin (WKB) approximation and one-band model [17]–[19] have been used to calculate the tunneling current through the FE insulator in [20]. Hinsche *et al.* have used Landauer-Büttiker formula and the WKB approximation together with *ab initio* calculation to model the FTJ characteristics [21]. Fechner *et al.* have used the *ab initio* method to study the electric polarization dependent phase transition in Fe/ATiO₃ interface [22]. On the other hand, the non-equilibrium Green's function (NEGF) method along with Landau-Khalatnikov (LK) equation have been used to estimate the FTJ I-V characteristics in [23]. However, the study did not consider the magnetization dynamics or the Hamiltonian dependence on the magnetization.

To conclude, the scarcity of multi-physics simulation studies that capture the MFTJ magnetization dynamics, along with TMR, and TER effects motivates the modeling and simulation framework applied in this study. In this study, the spin-based NEGF is applied

to model the tunneling current, along with Landau-Lifshitz-Gilbert's (LLG) equation are applied to model the magnetization dynamics, and the LK equation is applied to describe the FE motion [24]. However, the accuracy of these models depends on the parameters used to model various materials. We use the density functional theory (DFT) to estimate the electrostatic potential, and hence the screening lengths of the electrode that are used in the NEGF transport simulations. The simulation results are compared to experimental results of the MFTJ in [5], [11] to confirm the validity of the method.

The quantum transport model adopted by this study is based on the mean field approximation. In addition, the proposed model is based on single-band effective mass approximation of the complex band structure of the material. A detailed discussion of the advantages and limitations of the adopted quantum transport model could be found in [25]. However, the effective mass approximation is a computationally efficient method compared to other computationally intensive methods that account for the complex band structure of the material. The self-consistent solution of the magnetization dynamics, electric polarization, and quantum transport requires thousands of evaluations of the quantum transport model.

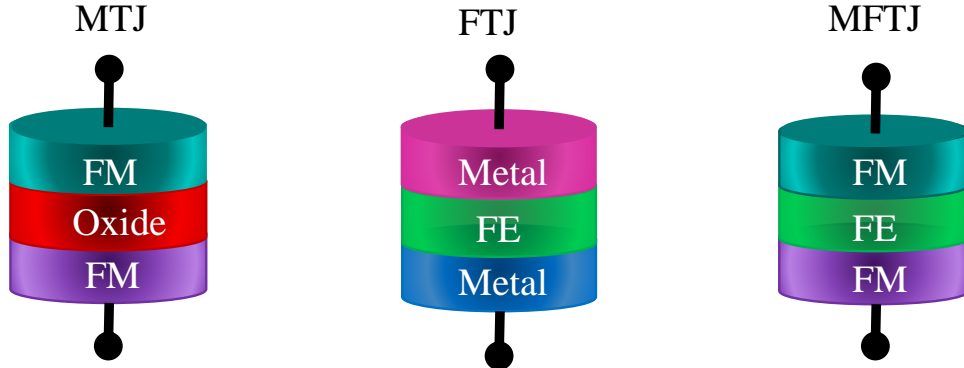


Figure 1.1. The layer structure of MTJ, FTJ, and MFTJ.

1.1 Multiferroic Tunnel Junctions

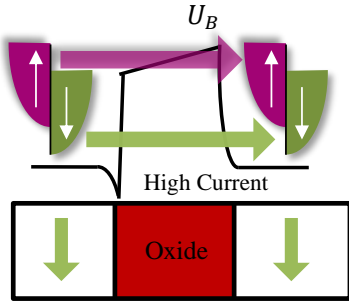
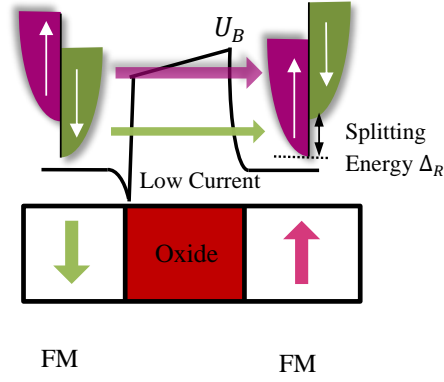
The MFTJ structure combines the FM electrodes of MTJ together with the FE insulator of FTJ to produce a four-state device. We start by explaining the TMR effect in the MTJ along with the TER effect in FTJ before describing the MFTJ characteristics. Furthermore,

the ME effect at the FM/FE interface is a unique property of MFTJs that enhances the TER effect, as explained in detail in this section and in section 2.

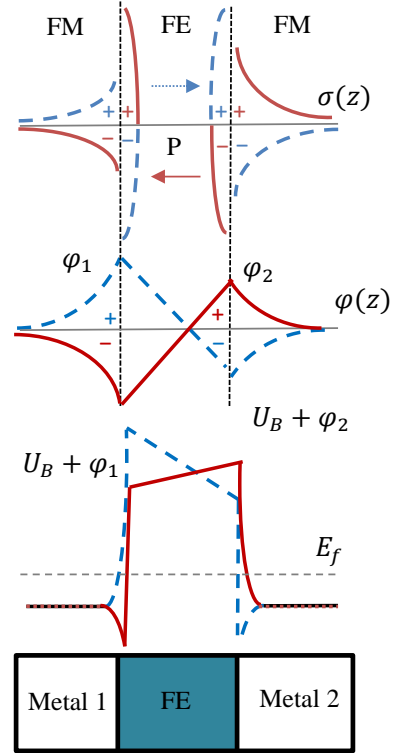
The TMR effect could be explained in the light of spin dependent transport illustrated in Fig. 1.2 [26]–[28]. In such FM materials, the lower band of the density of states (DOS) of the majority and minority spin carriers have energy shift, as illustrated in Fig. 1.2 (a). The energy splitting is dependent on the magnetization direction. Therefore, in the case of anti-parallel alignment of the electrode magnetization, the majority spin carriers that migrate from the left electrode are restricted by the shortage of matched spin states at the right electrode. Consequently, the overall charge current is reduced in the case of anti-parallel alignment of the electrode magnetization. In the case of parallel alignment of the magnetization, the majority and minority spin carriers migrate from the left electrode and are absorbed by the matched spin states that are sufficiently available at the right electrode. Consequently, the overall charge current is not limited by the availability of the spin states in the case of parallel alignment of magnetization. In other words, the MTJ resistance changes according to the magnetization alignment of the electrodes that control the DOS energy splitting between the majority and the minority spin carriers. Finally, the TMR is defined as $TMR = \frac{R_{AP}-R_P}{R_P}$, where R_{AP} is the resistance of anti-parallel aligned magnetization state, and R_P is the resistance of parallel aligned magnetization state [26].

The TER effect of FTJ could be explained by the help of charge screening phenomena in the metal electrode [15]. The electric polarization of FE insulator induces bound charges at the metal/FE interface. The bound charges are partially screened by the free electron gas in the metal side, as illustrated in Fig. 1.2 (b). The uncompensated charges at the interface result in a constant electric field inside the insulator, and hence linear potential. Moreover, the polarization direction controls the polarity of the bound charge, and hence the polarity of the potential drop in the FE insulator ($\phi_1 - \phi_2$), where ϕ_1 and ϕ_2 are the potential at the left and right metal/FE interfaces, respectively. Therefore, the barrier height increases by $|\phi_1 + \phi_2|$ in the case of positive electric polarization. In contrast, the barrier height is reduced by $|\phi_1 + \phi_2|$ in the case of negative electric polarization. Finally, the large TER value of FTJ is a natural result of the exponential dependence of tunneling current on the barrier height. The asymmetry of the electrodes screening lengths is an important factor for

(a) MTJ



(b) FTJ



(c) MFTJ

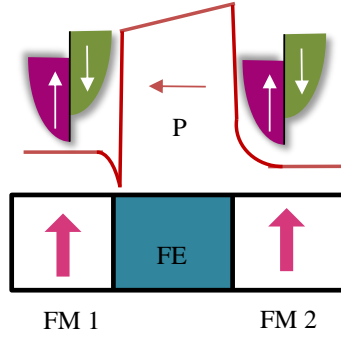
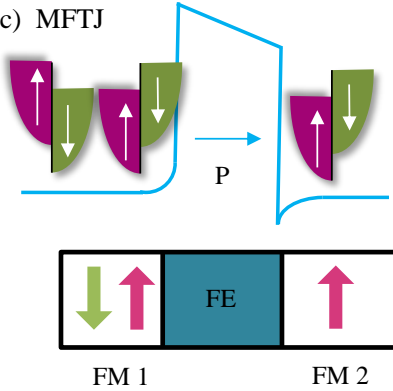


Figure 1.2. The electrostatics of different tunnel junctions. (a) The electrostatic potential and density of states of MTJ. (b) The charge and electrostatic potential of FTJ. (c) The electrostatic potential and magnetization dependent density of states of MFTJ.

MFTJs to exhibit a nonzero TER. It is important to mention that the TER also depends on

the barrier effective thickness, which can change upon the polarization reversal due to the change from the insulating to metal phase, and both interface terminations [29], [30].

The aforementioned qualitative discussion could be formulated quantitatively, as illustrated in [15]. The screening charges and potential distribution in the metal side is described by the Thomas-Fermi formalism:

$$\phi(z) = \begin{cases} \frac{\sigma_s \delta_1}{\epsilon_0 \epsilon_{r1}} e^{-\frac{|z|}{\delta_1}} & z \leq 0 \\ -\frac{\sigma_s \delta_2}{\epsilon_0 \epsilon_{r2}} e^{-\frac{|z-d|}{\delta_2}} & z > 0, \end{cases} \quad (1.1)$$

where ϕ is the electrostatic potential, σ_s is the surface charge density of free charges, ϵ_0 is permittivity of free space, ϵ_{r1} (ϵ_{r2}) is the permittivity of the first (second) electrode, and δ_1 (δ_2) is the screening length of first (second) electrode. According to Thomas-Fermi relation, the charge and the potential of any point in the electrodes decrease as an exponential function of the distance between the point and the interface. Moreover, the potential values at the interface are defined as $\phi_1 = \frac{\sigma_s \delta_1}{\epsilon_0 \epsilon_{r2}}$ and $\phi_2 = \frac{-\sigma_s \delta_2}{\epsilon_0 \epsilon_{r2}}$. By applying the Gauss's law at the metal/FE interface, we get the expression

$$E_{FE} = \frac{(\sigma_s - P)}{\epsilon_0}, \quad (1.2)$$

where P is the polarization vector and E_{FE} is the electric field in the FE layer. The potential drop $\phi_1 - \phi_2$ is equal to the constant electric field inside the FE insulator multiplied by t_{FE} as given by

$$\frac{\sigma_s \delta_1}{\epsilon_0 \epsilon_{r1}} + \frac{\sigma_s \delta_1}{\epsilon_0 \epsilon_{r2}} + E_{FE} t_{FE} = 0. \quad (1.3)$$

Finally, from (1.2) and (1.3), the σ_s that satisfies the continuity of the potential at the interface is defined as

$$\sigma_s = \frac{P t_{FE}}{\frac{\delta_1}{\epsilon_{r1}} + \frac{\delta_2}{\epsilon_{r2}} + t_{FE}}. \quad (1.4)$$

However, for the limiting case of $t_{FE} \gg \frac{\delta_1}{\epsilon_{r1}} + \frac{\delta_2}{\epsilon_{r2}}$, the free charge density σ_s is equal to P , and hence the potential drop is zero which eliminates the TER effect [15]. Therefore, a mandatory constraint is imposed on the maximum FE thickness that maintains the TER effect. However, the stability of the ferroelectricity imposes a lower limit on the FE thickness. Therefore, the FE layer should have an optimal thickness that maintains the ferroelectricity and provides high TER ratio at the same time.

An MFTJ combines the TER effect of FTJ along with the TMR effect of MTJ to produce a four-state device as illustrated in Fig. 1.2 (c). However, it has been experimentally observed that the LCMO electrode of LSMO/LCMO/BTO/LSMO MFTJ [11] goes through phase transition from the FM state to the AFM phase by the influence of the electric polarization switching. To understand the effect of the FM to the AFM phase transition on the TER, let us assume that both electrodes have the magnetization in the positive z direction. In the case of *positive* electric polarization (*high resistance state*), the LCMO left electrode has an *AFM* configuration. The lower band of the DOS of the spin-up carriers shifts to higher energy levels. Therefore, the spin-up carriers that migrate from the right electrode are restricted by the shortage of spin-up states at the left electrode. Thus, the MFTJ *high resistance* increases, and hence the TER increases. In case of *negative* electric polarization (*low resistance state*), the LCMO has an *FM* configuration. The spin-up carriers that migrate from the right electrode are absorbed by the matched spin states without any restriction. Consequently, the overall TER of the MFTJ improves. The details and origin of this ME effect are explained in the following section.

2. THE FIRST PRINCIPLE CALCULATIONS OF THE FM/FE INTERFACE

Recently, many different forms of magnetoelectric effects have been observed in the literature such as electric field manipulated magnetization, electric field induced magnetic phase transition, and voltage controlled magnetic anisotropy [31]–[33]. In this study, we focus on the magnetoelectric effect that happens in the interface between $La_{1-x}A_xMnO_3/BaTiO_3$, where A is a divalent cation, i.e., Ca, Ba, and Sr and x is the chemical doping concentration. *LAMO*'s phase diagram exhibits a phase change between the ferromagnetic state and antiferromagnetic state as a function of hole carrier concentration x [34]. The transition between the FM and AFM phases and its dependence on hole concentration could be explained by the existence of two competing interactions that happen between the adjacent Mn sites in LAMO: superexchange interaction and double exchange interaction. In contrast to superexchange interaction that prefers AFM alignments, the double exchange interaction favors FM alignment [35]. The doping concentration x , modulates the density of electrons in Mn e_g orbitals that mediate the double exchange interaction. Note, the doping concentration supports one of the interactions over the other, and hence favors one of the configurations over the other.

The electrostatic doping created by electric polarization could change the electron concentrations similar to chemical doping [36]. Since the bound charges induced by electric polarization of BTO at the interface modulates the screening charges at the LAMO side, the electric polarization could control the magnetization phase transition similar to chemical doping. The magnetoelectric effect in LAMO/BTO interface is illustrated in Fig. 2.1. The second Mn site in LAMO exhibits AFM (*FM*) alignment in case of positive (*negative*) polarization state. However, the chemical doping concentration has to be fixed at the magnetic phase transition point ($x = 0.5$) between the FM and the AFM phases to facilitate the magnetic phase transition by electrostatic doping [37].

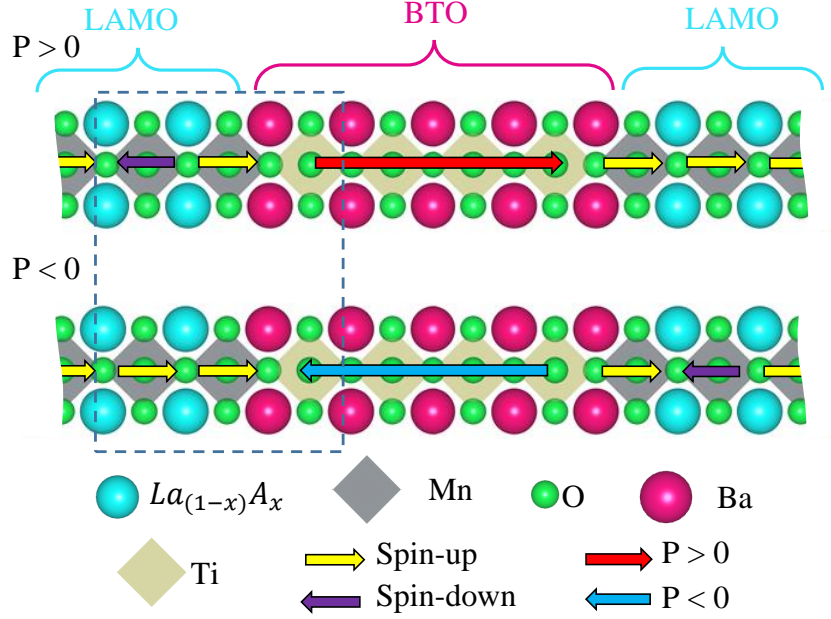


Figure 2.1. The atomic structure of LAMO/BTO interface that is used for supercell simulation. The structure consists of 4.5 unit cells of LAMO and 5.5 unit cells of BTO. The dependence of the magnetic configuration of LAMO on the electric polarization of BTO is illustrated. At the left interface, the second Mn site in LAMO exhibits AFM and *FM* alignment in case of positive and *negative* electric polarization of BTO, respectively.

2.1 Simulation Procedure and Parameters

We applied DFT method to extract the electrostatic potential profile of LAMO/BTO and Co/BTO structures. The screening lengths of LAMO and Co electrodes are estimated from the electrostatic potential. The generalized gradient approximation (GGA) method [38] implemented in Quantum-ESPRESSO package [39] is used to perform all of the DFT calculations in this study. The Vanderbilt's ultrasoft pseudopotential [40] is used along with virtual crystal approximation (VCA) [41] to handle the La-A doping. The VCA method is used by Burton *et al.* [10] to perform DFT calculations for typical structure with acceptable accuracy. The energy cutoff of 400 eV and Monkhorst-Pack grid of 12x12x1 of k-points are used for all the DFT simulations in this study.

The supercell used to simulate *LAMO/BTO* interface consists of 4.5 unit cells of LAMO and 5.5 unit cells of BTO, as illustrated in Fig. 2.1. The structure is stacked along (001)

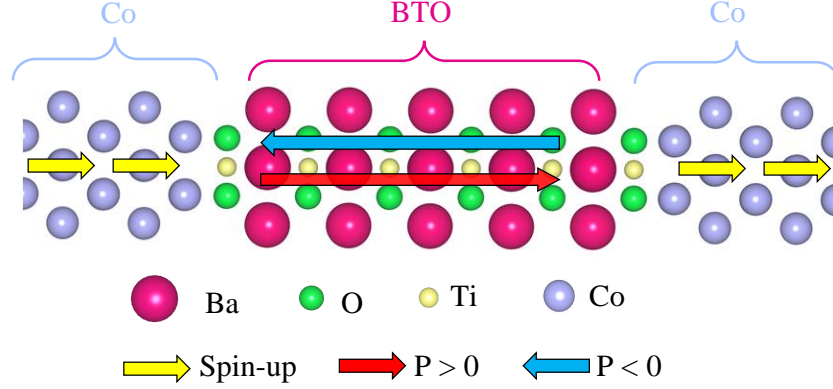


Figure 2.2. The atomic structure of Co/BTO interface that is used for supercell simulation. The structure consists of 5.5 unit cells of BTO and 4.5 unit cells of Co. The Co magnetization exhibits constant magnetization independent of the electric polarization of BTO.

direction of the perovskite cell. The stacking sequence at LAMO/BTO interface is $AO-BO_2$ [10]. The supercell illustrated in Fig. 2.2 is utilized to model the Co/BTO interface. The structure consists of 4.5 unit cells of Co and 5.5 unit cells BTO along (001) direction and is rotated 45° in the $x-y$ plane. The most stable interface has TiO_2 termination as described in [42]. We did not include any vacuum regions in these structures. As both structures are epitaxial growth on a $SrTiO_3$ substrate that has a bulk in-plane lattice constant of $a = 3.94\text{\AA}$, the lattice constant in the lateral direction is constrained to $a = 3.94\text{\AA}$ for all the layers of LAMO, Co and BTO. The lateral strain results in tetragonal distortion in the longitudinal direction (z direction). To estimate the tetragonal distortion, the DFT calculation of a single LAMO unit cell is repeated with different longitudinal lattice constants c . The lattice constant that has the minimum total energy is selected for further supercell simulations. The longitudinal lattice constant of LAMO that has minimum total energy is $c/a = 0.99$. Similarly, the longitudinal lattice constant of BTO and Co are estimated to be $c/a = 1.05$ and $c/a = 0.83$, respectively. Next, both supercells of LAMO/BTO and Co/BTO with the in-plane constraint and the corresponding tetragonal distortion are relaxed until the total force on the atoms is less than 10^{-3} Ryd/au . As the total force on the atoms reaches the limit of 10^{-3} Ryd/au , the atoms reach their equilibrium positions. Further optimization beyond this limit results in a negligible change in the positions of the atoms.

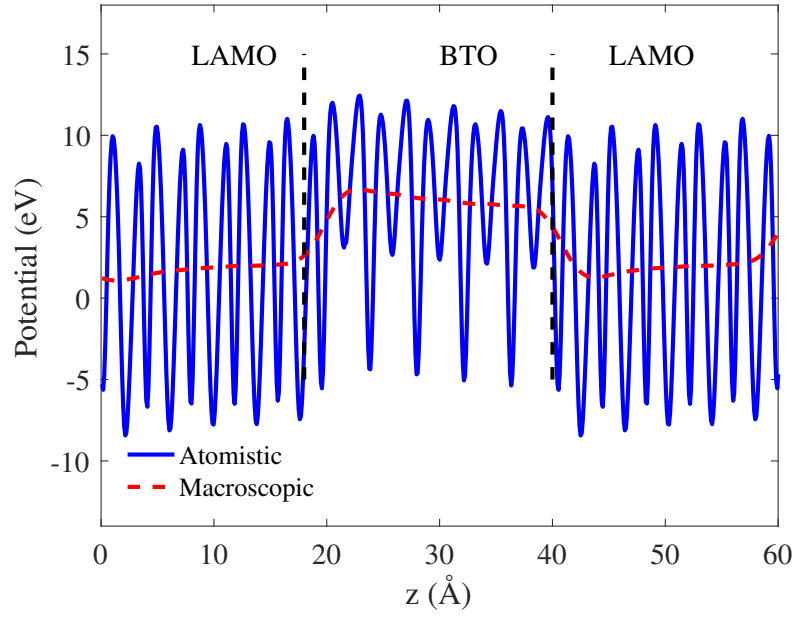


Figure 2.3. The atomistic and macroscopic potential of LAMO/BTO structure.

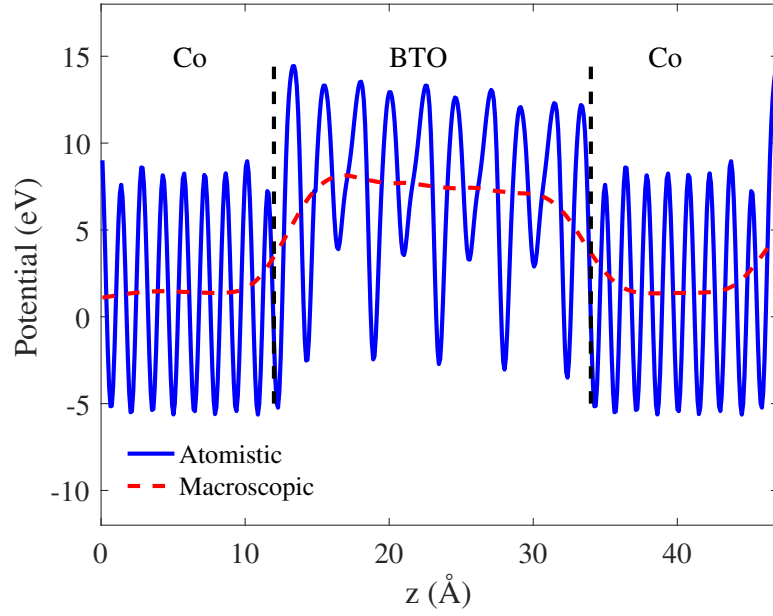


Figure 2.4. The atomistic and macroscopic potential of Co/BTO structure.

2.2 DFT Simulation Results

The magnetic configurations that minimize the total energy of the LAMO/BTO interface are illustrated in Fig. 2.1. The second Mn site in LAMO (left interface) exhibits AFM (*FM*) alignment in case of positive (*negative*) polarization state. The magnetic configuration of LAMO (left interface), that minimize the total energy, is AFM in the case of positive polarization and FM in the case of negative polarization [10]. The DFT simulation results for the magnetization of Mn sites are 2.57, -2.66, 2.76, 2.87, and 3.02 μ_B . In case of positive polarization state, the magnitude of the magnetization of the Mn atoms is lower at left interface and increases for the atoms away from that left interface [10]. In contrast, the magnetic configuration of the Co/BTO interface, that minimizes the total energy, is FM configuration independent of electric polarization of BTO. The Co/BTO interface exhibits a constant magnetic configuration independent of the electric polarization of BTO [42], as illustrated in Fig. 2.2. The DFT simulation result for the magnetization of bulk Co is 1.74 μ_B .

The atomistic electrostatic potential of LAMO/BTO and Co/BTO are illustrated in Fig. 2.3 and Fig. 2.4, respectively. The macroscopic potential is estimated from the atomistic potential by a moving window integral [41] and fitted by a spline function. Finally, the screening lengths $\delta/\epsilon_0\epsilon_r$ of $\text{La}_{0.7}\text{A}_{0.3}\text{MO}$, $\text{L}_{0.5}\text{A}_{0.5}\text{MO}$, and Co are estimated from electrostatic potential to be 1.06, 1.05, and 1.14 m^2/F , respectively. The estimated screening lengths are used in the spin dependent transport calculations, as explained in section 3.3.

3. MFTJS SIMULATION FRAMEWORK

3.1 The Magnetization Dynamics

The Landau-Lifshitz-Gilbert (LLG) equation formulates the precessional and damped motion of magnetization induced by the magnetic field and spin current [43], [44]. The single domain LLG equation is used along with NEGF self-consistently in many studies in literature. The single domain solution of LLG equation is not appropriate for LAMO. Because the LAMO material has atoms in the FM order and other atoms in the AFM order at the same time. Similarly, the solution of the magnetization as a continuum fails as well, because it requires a second order derivative of the magnetization with respect to space. The second order derivative appears in the definition of the exchange interaction effective field $H_{exch} = \frac{2A}{\mu_0 M_S} \frac{\partial^2 m}{\partial x^2}$, where A is a constant. However, the abrupt change of the magnetization at that atomistic scale makes the derivative with respect to space is not possible. The usual solution in case of AFM material is to replace the magnetization by the total magnetization $l = m_{j+1} + m_j$ and the AFM Neel field $n = m_{j+1} - m_j$ that are continuous variables in case of AFM material. However, LAMO has the FM and AFM orders that exist at the same time. The Neel field will be discontinuous at the area between the FM and the AFM phase.

We adopted a discrete multi-domain version of the LLG equation. The main difference between the continuum and discrete LLG equation is the definition of the exchange field. The definition of the exchange field in the discrete LLG equation does not require differentiation with respect to spatial coordinates. The discrete multi-domain LLG equation is similar to the atomistic LLG equation [45]. However, the discrete multi-domain LLG equation models the lateral direction as a single domain to reduce the computational effort. The lateral single domain assumption does not affect the accuracy of the method because the cross-section area of the junction is large enough to neglect the effect of edges. The discrete domains have a thickness equal to a single unit cell in the normal direction.

3.1.1 The LLG Equation

The LLG equation [45] can be expressed as

$$\frac{\partial m_i}{\partial \tau} = -m_i \times H_{eff,i} - \alpha m_i \times \frac{dm_i}{dt} + STT_i, \quad (3.1)$$

where m is a unit vector in direction of magnetization, τ is defined as $\tau = \frac{|\gamma|}{(1+\alpha^2)} dt$, t is the time, H_{eff} is the effective magnetic field, α is the Gilbert damping constant, γ is the gyro-magnetic ratio, i is index over the atoms along the x axis, and STT is the spin transfer torque. The first term of (3.1) is the precessional motion of the magnetization due to the effective magnetic field. The second term models the damped part of magnetization oscillation. The third term is the spin torque exerted by the spin current on the magnetization.

LAMO is modeled as a 1D chain of discrete domains with a magnetization variable m_i assigned to each domain. Each mesh cell has a length equal to the lattice constant and cross section area equals the total cross-section area of the MFTJ. In other words, we assumed that the MFTJ cross-section area is large enough. Therefore, we can neglect the effect of the boundary cell on the magnetization dynamics.

3.1.2 The Effective Magnetic Field

The effective magnetic field is given by

$$H_{eff,i} = H_{ext} + H_{therm} + H_{anis} + H_{exch,i}, \quad (3.2)$$

where H_{ext} is the external magnetic field, $H_{exch,i}$ is the exchange interaction effective field, H_{therm} models the random thermal variations, and H_{anis} is the magnetic anisotropy. The magnetic anisotropy is defined as $H_{anis} = \frac{2K_U}{M_S}$, where K_U is the anisotropy constant, and M_S is the saturation magnetization.

The exchange interaction field is defined as $H_{exch,i} = \frac{1}{\mu_0 M_S} \sum_j^N J'_{exch,i,j} m_j$ [45], where $J'_{exch,i,j}$ is the material magnetic exchange coefficient that is averaged by the FM to AFM transition probability as explained in section 3.4, and N is the number of nearest neighbors.

3.1.3 The Thermal Fluctuations

The random variation in the magnetization due to thermal excitations is modeled by the effective magnetic field H_{therm} defined as $H_{therm} = \zeta \sqrt{\frac{2\alpha KT}{|\gamma| M_S V_{cell} dt}}$, where K is Boltzmann's constant, T is the temperature, V_{cell} is the mesh cell volume that equals to the lattice constant multiplied by the total cross-section area of the MFTJ, dt is the numerical time step, and ζ is a vector with random components which are selected from standard normal distribution [46].

The thermal fluctuations term makes the LLG equation stochastic differential equation (SDE). The integration of the thermal fluctuations results in Wiener stochastic process [47], [48] that is not differentiable with respect to time. Therefore, the Stieltjes integral is used instead of the Riemann integral to integrate the thermal term [47], [48]. The Stieltjes integral of the thermal term is defined in terms of the differential increments of Wiener process that has a variance proportional to the integration time step. Therefore, time-step dt appears in the denominator of the thermal field. The details of the integration of the LLG equation as a stochastic differential equation is explained in [45], [47], [49].

3.1.4 The spin transfer torque

The STT term is defined as $STT = \frac{\hbar}{2\mu_0 M_s a} m \times (m \times J^{spin})$ [50], where a is lattice constant, and J^{spin} is the spin current that is calculated from the quantum transport, as explained in 3.3.

3.2 The Ferroelectric Dynamics

The Landau-Devonshire (LD) expression of the free energy of FE material that describes the dependence of free energy of the FE material on the electric polarization and the electric field is defined as

$$F = \alpha_1 P^2 + \alpha_{11} P^4 + \alpha_{111} P^6 - \frac{V_a P}{t_{FE}}, \quad (3.3)$$

where α_1 , α_{11} , and α_{111} are the free-energy expansion coefficients for bulk material [51], [52]. The polarization of the material could be determined by minimizing the free energy (F) with respect to the electric polarization in (3.3). However, the LD expansion describes the static relation between electric field and polarization. The dynamic behavior of FE and its dependence on time is described by Landau-Khalatnikov (LK) equation:

$$\lambda \frac{\partial P}{\partial t} = -\frac{\partial F}{\partial P}, \quad (3.4)$$

where λ is the viscosity coefficient that represents the resistance of FE polarization motion toward the free energy minimum state.

3.3 Quantum Transport: Non-equilibrium Green's Function modeling of MFTJ

The NEGF models the magnetization dependent tunneling current by splitting the device into two independent channels for the spin-up and spin-down carriers. The schematic diagram in Fig. 3.1 shows the device meshing and the magnetization dependent DOS. The spin-based channel Hamiltonian H_{ch} and the left (right) contact Hamiltonian $H_{L(R)}$ [50], [53] of the MFTJ are defined as

$$H_{L(R)} = \begin{cases} \left(\alpha_{L(R)} \pm \frac{qV_a}{2} \right) I \pm \left(I - \sigma \cdot M_{L(R)}(\mathbf{i}) \right) \frac{\Delta_{L(R)}}{2}, & \mathbf{i} = \mathbf{j} \\ -t_{L(R)} I, & \mathbf{j} = \mathbf{i} \pm 1 \\ 0, & o.w. \end{cases} \quad (3.5)$$

$$H_{ch} = \begin{cases} (\alpha_{ch} + U_B) I + (qV_a + \phi_{BI} + \phi_1 - \phi_2) \left(\frac{N+1-2\mathbf{i}}{2N+2} \right) I, & \mathbf{i} = \mathbf{j} \\ -t_{ch} I, & \mathbf{j} = \mathbf{i} \pm 1 \\ 0, & o.w. \end{cases} \quad (3.6)$$

where a is the length of the mesh element, N is the number of the mesh elements, q is the electron charge, V_a is the applied voltage, ϕ_{BI} is the built-in potential, I is the identity matrix, i is the horizontal index of the Hamiltonian matrix, j is the vertical index of the Hamiltonian matrix, σ are the Pauli spin matrices, $\Delta_{L(R)}$ is the splitting energy of the left (right) contact as illustrated in Fig. 3.1, respectively, and $M_{L(R)}$ is the normalized magnetization of the left (right) contact. The Hamiltonian tight binding parameters are defined as $\alpha_{ch}(K_t) = 2t_{ch} + \frac{\hbar^2 K_t^2}{2m_{ch}^*}$, $\alpha_{L(R)}(K_t) = 2t_{L(R)} + \frac{\hbar^2 K_t^2}{2m_{L(R)}^*}$, $t_{ch} = \hbar/(2m_{ch}^*a^2)$, and $t_{L(R)} = \hbar/(2m_{L(R)}^*a^2)$, where K_t is the momentum vector in the transverse direction, $m_{L(R)}^*$ is the electron effective mass of left (right) electrodes, and m_{ch}^* is the electron effective mass of the channel.

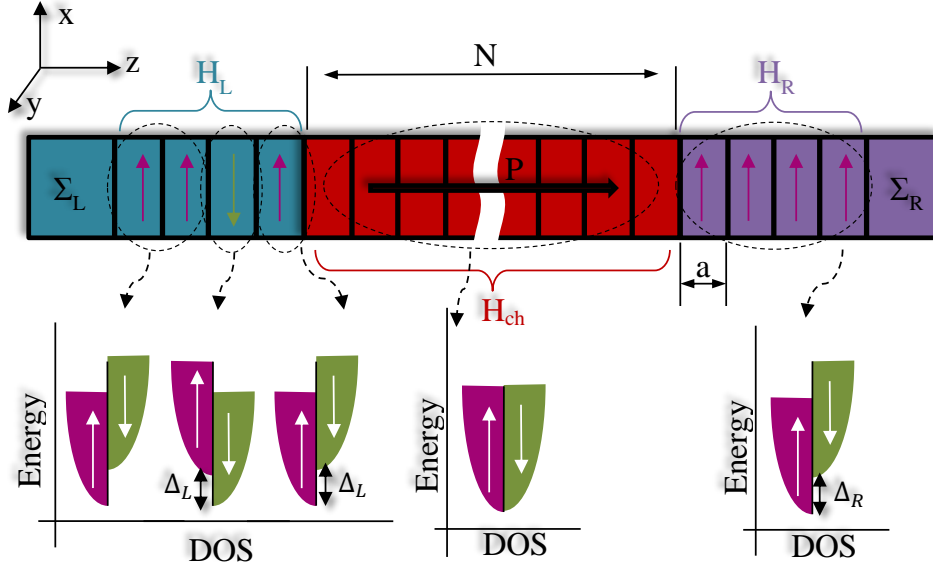


Figure 3.1. The MFTJ structure with the spin based NEGF meshing projected. The Hamiltonian definitions along with magnetization directions and DOS.

The Hamiltonian $H_{L(R)}$ dependence on the magnetization direction is modeled by the term $(I - \sigma \cdot M_{L(R)}(i)) \frac{\Delta_{L(R)}}{2}$. The term $(qV_a + \phi_{BI} + \phi_1 - \phi_2) \frac{(N+1-2i)}{2N+2} I$ in H_{ch} linearly interpolates the applied field and built-in potential $V_a + \phi_{BI} + \phi_1 - \phi_2$ over the channel. U_B is the barrier height relative to the conduction band. The term $\phi_1 - \phi_2$, that is estimated by (1.1-1.4), represents the dependence of the potential on the electric polarization of the FE

insulator. The screening lengths estimated by the DFT method and the electric polarization estimated by LK equation are plugged in Thomas-Fermi relation (1.1) to determine $|\phi_1 - \phi_2|$. The term $|\phi_1 - \phi_2|$ is necessary for evaluating the NEGF Hamiltonian (3.5).

The Green's function G is defined as

$$G = [EI - H - \Sigma_L - \Sigma_R]^{-1}, \quad (3.7)$$

where H is the full device Hamiltonian, $\Sigma_{L(R)}$ is the left (right) contact self-energy that is defined as

$$\Sigma_L = \begin{bmatrix} -t_L e^{iK_L^\uparrow a} & 0 & 0 & . & . & 0 \\ 0 & -t_L e^{iK_L^\downarrow a} & 0 & . & . & . \\ 0 & 0 & . & . & . & . \\ . & . & . & . & . & . \\ . & . & . & . & . & . \\ 0 & . & . & . & . & 0 \end{bmatrix}, \quad (3.8)$$

$$\Sigma_R = \begin{bmatrix} 0 & . & . & . & . & 0 \\ . & . & . & . & . & . \\ . & . & . & . & . & . \\ . & . & . & . & 0 & . \\ . & . & . & 0 & -t_R e^{iK_R^\uparrow a} & 0 \\ 0 & . & . & . & 0 & -t_R e^{iK_R^\downarrow a} \end{bmatrix}, \quad (3.9)$$

where $K_{L(R)}^\uparrow$ is the left (right) contact longitudinal wave vector of *spin-up* electron given by

$$K_{L(R)}^\uparrow = \cos^{-1} \left(1 - \frac{E \pm \frac{qV_a}{2} - \frac{\hbar^2 K_t^2}{2m_{L(R)}^*} + \frac{\Delta_{L(R)}}{2}}{2t_{L(R)}} \right), \quad (3.10)$$

and $K_{L(R)}^\downarrow$ is the left (right) contact longitudinal wave vector of *spin-down* electron given by

$$K_{L(R)}^\downarrow = \cos^{-1} \left(1 - \frac{E \pm \frac{qV_a}{2} - \left(\frac{\hbar^2 K_t^2}{2m_{L(R)}^*} \right) - \frac{\Delta_{L(R)}}{2}}{2t_{L(R)}} \right). \quad (3.11)$$

Finally, the Landau's current formula is defined as

$$J = \frac{-e}{2\pi^2\hbar} \int_{-\infty}^{\infty} \int_{-\infty}^{\infty} dk_x dk_y \int dEt (f_L - f_R), \quad (3.12)$$

where t is the transmission coefficient of the channel given by the expression

$$t = \text{Trace} \left(\Gamma_L G \Gamma_R G^\dagger \right), \quad (3.13)$$

and $\Gamma_{L(R)}$ is the left (right) broadening function defined by

$$\Gamma_{L(R)} = i \left(\Sigma_{L(R)} - \Sigma_{L(R)}^\dagger \right). \quad (3.14)$$

The Fermi-Dirac distribution $f_L(R)$ is defined as

$$f_{L(R)} = \frac{1}{e^{(E - \mu_{L(R)})/K_B T} + 1}. \quad (3.15)$$

The spin current is defined as [\[53\]](#)

$$J^{spin} = \frac{i}{2\pi^2\hbar} \int dk_x dk_y \int dE \text{Trace} [\sigma \cdot (H G^n - \dots G^n H)_{ij}] dE, \quad (3.16)$$

where G^n defined as

$$G^n = G(\Gamma_L f_L + \Gamma_R f_R) G^\dagger. \quad (3.17)$$

3.4 Time-dependent Formulation of Exchange interaction Coefficient based on Time-dependent Perturbation Theory

In the following discussion, we formulate a time-dependent formulation of the evolution from the FM to AFM phase induced by electric polarization. The sign of exchange interaction constant $J_{exch,i,j}$ is responsible for the magnetic order. The FM to AFM phase transition is controlled by the electrical polarization of the BTO. The change in the potential results from polarization switching can be considered as a small perturbation. Therefore we can use the time-dependent perturbation theory to model the time evolution of the exchange coefficient due to the perturbation potential [54]. The time-dependent perturbation potential can be formulated from the Thomas-Fermi relation as

$$V(z, t) = \frac{P(V_a, t)t_{FE}}{\frac{\delta_1}{\epsilon_{r1}} + \frac{\delta_2}{\epsilon_{r2}} + t_{FE}} \frac{\delta_1}{\epsilon_0 \epsilon_{r1}} e^{-\frac{|z|}{\delta_1}} - V_0, \quad (3.18)$$

$$V_0 = \frac{P(V_a, t=0)t_{FE}}{\frac{\delta_1}{\epsilon_{r1}} + \frac{\delta_2}{\epsilon_{r2}} + t_{FE}} \frac{\delta_1}{\epsilon_0 \epsilon_{r1}} e^{-\frac{|z|}{\delta_1}}, \quad (3.19)$$

where V_0 is the initial value of the potential. Assuming that the FM to AFM phase transition results from the transition from wave function ψ_b to ψ_a . The time dependent wave function can be written as $\Psi(z, t) = a(t)\psi_a(z)e^{-i\frac{E_a}{\hbar}t} + b(t)\psi_b(z)e^{-i\frac{E_b}{\hbar}t}$. The time evolution of $a(t)$ can be formulated as [54]

$$a(t) = -\frac{i}{\hbar} \frac{t_{FE}}{\frac{\delta_1}{\epsilon_{r1}} + \frac{\delta_2}{\epsilon_{r2}} + t_{FE}} \frac{\delta_1}{\epsilon_0 \epsilon_{r1}} \left\langle \psi_a | e^{-\frac{|z|}{\delta_1}} | \psi_b \right\rangle \int_0^t (P(t) - P(t=0)) e^{-i\omega t} dt, \quad (3.20)$$

where $\omega = \frac{E_b - E_a}{\hbar}$, E_a is the energy of ψ_a , and E_b is the energy of ψ_b . finally, the transition probability from state ψ_a to state ψ_b is $P_{b \rightarrow a} = |a(t)|^2$. The term $\left\langle \psi_a | e^{-\frac{|z|}{\delta_1}} | \psi_b \right\rangle$ can be determined from the normalization of the probability density. However, the polarization as function of time $P(t)$ is not known analytically. Therefore the integration (3.20) has to be

numerically evaluated. The time evolution of the exchange interaction coefficient can be formulated as

$$J'_{exch,i,j} = |J_{exch,i,j}| \left(1 - |a(t)|^2\right) - |J_{exch,i,j}| |a(t)|^2, \quad (3.21)$$

where $J_{exch,i,j}$ is the material-dependent magnetic exchange constant.

3.5 Simulation Procedure and Parameters selection

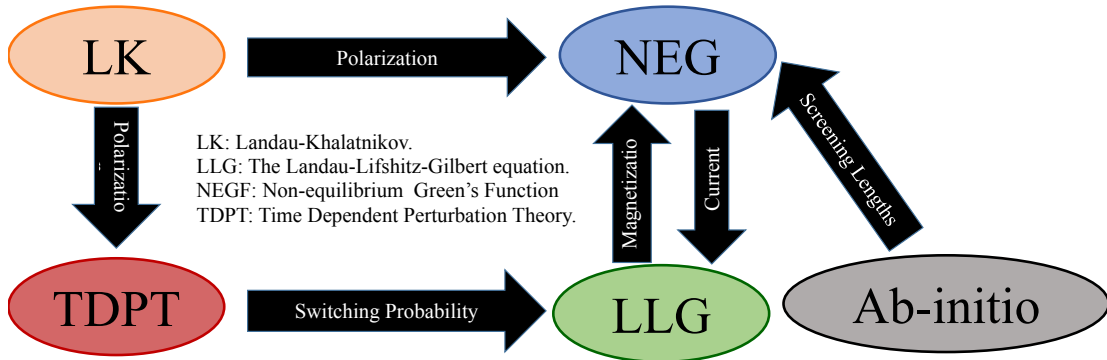


Figure 3.2. The self-consistent simulation procedure.

In the previous discussion, we explained the quantum transport model, the magnetization LLG equation, and the LK equation, separately. In the following discussion, we explain the methodology we used to solve these models together to get the MFTJ characteristics, as illustrated in Fig. 3.2. The steady-state characteristic of the MFTJ is calculated by the following procedure. Given the initial polarization P and the external applied voltage V_a , the term $\frac{dF}{dP}$ is calculated by differentiating the LD equation analytically. The $\frac{dF}{dP}$ obtained in the previous step is substituted in the LK equation to get $\frac{dP}{dt}$. Then the forward difference formula is used to update the polarization $P(t + dt) = P(t) + \frac{dP}{dt}dt$. The previous steps are repeated iteratively until the electric polarization reaches its steady-state value. After the steady-state electric polarization is obtained, the electrostatic potential is calculated from (1) and (4). Next the current is calculated from the quantum transport model. However, the solution of the transport model is dependent on the magnetization directions of the

electrodes which are calculated by the LLG equation. At the same time, the solution of the LLG equation depends on the current obtained from the NEGF equation. This raises the need for a self-consistent solution of the quantum transport and the LLG equation iteratively until the steady state current and magnetization are reached. The LLG equation is solved using Huen's method [45], [46]. The existence of the thermal fluctuation in the LLG equation makes it a stochastic differential equation (SDE). The integration of the SDE is explained in [45]–[47].

The time-dependent response of the MFTJ is calculated using the following procedure. **Step 1:** the term $\frac{dF}{dP}$ is calculated from the LD equation, given the initial polarization P and the external applied voltage V_a . The $\frac{dF}{dP}$ obtained in the previous step is substituted in the LK equation to get $\frac{dP}{dt}$. Then the forward difference formula is used to update the polarization as following $P(t + dt) = P(t) + \frac{dP}{dt}dt$. **Step 2:** the electrostatic potential is calculated from (1) and (4). **Step 3:** The spin current is calculated from the quantum transport model. The magnetization obtained from the solution of LLG and the electrostatic potential obtained in the previous step are used to solve the quantum transport. **Step 4:** the exchange coefficient $J'_{exch,i,j}$ is calculated from (3.20)–(3.21) using the electric polarization at time t obtained from the LK equation. **Step 5:** the LLG equation is solved to get $m(t + dt)$ using the spin current obtained from the quantum transport. Finally, the steps (Step 1) to (Step 5) are repeated at each time step.

The transport parameters are usually estimated by fitting the parameters on the experimental I-V characteristic [29], [50], [55]. However, the estimation process is not straight forward and more than one solution could produce the same transport properties. In this study, we try to go beyond that and predict some of the parameters from DFT calculations to reduce the complexity of the estimation process. On the other hand, some transport processes cannot be included in the DFT calculation. Note, the DFT by definition describes the system at the ground minimum energy state. In contrast, the quantum transport model exhibits nonequilibrium conditions by definition. Therefore, it is better to estimate certain parameters from experimental data to account for these limitations of DFT. Because of the aforementioned discussion, we adopted a combination of estimating the parameters directly

from experimental data and estimating the parameters from DFT to improve the quality of parameter estimation.

The simulation parameters used in this study are selected according to the following criterion. The saturation magnetization, magnetic exchange constant are estimated from DFT calculations. The magnetic anisotropy is selected from the experimental study [11]. The magnetic damping factor is set within the acceptable range of similar structure. The screening lengths and the splitting energy are estimated by the DFT calculation. The effective mass are tuned within the acceptable range in literature to produce the experimental results. This is a very common procedure for selecting effective mass [29], [50], [53], [55].

The Landau-Devonshire equation parameters α_1 , α_{11} , and α_{111} are calculated from the critical voltage at which the electric polarization is switched and the values of the polarization at zero voltage. The values of the critical voltage and polarization at zero voltage are known from the experimental results in [11]. The two values of the polarization at zero voltage are local minimum points of the free energy. The free energy has a maximum point at zero polarization. The maximum and minimum points are located at the zeros of the first derivative of the free energy and impose constraints on the sign of the second derivative of the free energy. In addition, the coefficient of the highest order term in the free energy has to be positive because the free energy has to reach positive infinity as the polarization reaches $\pm\infty$. We used a numerical grid search to solve for α_1 , α_{11} , and α_{111} that considers the aforementioned constraints. The viscosity coefficient is estimated by a grid search to get 5ns switching time. Finally, the energy E_a and E_b in (3.20) are estimated from DFT calculations.

4. SIMULATION RESULTS AND ANALYSIS

4.1 Comparison with Experimental MFTJ Characteristics

The main advantage of spin-based NEGF is the ability to model the four resistance states of the MFTJ. The LSMO-LCMO-BTO-LSMO MFTJ in [11] is the most appropriate device to demonstrate these physical characteristics. The simulation results of LSMO-LCMO-BTO-LSMO are illustrated in Fig. 4.1. The proposed framework can capture the majority of the MFTJ I-V characteristic for positive (low resistance) and negative (high resistance) polarization states, as illustrated in Fig. 4.1. The simulation results for LSMO-BTO-Co FTJ are in agreement with the experimental results [5], as illustrated in Fig. 4.2. The simulation parameters of the LK and the LLG equations are $\alpha_1 = -1.0654 \times 10^9 \text{ m/F}$, $\alpha_{11} = -6.0878 \times 10^9 \text{ m}^5/(C^2.F)$, $\alpha_{111} = 5.0499 \times 10^{10} \text{ m}^9/(C^4.F)$, $dt = 1 \times 10^{-14} \text{ s}$, $K_U = 7.8 \times 10^4 \text{ erg/cm}^3$, $\alpha = 0.05$, $\lambda = 1.8 \text{ s/F}$, $j_{exch,i,j} = 4.5 \times 10^5 \text{ erg/cm}^3$, $|E_a - E_b| = 0.029 \text{ eV}$ and $M_s = 414.15 \text{ emu/cm}^3$.

As explained in section 2, the LCMO layer goes through a phase transition from the FM to the AFM alignment by the influence of the electric polarization switching. The phase transition is confirmed by the following experimental procedure [11]. Starting by applying an external magnetic field to the MFTJ, the change in the resistance of the MFTJ due to the increase of the external magnetic field is measured. In the case of positive polarization, the device resistance diminishes due to the increase of the external magnetic field. In contrast, the negative polarization state exhibits a constant resistance independent of the magnetic field. This behavior of the MFTJ resistance is explained by the influence of the external magnetic field on the AFM aligned Mn site and the ability of the external magnetic field to switch the AFM aligned Mn site back to FM alignment [11]. Fig. 4.3 illustrates the effect of the external magnetic field on the MFTJ resistance that is produced by the quantum transport and magnetization dynamics. The simulation mimics the same physical device behavior because the FM electrode Hamiltonian has a magnetization dependent term (3.6).

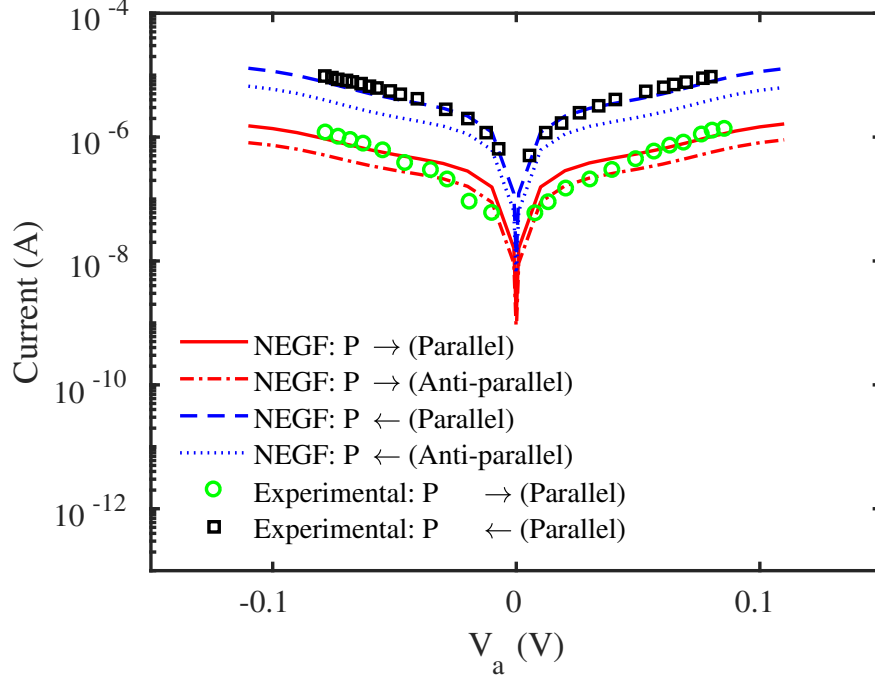


Figure 4.1. The current of LSMO-LCMO-BTO-LSMO MFTJ is illustrated at different applied bias voltages V_a for the four MFTJ states. The experimental data for the same device is demonstrated in [11]. The simulation parameters are $m_{ch}^* = 0.8m_0$, $m_L^* = 0.9m_0$, $m_R^* = 0.9m_0$, m_0 is the free electron mass, $\mu_L = 3$ eV, $\mu_R = 3$ eV, $\Delta_L = 2.4$, $\Delta_R = 2.4$ eV, $U_B = 3.1$ eV, $\phi_{BI} = 1$ eV, $t_{FE} = 2$ nm, $T = 80$ K [11], and the MFTJ radius is $8.5 \mu m$. The screening lengths of the electrodes used in NEGF simulation are estimated by DFT, as illustrated in section 2.

4.2 Analysis of Various MFTJ Parameters

The TER is estimated at different values of the splitting energy, as illustrated in Fig. 4.4. The TER dependence on splitting energy originates from the ME effect that happens in the LCMO/BTO interface. Moreover, the TMR_{\rightarrow} is consistently lower than TMR_{\leftarrow} as illustrated in Fig. 4.1. This asymmetric behavior is due to the antiferromagnetic alignment of the Mn sites of the LCMO electrode in the case of P_{\rightarrow} state that reduces the TMR effect at that state. In contrast, the LCMO exhibits FM alignment in the case of P_{\leftarrow} state, and hence the TMR_{\leftarrow} is higher compared to TMR_{\rightarrow} .

The asymmetry in the electrodes screening lengths is necessary for an FTJ to exhibit a TER effect, as explained in section 1.1. However, the NEGF transport simulations show

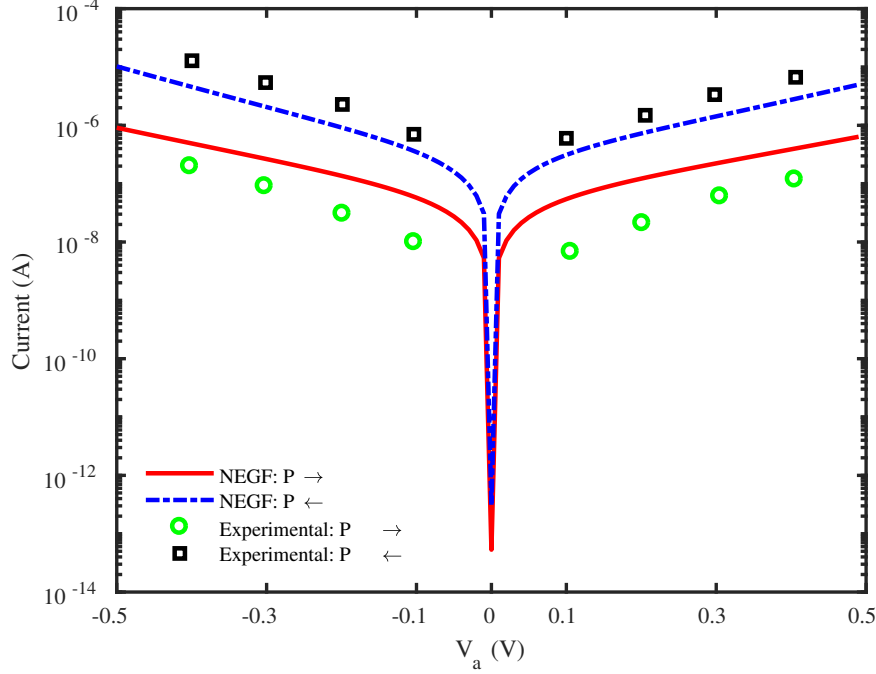


Figure 4.2. The current of LSMO/BTO/Co FTJ is illustrated at different applied bias voltages V_a . The experimental data for the same device is demonstrated in [5]. The simulation parameters are $m_{ch}^* = 0.8m_0$, $m_L^* = 0.9m_0$, $m_R^* = 2m_0$, $\mu_L = 3$ eV, $\mu_R = 2.9$ eV, $\Delta_L = 2.4$, $\Delta_R = 1.8$ eV, $U_B = 3.16$ eV, $\phi_{BI} = 1.2$ eV, $t_{FE} = 3$ nm, m_0 is the free electron mass, $T = 300K$ [23], and the FTJ radius is 350 nm. The screening lengths of the electrodes used in NEGF simulation are estimated by DFT, as illustrated in section 2.

a significant TER ratio for a hypothetical device that has electrodes of identical screening lengths. Fig. 4.5 shows the TER ratio as a function of the built-in potential ϕ_{BI} along with the electrostatic potential of the positive and negative polarization states at different values of ϕ_{BI} . Although the electrodes screening lengths are identical, the TER ratio increases significantly due to the increase of the built-in potential. The origin of the TER effect in the case of symmetric electrodes screening lengths could be explained by observing the potential profile of the positive and negative polarization states. In the case of $\phi_{BI} = 0$, the potential profiles of P_{\rightarrow} and P_{\leftarrow} are symmetric, and hence the TER ratio is zero as expected. However, as the built-in potential ϕ_{BI} increases, the potential profile of P_{\rightarrow} and P_{\leftarrow} start to deviate from the symmetric shapes to asymmetric potential profiles that have different average barrier height, as illustrated in the inset of Fig. 4.5. In other words, the built-in

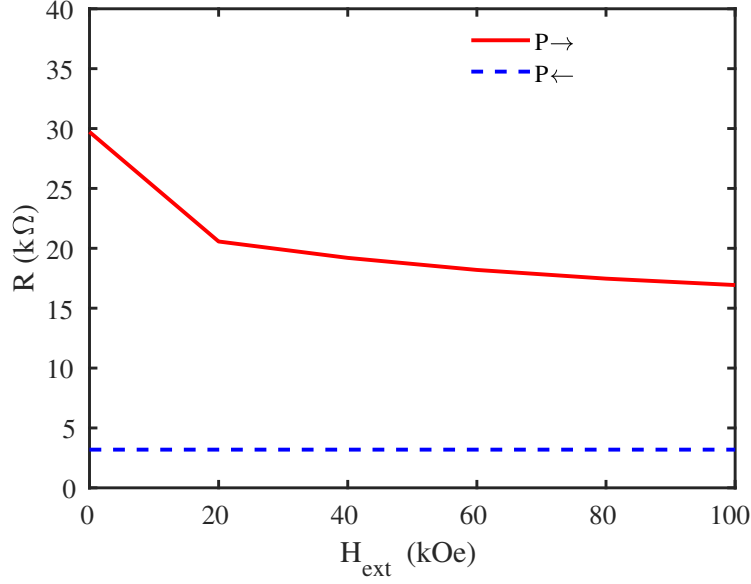


Figure 4.3. The resistance of LSMO/LCMO/BTO/LSMO MFTJ is illustrated under the effect of external magnetic field.

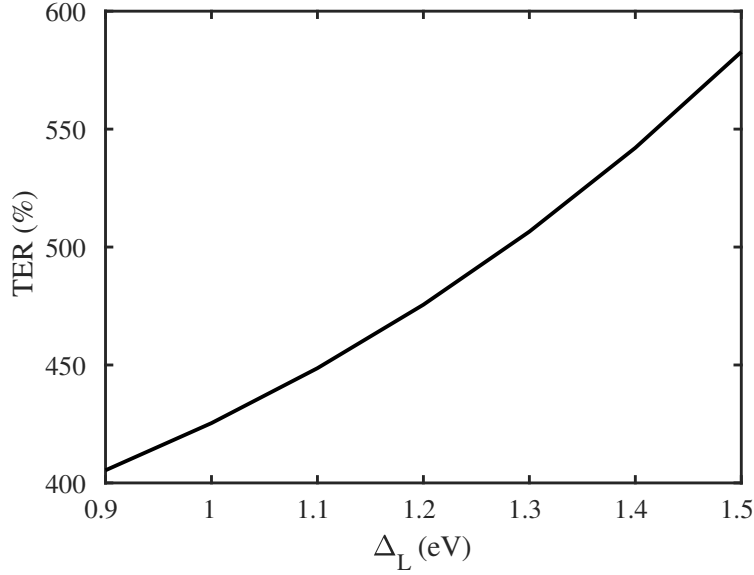


Figure 4.4. The TER of the MFTJ as a function of splitting energy Δ_L .

potential introduces another source of asymmetry that allows the modulation of the barrier average height by the electric polarization.

The exponential dependence of the TER on the left and right electrode screening lengths ratio is demonstrated in Fig. 4.6. In order to understand the TER behavior as a function of $\frac{\delta_1}{\delta_2}$, we have reordered the TER definition as $TER = \frac{j_{\leftarrow}}{j_{\rightarrow}} - 1$, where j_{\rightarrow} and j_{\leftarrow} are the current

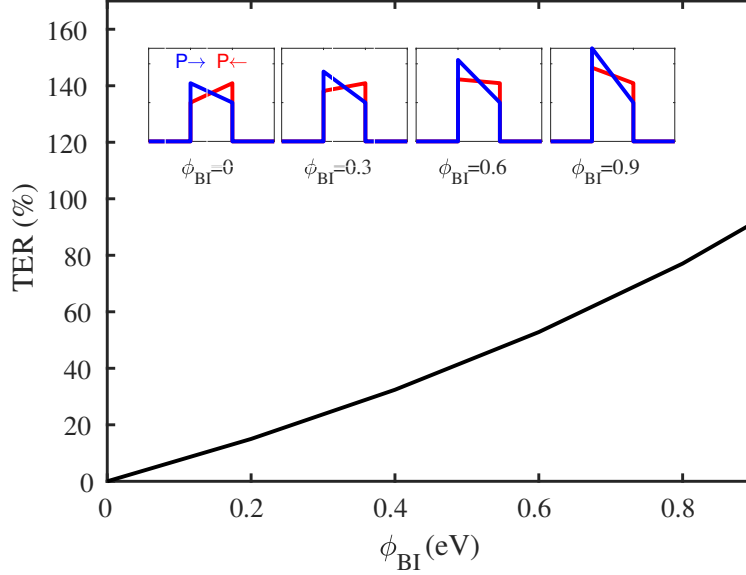


Figure 4.5. The TER as a function of the built-in potential ϕ_{BI}

at positive (*high resistance*) and negative (*low resistance*) polarization states, respectively. The strength of the barrier height modulation, induced by polarization switching, is enhanced by increasing the difference between the screening lengths of the electrodes. Therefore, the current j_{\rightarrow} increases and the current j_{\leftarrow} decreases, as illustrated in Fig. 4.6. Consequently, the TER improves exponentially as the ratio $\frac{\delta_1}{\delta_2}$ reaches zero. The same conclusion can be quantitatively derived from the Thomas-Fermi relation (1.1) that formulates the potential at the interface as $\phi_1 = \frac{\sigma_s \delta_1}{\epsilon_0 \epsilon_r}$. Therefore, the potential ϕ_1 decreases as δ_1 shrinks, and hence the potential difference $||\phi_1| - |\phi_2||$ rises along with the ratio $\frac{j_{\leftarrow}}{j_{\rightarrow}}$. As a result of $\frac{j_{\leftarrow}}{j_{\rightarrow}}$ exponential increase, the TER exponentially improves.

Interestingly, the TER shows exponential dependence on the ratio $\frac{\delta_1}{\delta_2}$, but weaker dependence on the barrier height U_B . The rationale behind the difference in the dependence of TER on $\frac{\delta_1}{\delta_2}$ and U_B is explained in the following comparative analysis. The decay of the ratio δ_1/δ_2 results in increasing j_{\rightarrow} and decreasing j_{\leftarrow} that exponentially enhance the TER. In contrast, the increase in the barrier height U_B reduces both j_{\rightarrow} and j_{\leftarrow} but with different rates. Therefore, the TER changes with a weak rate because it is proportional to $\frac{j_{\leftarrow}}{j_{\rightarrow}}$, as illustrated in Fig. 4.7. However, the TER curve looks approximately linear because of the narrow range of U_B along with the weak exponential dependence of the TER on U_B . The MFTJ high and

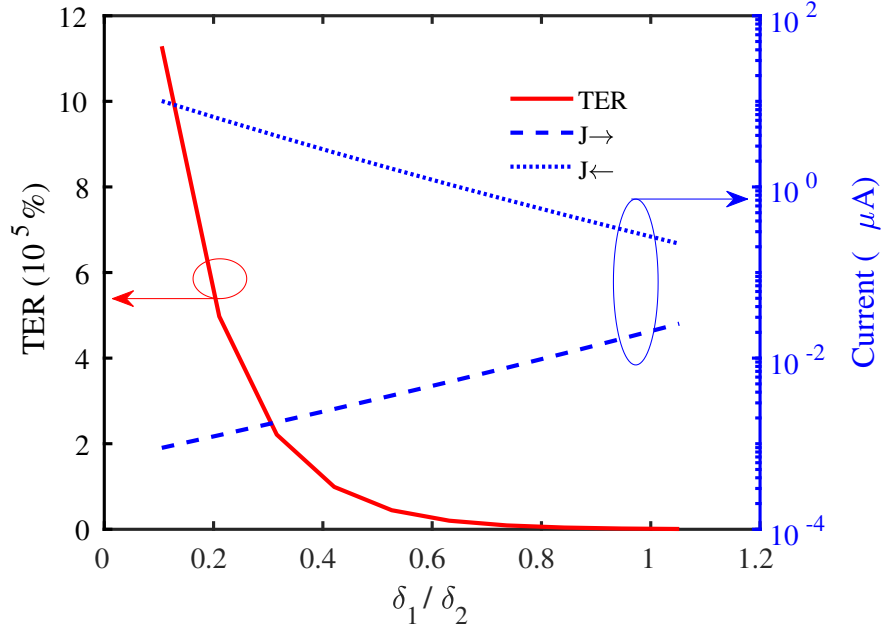


Figure 4.6. The TER of the MFTJ as a function of the screening lengths ratio δ_1/δ_2 .

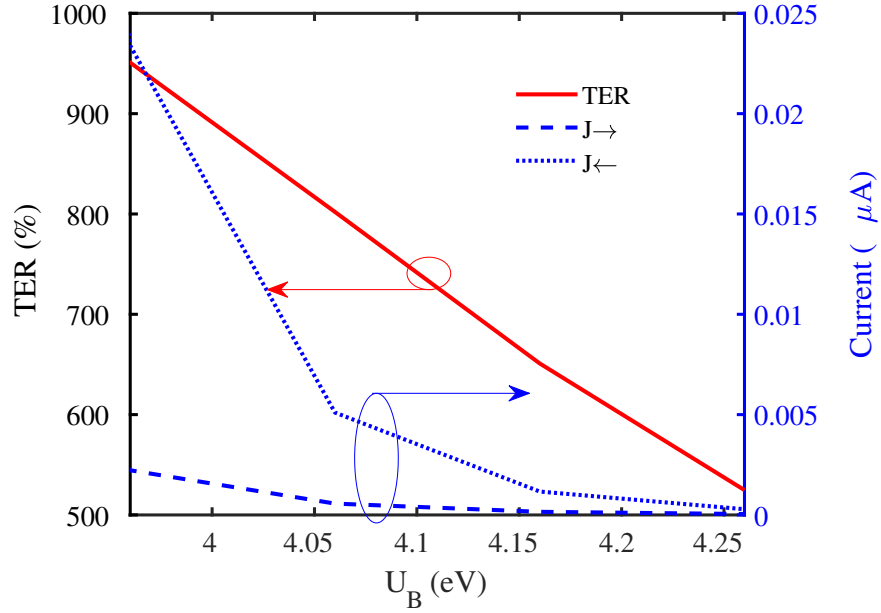


Figure 4.7. The current and TER of the MFTJ as a function of barrier height U_B .

low resistances is exponentially augmented as U_B elevates, as observed from the currents j_{\rightarrow} and j_{\leftarrow} in Fig. 4.7. The barrier height is dependent on the insulator and electrodes work

functions. Therefore, the electrodes work functions together with the screening lengths have a strong influence on the resistance and the TER of MFTJ, respectively.

4.3 MFTJ Dynamic Characteristics

The time-dependent response of the MFTJ switching is illustrated in Fig. 4.8. The MFTJ dynamic response is calculated according to the procedure explained in section 3.5. The electric polarization takes around $5ns$ to switch from negative to positive value and saturate. The transition probability elevates from zero to one and saturates following the electric polarization, as illustrated in Fig. 4.8. The transition probability of the FM phase to the AFM phase is calculated from (3.20) that is based on the time-dependent perturbation theory. The exchange coupling coefficient follows the transition probability according to (3.21). Therefore, the exchange coefficient change from a positive value (FM alignment) to a negative value (AFM alignment). The magnetization of the second Mn atom switches from positive to negative magnetization following a magnetic precession motion because of the change in the exchange coupling. The precession motion of the magnetization causes the oscillation of the MFTJ current, as illustrated in Fig. 4.9.

Interestingly, the electric current decreases significantly after $4ns$ from the start of the switching process. The large variations of the current are due to the electric polarization switching. In contrast, the change in magnetic configuration lags the electric polarization switching, as illustrated in Fig. 4.8 and Fig. 4.9. During the switching process, the electric polarization changes from negative to positive direction passing by $P = 0$. The electrostatic potential is modulated by the electric polarization as described by Thomas-fermi relation. The current reaches its minimum value because the tunneling current changes from Nordheim tunneling to direct tunneling at that point. The current changes back to Nordheim tunneling after the minimum point. Therefore, the current starts to increase after the minimum current point. Note, non-ideal contacts are assumed at high switching voltage to allow a constant voltage drop at each contact of $0.2V$ during quantum transport.

In contrast, the oscillations that start after the current minimum point are due to the precession motion of the Mn atoms. The precession motion of the Mn atoms is derived by the magnetic exchange torque of neighbor atoms. Due to the time-dependent perturbation

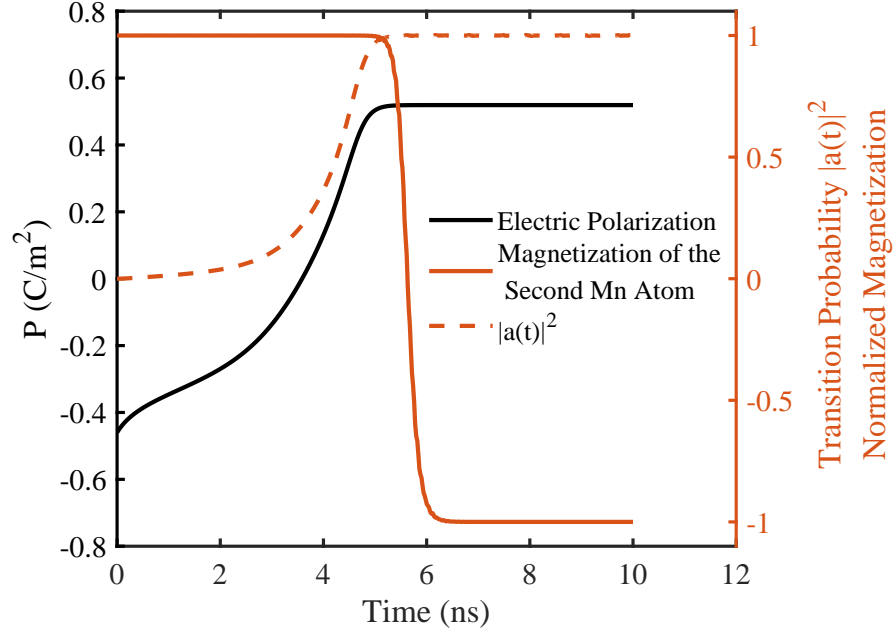


Figure 4.8. The electric polarization, the transition probability $|a(t)|^2$ and the z component of the magnetization of the second Mn atom away from the LAMO/BTO interface.

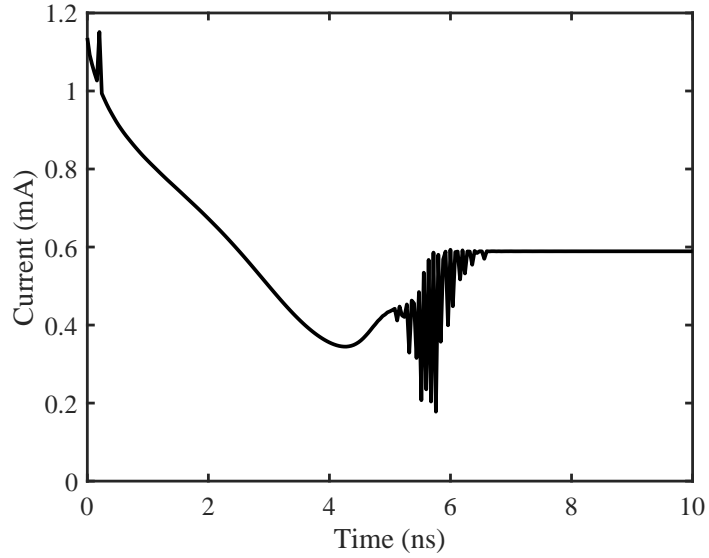


Figure 4.9. The current of the MFTJ as a function of time.

potential caused by electric polarization switching, the probability of magnetization switching to AFM alignment increases from zero to one. The magnetization switching lags the

switching probability by hundreds of picoseconds. The reason behind the delay in the magnetization switching is that the magnetization and the effective exchange field have almost an angle of π at the initial position. Therefore, the magnetization motion under the effect of magnetic torque is slow at the beginning. The thermal fluctuations could assist the switching process at the slow-starting part of the switching process. However, the thermal fluctuations are small compared to the magnetic anisotropy due to the large area of the MFTJ.

5. ANTIFERROELECTRIC TUNNEL JUNCTIONS AS ENERGY-EFFICIENT COUPLED OSCILLATORS: MODELING, ANALYSIS, AND APPLICATION TO SOLVING COMBINATORIAL OPTIMIZATION PROBLEMS

The majority of the combinatorial optimization problems are solved by searching a solution space that grows as an exponential function of the problem size. Such class of problems scales inefficiently on the Boolean von Neumann architecture. On the other hand, some alternative computing techniques like coupled-oscillator networks are efficient in solving combinatorial optimization problems. In this study, we demonstrate the effectiveness of antiferroelectric tunnel junctions (AFTJs) in coupled-oscillator networks for solving combinatorial optimization problems such as graph coloring. AFTJs are tunnel junctions that show a high on/off current ratio. The high on/off current ratio of AFTJs allows a higher sense margin at low bias current. Consequently, AFTJs oscillators are more energy-efficient compared to VO_2 , $HfTaOx$, and $TaOx$ based oscillators. This study explains the origin of the large on/off current ratio of AFTJs [56]. A physics-based model is proposed to determine AFTJ current. The proposed AFTJ model is compared to experimental results to show the ability of the model to predict AFTJs behavior. The proposed AFTJ model is implemented in Verilog-A to be used in circuit simulations of the AFTJ based coupled-oscillator network. The AFTJ based coupled-oscillator network could approximate the solution of graph coloring efficiently.

A large set of combinatorial optimization problems have a non-deterministic polynomial (NP) time complexity [57]. The class of NP problems scales inefficiently on the conventional Boolean based von Neumann architecture which is the main computational approach for modern computers [58]. Many alternative computational models have gained a growing interest in the literature. One of the interesting alternative computing technique is the synchronized network of a large number of coupled oscillators [59]. The synchronized network of coupled oscillators has been used to solve combinatorial optimization problems like graph coloring [60]. The coupling of such a large number of oscillators inspired the exploration of new energy-efficient circuit primitives that can pave the path for efficient realization of such networks. However, to make such coupled oscillatory networks, there is a need to explore

proper device characteristics with high on-off ratio, simple coupling mechanisms to a couple (frequency or phase) large number of oscillators, and to have a high frequency of oscillation for faster operation.

Recently, an antiferroelectric tunnel junction (AFTJ) [61] that has a large on/off current ratio has been reported in the literature. Such a large on/off ratio provides a large sense margin. The large sense margin reduces the power needed to amplify/read the device status. The utilization of the AFTJ as an oscillator can provide an efficient building block for the network of coupled oscillators compared to other emerging devices e.g., VO_2 [62], $HfTaOx$ [63], and $TaOx$ [64].

As an application of the proposed AFTJ based coupled oscillator to solve a combinatorial optimization problem, we will consider the graph coloring problem. [Note, the graph coloring problem is also an abstract description of many real-world problems e.g., frequency allocation in communication networks, resource allocation, and scheduling problems.] The problem can be stated as finding the minimum number of colors to color graph with the constraint that every two connected nodes on the graph have different colors. The graph chromatic number is defined as the minimum number of colors required to color a graph. To solve the graph coloring problem using the coupled-oscillator network, the solution space has to be mapped to the energy landscape of the coupled-oscillator network. The mapping is achieved by shaping the coupling between the oscillators according to the adjacency matrix of the graph. The minimum energy of the coupled oscillator network overlaps with the optimal coloring of the graph (chromatic number)[60], as we will explain in section 5.2.

In this study, we first consider circuit techniques using AFTJs to efficiently solve the graph coloring problem. We propose a physics-based model that explains the AFTJ I-V characteristics. The results of the proposed model are compared to experimental data. We explain the difference between ferroelectric tunnel junctions (FTJs) and AFTJs current characteristics and the criterion by which these differences are reflected in the model. We demonstrate the difference between the proposed model with the state of the art in the literature of AFTJs [61]. We demonstrate the use of an AFTJ as an oscillator in the coupled oscillator network. The energy and performance of the AFTJ are compared to other devices

e.g., VO_2 [62], $HfTaOx$ [63], and $TaOx$ [64] showing the energy efficiency of AFTJ oscillators. Finally, we use the coupled oscillator networks to solve the graph coloring problem.

5.1 AFTJ physics

Recently, AFTJ with high tunneling electro-resistance (TER) of 10^5 has been reported in literature [61]. The AFTJ consists of antiferroelectric insulating layer and two ferromagnetic electrodes $La_{0.7}Sr_{0.3}MnO_3(LSMO)/PbZrO_3(PZO)/Co$. The epitaxial PZO film is deposited by pulsed laser deposition. The AFTJ exhibits two different resistance states. The **high resistance state** is the ground state at low applied external voltage. The **low resistance state** is the state at the high positive/negative applied voltage and hence, the positive/negative nonzero electric polarization of PZO. The origin of the high TER ratio is due to the modulation of the barrier height by the electric polarization of the antiferroelectric insulator. To explain the physical origin of the AFTJ characteristics, we start by explaining the antiferroelectric material dynamics. Next, we formulate the electrostatic potential of AFTJ as a function of the applied voltage and the electric polarization of the PZO insulator. Finally, we use the formulated electrostatic potential of an AFTJ along with Wenzel-Kramer-Brillouin (WKB) approximation to model the tunneling current through the trapezoidal barrier of the AFTJ.

5.1.1 The antiferroelectric dynamics

The antiferroelectric material is defined as a material with two sublattices that are spontaneously polarized but in antiparallel direction. Therefore, Kittel [65] formulated the free energy of antiferroelectric material based on two variables P_a and P_b that are the electric polarization of the sublattices a and b , respectively. The free energy of antiferroelectric material is defined by Kittel's model [65] as

$$F = f_a P_a^2 + f_b P_b^2 + g P_a P_b + h_a P_a^4 + h_b P_b^4 - E(P_a + P_b), \quad (5.1)$$

where E is the external applied electric field, f_a , f_b , g , and h are temperature dependent coefficients. The evolution of the polarization with respect to time is described by the following relation

$$\gamma \frac{\partial P_a}{\partial t} = -\frac{\partial F}{\partial P_a}, \quad (5.2)$$

$$\gamma \frac{\partial P_b}{\partial t} = -\frac{\partial F}{\partial P_b}, \quad (5.3)$$

where γ is the viscosity coefficient that models the resistance of P_a and P_b polarization motion toward the free energy minimum state. The antiferroelectric material has zero polarization at zero applied voltage and nonzero electric polarization at bias voltage that is higher than the threshold voltage, as illustrated in Fig. 5.1. The antiferroelectric behavior could be understood as a superposition of the polarization of the two ferroelectric sublattices aligned in antiparallel directions. The relations (5.2) and (5.3) describe the motion of the electric polarization toward the minimum of the free energy of the antiferroelectric material.

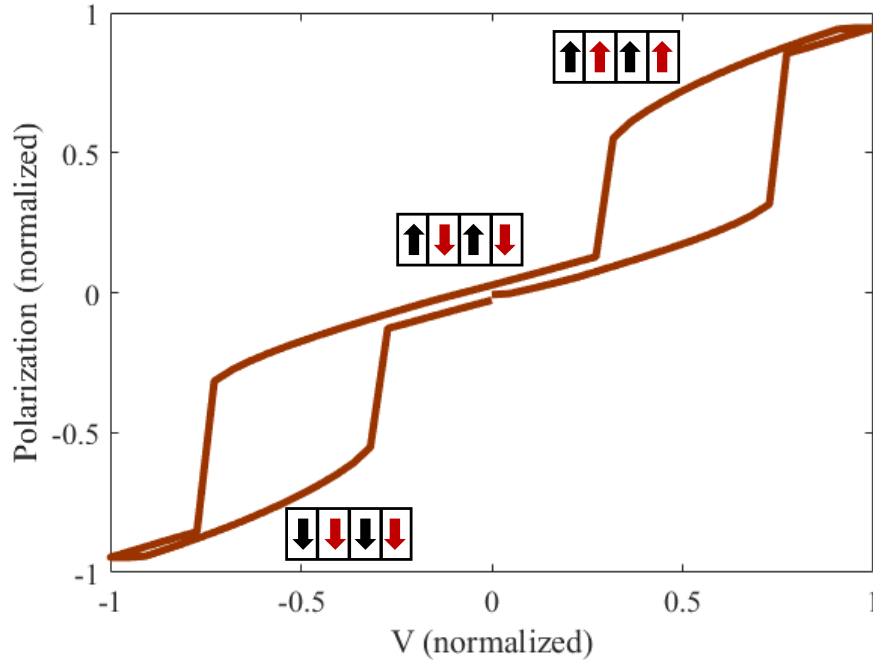


Figure 5.1. The electric polarization of antiferroelectric material.

5.1.2 The electrostatic potential

At *high resistance state* (low external voltage), PZO layer has almost zero electric polarization. The applied external voltage at the metal electrodes generates an electric field inside the insulator. The insulator does not have any free charge or bound charges at low external voltage. Therefore, the electric field is constant inside the insulator and the electrostatic potential is linear. The electrostatic barrier has a trapezoidal shape, as illustrated in Fig. 5.2. The trapezoidal-shaped barrier is a sign of Fowler-Nordheim tunneling current [66].

At *low resistance state* (high external voltage), the electric polarization of PZO switch to ferroelectric state. The PZO insulator layer does not have free charges. However, dielectric dipoles of PZO are not compensated at the interface and hence a non-zero layer of bound charges is formed. The free electron gas in the metal electrodes accumulates near the interface by the influence of the bound charges at the interface. However, the electric field of bound charges is partially screened by the free electron gas. The uncompensated charges result in a nonzero electric field inside the insulator that opposes the externally applied voltage. Therefore, the electrostatic barrier is reduced due to the opposing electric field induced by the electric polarization of the insulator layer. Consequently, the current increases as the barrier height decreases. Therefore, the AFTJ resistance reaches its low resistance state. Now, let us formulate the previous qualitative discussion of the AFTJ operations in formal mathematical representation. The formulation has been first introduced for FTJ [15], [20]. We start from the Thomas-Fermi [67] and Gauss's law to formulate the electric potential profile of the AFTJ. Next, we use the WKB approximation to model the tunneling current through the trapezoidal barrier [68]–[70].

The Thomas-Fermi screening relation [67] (5.4) is a theoretical approximation of the fast decay of the electric field of positive charges due to the screening by the free electron gas. The Thomas-Fermi relation is defined as

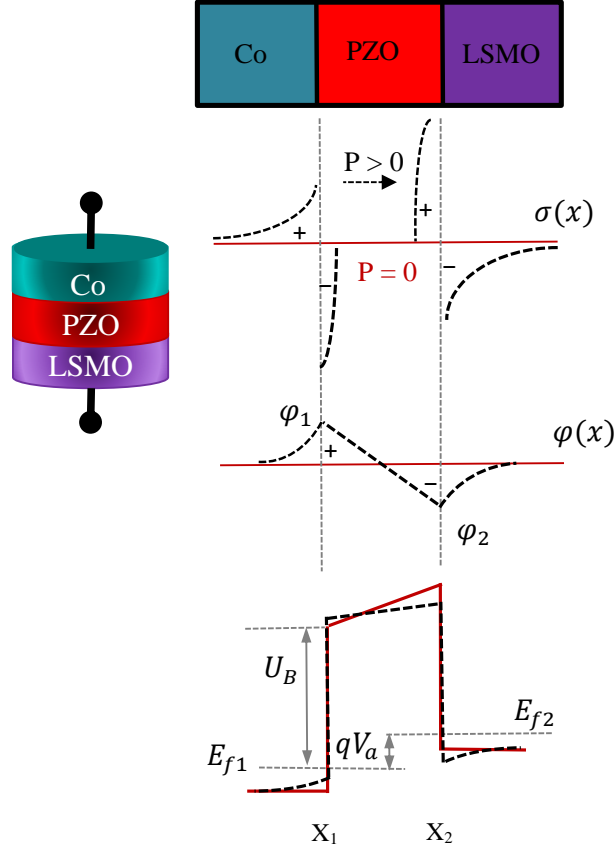


Figure 5.2. The layered structure of AFTJ and the electrostatic potential at different states of electric polarization.

$$\varphi(x) = \begin{cases} \frac{\sigma_s \delta_1}{\epsilon_0 \epsilon_{r1}} e^{-\frac{|x-x_1|}{\delta_1}} & x < x_1 \\ -\frac{\sigma_s \delta_2}{\epsilon_0 \epsilon_{r2}} e^{-\frac{|x-x_2|}{\delta_2}} & x > x_2 \end{cases} \quad (5.4)$$

where φ is the electrostatic potential, σ_s is the surface charge density of free charges, ϵ_0 is permittivity of free space, ϵ_{r1} (ϵ_{r2}) is the permittivity of the left (right) electrode, and δ_1 (δ_2) is the screening length of the left (right) electrode. The electrostatic potential at the left and right interface are defined by Thomas-Fermi relation as $\varphi_1 = \frac{\sigma_s \delta_1}{\epsilon_0 \epsilon_{r1}}$ and $\varphi_2 = \frac{-\sigma_s \delta_2}{\epsilon_0 \epsilon_{r2}}$, respectively. The potential difference between the electrodes is $\varphi_1 - \varphi_2 = \frac{\sigma_s \delta_1}{\epsilon_0 \epsilon_{r1}} + \frac{\sigma_s \delta_2}{\epsilon_0 \epsilon_{r2}}$. The

potential difference $\varphi_1 - \varphi_2$ is proportional to the electric field inside the insulator E_{AF} according to the relation

$$\frac{\sigma_s \delta_1}{\epsilon_0 \epsilon_{r1}} + \frac{\sigma_s \delta_1}{\epsilon_0 \epsilon_{r2}} + E_{AF} t_d = 0, \quad (5.5)$$

where t_d is the thickness of the insulator layer. The electric field inside the insulator is proportional to the charge density at the interface. By applying Gauss' law at the interface, we get

$$E_{AF} = \frac{(\sigma_s - P)}{\epsilon_0}, \quad (5.6)$$

where P is the electric polarization of antiferroelectric insulator. We rearrange (5.5) and substitute by the definition of the electric field (5.6) to formulate σ_s as

$$\sigma_s = \frac{Pt_d}{\frac{\delta_1}{\epsilon_1} + \frac{\delta_2}{\epsilon_2} + t_d}. \quad (5.7)$$

Finally, the electric potential of the junction is a superposition of the externally applied field and the potential induced by the electric polarization of the PZO insulator. The PZO insulator has zero charge density except for the bound charges at the interface. Therefore, the electric field has to be constant in the insulator layer and the potential is linear. Based on the previous discussion the electrostatic potential could be formulated as

$$\varphi(x) = \begin{cases} \frac{\sigma_s \delta_L}{\epsilon_0 \epsilon_L} e^{-\frac{|x-x_1|}{\delta_L}} & x < x_1, \\ \left(\frac{\sigma_s \delta_L}{\epsilon_0 \epsilon_L} + \frac{\sigma_s \delta_R}{\epsilon_0 \epsilon_R} + qV_a \right) \times \dots \\ \frac{(x-x_1)}{t_{FE}} + U_B & x_2 < x < x_1, \\ \frac{\sigma_s \delta_R}{\epsilon_0 \epsilon_R} e^{-\frac{|x-x_2|}{\delta_R}} & x_2 < x, \end{cases} \quad (5.8)$$

where q is the electron charge, and V_a is the applied voltage.

5.1.3 Tunneling current

In the previous discussion, we could formulate the relation between the electric polarization of PZO and the potential barrier profile. In this section, we apply the WKB approximation together with the barrier profile in (5.8) to model the tunneling current in AFTJs. The WKB approximation of the transmission through trapezoidal barrier [68]–[70] is defined as

$$T(E_x) = e^{-\frac{\sqrt{8m\beta}}{\hbar} \int_{x_1}^{x_2} \sqrt{(\varphi(x) - E_x)} dx}, \quad (5.9)$$

where E_x is the energy in the transport direction, β is fitting parameter and m is the electron effective mass. Substituting the potential (5.8) in (5.9) and integrating with respect to x direction we get

$$T(E_x) = e^{-\frac{\sqrt{32m\beta}}{3\hbar A} \left[(\varphi(x_2) - E_x)^{\frac{3}{2}} - (\varphi(x_1) - E_x)^{\frac{3}{2}} \right]}, \quad (5.10)$$

where A is defined as $A = \frac{1}{t_{FE}} \left(\frac{\sigma_s \delta_1}{\epsilon_0 \epsilon_{r1}} + \frac{\sigma_s \delta_2}{\epsilon_0 \epsilon_{r2}} + qV_a \right)$. In contrast, the low resistance state barrier is not trapezoidal at certain applied voltages. Therefore, the integration in (5.9) is evaluated as

$$T(E_x) = e^{-\frac{\sqrt{8m\beta}}{\hbar} \sqrt{(\bar{\varphi} - E_x)} t_d}, \quad (5.11)$$

where $\bar{\varphi}$ is the average potential height. The electric current density is defined as [70]

$$j = \frac{4\pi q}{\hbar} \sum_{\vec{k}_t} \int_{-\infty}^{\infty} T(E_x) [f_1(E_x) - f_2(E_x)] dE_x, \quad (5.12)$$

where \hbar is reduced Planck's constant, K_t is the transverse momentum, $f_{1(2)}$ is the Fermi-Dirac distribution. The Fermi-Dirac distribution is defined as

$$f_{1(2)} = \frac{1}{1 + e^{(E_x - \mu_{1(2)})/KT}}, \quad (5.13)$$

where $\mu_1(\mu_2)$ is the chemical potential of the left (right) contact, K is the Boltzmann constant, and T is the temperature. By replacing the summation in (5.12) to integration over the transverse momentum K_t and evaluating the integration analytically, we get

$$j = \frac{2m\beta q}{\hbar^3} \int_{-\infty}^{\infty} T(E_x) [F_1(E_x) - F_2(E_x)] dE_x, \quad (5.14)$$

where $F_{1(2)}$ is defined as $F_{1(2)} = KT \ln \left(1 + e^{\frac{E_x - \mu_{1(2)}}{KT}} \right)$.

5.1.4 Simulation results and discussion

In the previous section, we explained the relation between the polarization and the electrostatic potential. The formulation in (5.8) is similar to the formulation introduced for FTJ [15]. However, Zhuravlev et al [15] explain the TER of FTJs by the asymmetry of screening length of the electrodes. The asymmetry of screening length results in a difference in potential-barrier height between the positive and negative polarization states. However, the resistance of the positive and negative polarization states are equal. Therefore, the asymmetry of the screening length of electrodes is not an appropriate explanation of the on/off resistance ratio of AFTJs. The equal resistance of the positive and negative polarization states of an AFTJ asserts that the screening lengths of the electrodes are equal.

However, the asymmetric screening length of electrodes is not the only explanation of the TER of FTJs. Many other phenomena are investigated in the literature to explain the TER of FTJs besides the screening length. For example, there is a class of FTJs that exhibits a magnetoelectric effect (ME) at the ferroelectric and ferromagnetic interface [10]. To put it simply, the magnetization alignment at the interface is dependent on the electric polarization of the ferroelectric insulator. In other words, the LSMO electrode switches from ferromagnetic to antiferromagnetic alignment according to the direction of the ferroelectric polarization of the insulator. The relative alignment of the magnetization modulates the current similar to the tunneling magnetoresistance of magnetic tunnel junctions. However, this magnetoelectric effect is not an appropriate explanation of the AFTJ characteristic because of two reasons. First, the magnetoelectric effect results in high resistance in a

given electric polarization direction and low resistance for the other polarization direction. In contrast, the AFTJ resistance is equal in the positive and negative polarization states. Second, the magnetoelectric effect is noticed in $\text{La}_{0.5}\text{Sr}_{0.5}\text{MnO}_3$ which is different than the $\text{La}_{0.7}\text{Sr}_{0.3}\text{MnO}_3$ electrode of the AFTJ investigated in this study [10].

Another import factor that improves the TER in the case of FTJs is the built-in potential. The built-in potential introduces asymmetric electrostatic potential barrier that allows the modulation of the barrier height by the electric polarization [24]. However, the built-in potential results in different resistance at the positive and negative polarization states which is not consistent with the characteristics of AFTJs.

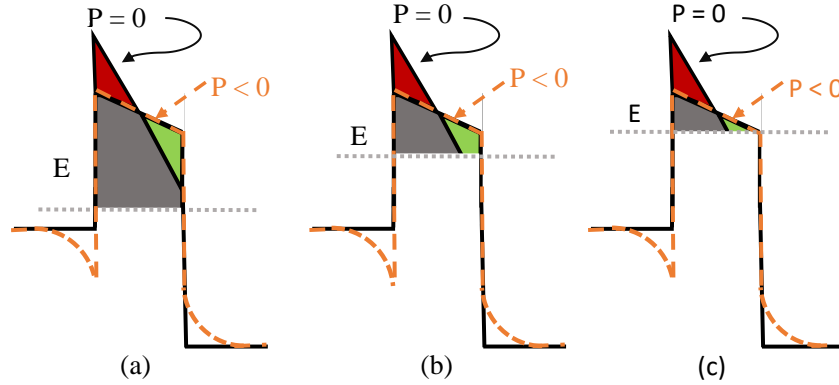


Figure 5.3. The electrostatic potential at $P = 0$ and $P < 0$. For the case of $P = 0$, the red triangular is added and the green one is subtracted. In the case of $P < 0$, the red triangular is subtracted and the green one is added. (a) Direct tunneling in both polarization states. (b) Direct tunneling in case of $P = 0$ and Fowler-Nordheim in case of $P < 0$. (c) Fowler-Nordheim tunneling current dominates in both polarization states.

In summary, the phenomena that are responsible for the TER of AFTJs are different from the phenomena that contribute to the TER of FTJs. As we mentioned before, asymmetric screening, built-in potential, and magnetoelectric effect could not produce such characteristics of AFTJ. However, the potential profile of the AFTJ has symmetric screening lengths and a relatively small built-in potential. Next, we show that the direct tunneling current is not the appropriate tunneling mechanism for the AFTJ investigated in this study. The only tunneling current that could produce such AFTJ characteristics is Fowler-Nordheim tunneling current.

The potential profile of an AFTJ is demonstrated in Fig. 5.3. An AFTJ has a rectangular barrier under zero bias conditions and zero ferroelectric polarization. The applied voltage deforms the rectangular potential and produces a trapezoidal barrier. The trapezoidal barriers of the positive and negative applied voltage are symmetric around the vertical axes. After applying the positive (negative) voltage by a few nanoseconds the polarization of the ferroelectric material switch from zero to the positive (negative) direction. The potential induced by the electric polarization of the insulator opposes the applied voltage. Therefore, the maximum height of the potential barrier is reduced but the minimum potential height also increases by the same amount, and hence the total area below the barrier is constant. In other words, the area removed from the barrier by the polarization induced potential is equal to the area added because of the symmetry of the potential barrier and the induced potential, as illustrated in Fig. 5.3 (a). According to the AWK approximation, the tunneling current is dependent on the area under the barrier. The area under the barrier does not change in case of direct tunneling. Consequently, direct tunneling is not the appropriate tunneling mechanism for such large TER of the AFTJ investigated in this study.

In contrast to the direct tunneling current, the Fowler-Nordheim tunneling current could results in a difference in the area under the potential barrier, as illustrated in Fig. 5.3(b) and (c). In the case of Fowler-Nordheim, the area added by polarization-induced potential is not equal to the area subtracted because of the asymmetric potential profile. Therefore, the area under the curve in case of positive and negative polarization is less than the area under the barrier in case of zero polarization. However, the area under the potential barrier at positive and negative polarization states are equal which complies with the experimental results.

As demonstrated in Fig. 5.3(c), the Fowler-Nordheim tunneling is the dominant current in both polarization states. The modulation of the area under the barrier is enhanced compared to the case of switching from direct to Nordheim tunneling that is demonstrated in Fig. 5.3 (b).

Interestingly, M. Alexe et al [61] estimated the barrier height of AFTJ by fitting the tunneling current model to experimental data. Their results demonstrate that the *Nordheim tunneling* has less area under the potential barrier and is responsible for the low resistance

state and *direct tunneling* has a larger area under the potential barrier. In this study, the *Fowler-Nordheim* tunneling is associated with the large area under the potential (high resistance state) and the *direct tunneling* is associated with the smaller area under the barrier (low resistance state). The model explained in this study is consistent with the device physics because we related the electrostatic potential to the free charge distribution and the bounded charge induced by the electric polarization.

The simulation results of the proposed model are illustrated in Fig. 5.4. The parameter used for the simulations of AFTJ current is listed in Table 5.1. Interestingly, the proposed model could accurately fit the experimental results.

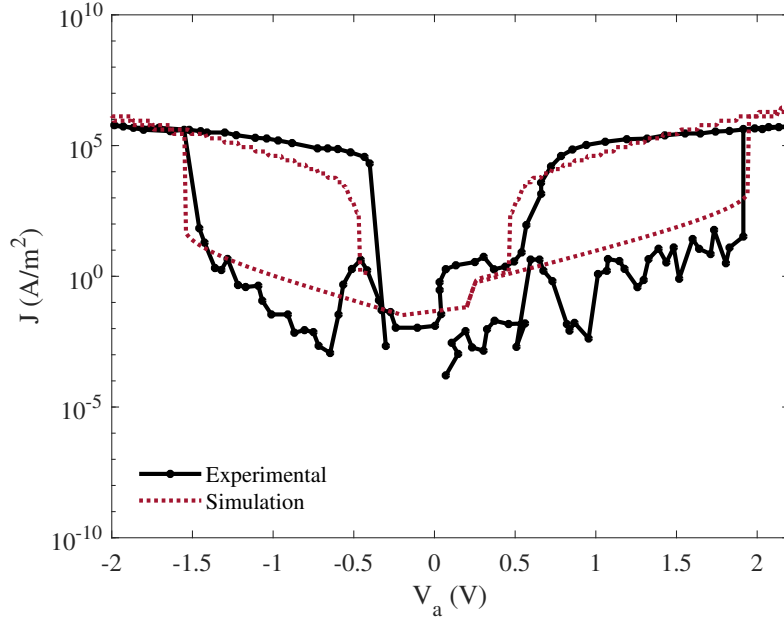


Figure 5.4. The simulation results and the experimental I-V characteristics of the AFTJ. The experimental I-V characteristic are published by M. Alexe *et al* [61].

5.2 Biasing AFTJ as an Oscillator

Let us describe the operations of the AFTJ as an oscillator. The AFTJ based oscillator is illustrated in Fig. 5.5. The oscillator consists of an AFTJ connected in series with a MOSFET transistor M_1 and a load capacitor C_{L1} . The AFTJ switches to the low resistance

Table 5.1. The list of the parameters values used for AFTJ simulations.

Parameter	Value	Parameter	Value
γ	0.3333 s/F	m	$9.11 \times 10^{-31} \text{ kg}$
f_a	$-102666 \times 10^3 \text{ m/F}$	T	300 K
f_b	$-153999 \times 10^3 \text{ m/F}$	U_B	0.9 eV
g	$3003 \times 10^5 \text{ m/F}$	$\frac{\sigma_s \delta_1}{\epsilon_0 \epsilon_{r1}}$	0.7 eV
h_a	$22774 \times 10^4 \text{ m}^5/(C^2.F)$	$\frac{\sigma_s \delta_2}{\epsilon_0 \epsilon_{r2}}$	0.7 eV
h_b	$432706 \times 10^3 \text{ m}^5/(C^2.F)$	t_d	6.1 nm
$Area$	$1 \text{ } \mu\text{m}^2$	β	10

state when the voltage on the AFTJ $|V_{AFTJ,1}|$ is higher than $V_{th,h}$. The AFTJ switches back to a high resistant state when the AFTJ voltage is less than $V_{th,l}$. Assuming that the initial voltage $|V_{AFTJ,1}|$ is zero, $V_1 = V_d$ and the resistance of the AFTJ is high. The capacitor C_{L1} starts to discharge from V_d to zero because the resistance of the path from V_1 to V_d through the AFTJ is higher than the resistance of the path to the ground through the transistor M_1 . When the voltage on the AFTJ is higher than $V_{th,h}$ the AFTJ switches to low resistance state. The switching of the AFTJ to the low resistance state makes the resistance of the path to V_d through the AFTJ lower than the resistance of path to ground through M_1 . Therefore, the capacitor C_{L1} starts charging. The capacitor C_{L1} charges until the voltage on AFTJ is lower than the $V_{th,l}$. When the AFTJ voltage $|V_{AFTJ,1}|$ is less than $V_{th,l}$, the AFTJ switches back to high resistance state and starts discharging the capacitor C_{L1} . Therefore, the AFTJ oscillates between high and low resistance states as the previous operation are repeated. Consequently, the voltage V_1 oscillates between the two voltage levels $V_{th,l}$ and $V_{th,h}$.

The previous qualitative discussion of the AFTJ operations as an oscillator could be explained formally using the terminology of nonlinear dynamics [71]. The I-V characteristics of the AFTJ and the transistor M_1 are projected over the bias voltage of AFTJ $V_{AFTJ,1}$ and drain voltage V_1 in Fig. 5.6. The transistor M_1 and the AFTJ are connected in series. The AFTJ current and the transistor current have to be equal. Therefore, the intersection point of the AFTJ current and M_1 current are expected to be candidate fixed points of the circuit. However, the classification of the fixed points as stable or unstable fixed points is dependent on the transistor biasing voltage $V_{ref,1}$ as well as the transistor size which is considered as

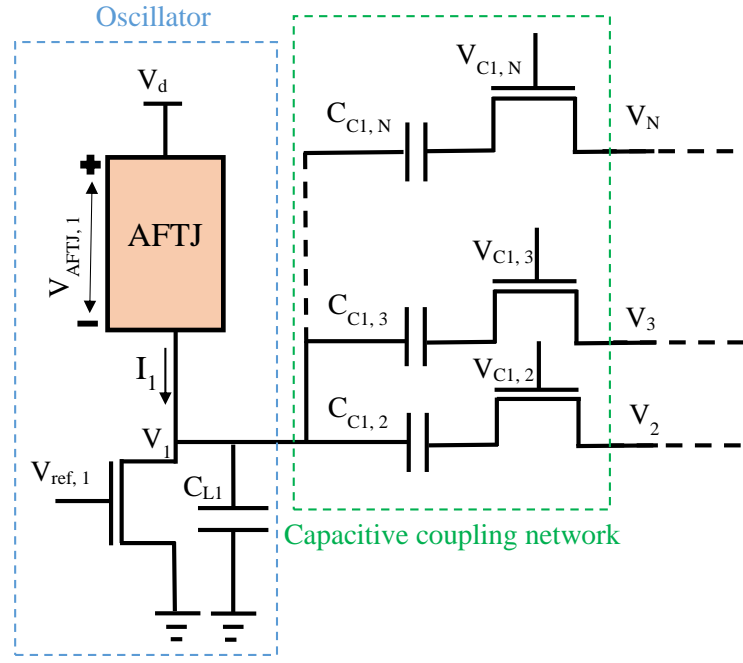


Figure 5.5. The AFTJ based coupled-oscillator network.

the bifurcation parameter. Fig. 5.6 illustrates different I-V characteristics at different values of the bifurcation parameter. The intersection points (fixed points) A and B in Fig. 5.6(a) are both saddle points as the direction of the change in the current is the same before and after these points. The change in the current happens at a constant voltage on these vertical hysteresis lines. The system state cannot change from charging to discharging or vice versa because the voltage of the oscillator is constant on these vertical lines. All the intersection points on the vertical lines $V_{AFTJ,1} = V_{th,l}$ and $V_{AFTJ,1} = V_{th,l}$ are saddle points in general. The two paths connecting the points A and B constitute a closed loop that means that the system oscillates.

As the bifurcation parameter increases, the point B migrates from the vertical line $V_{AFTJ,1} = V_{th,l}$ toward the part of the hysteresis loop that has a negative slope, as illustrated in Fig. 5.6(b). Therefore, the intersection point is changed from the saddle point B to a stable point B because the change in the current before and after B has opposite directions toward the point B . The loop ACB does not constitute an oscillatory system because of the stable point B . However, the system could still oscillate under certain temporal conditions. The condition of oscillation is that the charging time of C_{L1} is much less

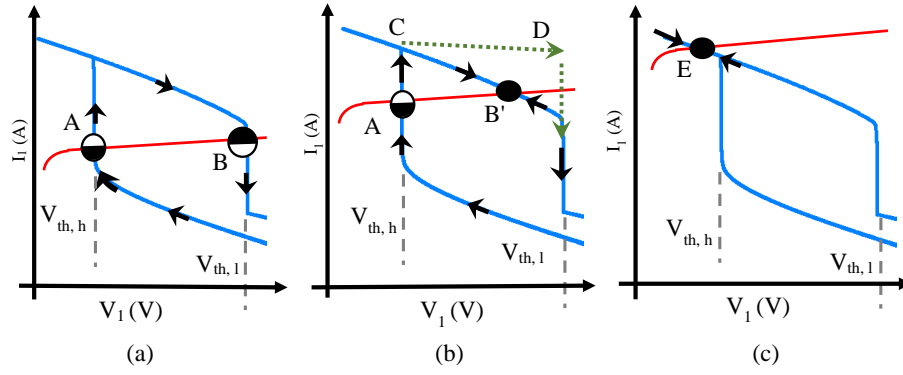


Figure 5.6. The AFTJ and the transistor M_1 I-V characteristics at different values of the bifurcation parameter. (a) The system has a single closed loop. (b) The system has two different cyclic paths ACD and ACB' . (c) The system has one stable fixed point.

than the ferroelectric polarization response time. Under this condition, The capacitor C_{L1} finishes charging before the AFTJ current could change (constant current path). Therefore, the AFTJ at transient time prefers the constant current charging path CD over the path CB . In contrast to the loop ACB (blue loop in Fig. 5.6(b)), the closed loop ACD does not have a stable fixed point. Consequently, the ACD loop shows the possibility of oscillatory motion.

At higher values of the bifurcation parameter, the fixed points A and B collide and annihilate to produce single stable point E , as illustrated in Fig 5.6 (c). In general, the AFTJ cannot oscillate for any load I-V characteristics that exist above or below the hysteresis loop. The comparison of different emerging oscillator technology is illustrated in Table 5.2.

Table 5.2. A comparison of different emerging oscillators with respect to power, area and frequency.

	AFTJ	VO_2 [62]	HfTaOx[63]	TaOx[64]
Power (μW)	<3	12	<50	<100
Area (μm^2)	1	0.89	0.5	0.5
Frequency (MHz)	4	9	350	500

The AFTJ power consumption shows significant improvement compared to other emerging oscillators. Interestingly, the power and the frequency of different oscillators show strong proportional relation. The reason behind this proportionality relation is that the device

with large resistance has lower current, and hence less power consumption. On the other hand, the large resistance of the device implies larger time constant of the circuit at constant load capacitance. The large time constant of the oscillator results in longer periodic time and lower oscillation frequency.

5.3 AFTJ based coupled-oscillator network

Let us explain the mapping between the coupled-oscillator network energy landscape and the chromatic number of the graph coloring problem. The coupling between different oscillators is done using a capacitor and a series transistor that works as a switch, as illustrated in Fig. 5.5. The transistor gate voltage $V_{Ci,j}$ is high if the corresponding element of the adjacency matrix of the graph $A_{i,j}$ is set to '1' and is grounded otherwise. The coupling capacitor between the nodes V_i and V_j causes a phase shift between the coupled oscillators. Every pair of coupled oscillators are assigned a different color because the phase of the capacitively coupled oscillators is different. The phase shifts between oscillators are redistributed to minimize the system energy by assigning a different phase to every pair of coupled oscillators, and hence a different color.

The previous explanation of the coupled-oscillator network approximation of graph chromatic number is demonstrated by the HSPICE circuit simulations. The AFTJ based-coupled oscillator solutions for different graph coloring optimization problem are illustrated in Fig. 5.7. The simulation is done using HSPICE circuit simulator. The physics-based model of the AFTJ described in section 5.1 is implemented using Verilog-A. The Verilog-A model of AFTJs is used in all HSPICE circuit simulations in this study.

A fully connected graph of three and four nodes is illustrated in Fig 5.7 (a) and (c). Interestingly, the oscillator has a phase shift of $\frac{2\pi}{3}$ and $\frac{2\pi}{4}$ for the case of three and four nodes fully connected graph, respectively. As mentioned before, every pair of coupled oscillator have to exhibit a phase shift. The phase of the 3 nodes connected graph has a phase shift of $\frac{2\pi}{3}$. The phase shift between the 3 nodes is redistributed to exhibit the maximum distance between the oscillators in the phase space to minimize the energy of the network. These simulation results agree with the previous discussion about mapping the energy landscape of the coupled-oscillator network and the chromatic number of the graph. Therefore, the

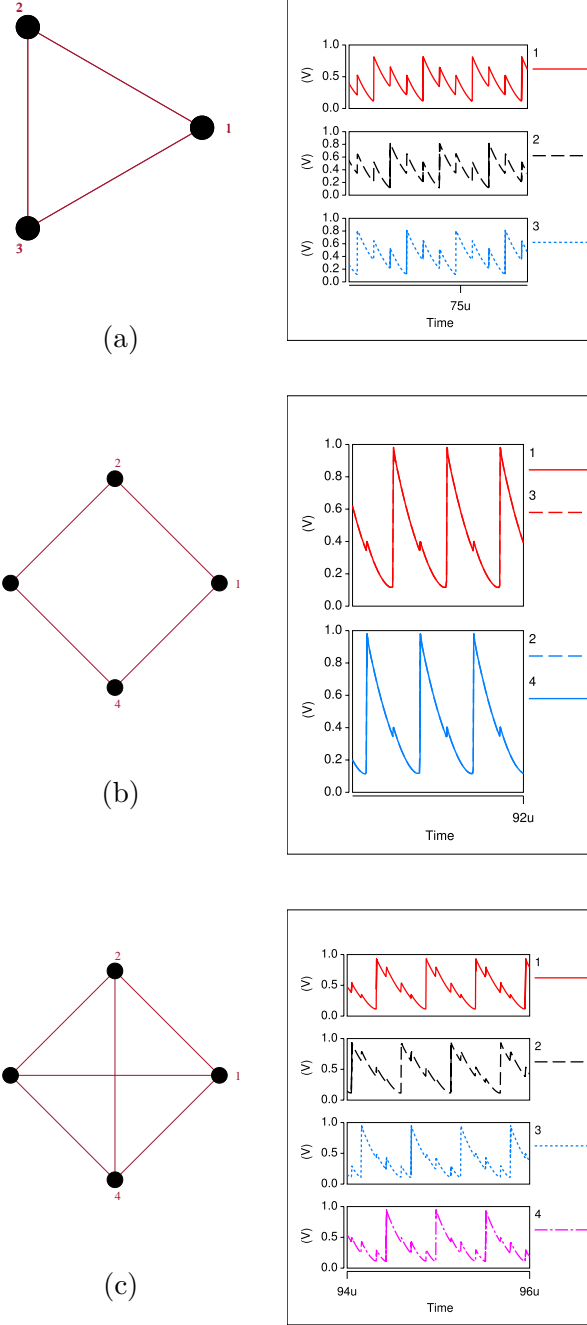


Figure 5.7. The hspice circuit simulation results for simple graph coloring problem using AFTJ based coupled-oscillator network. (a) Fully connected graph of three nodes. (b) Sparse graph of four nodes. (c) Fully connected graph of four nodes.

coupled-oscillator network could estimate the chromatic number of fully connected networks as expected.

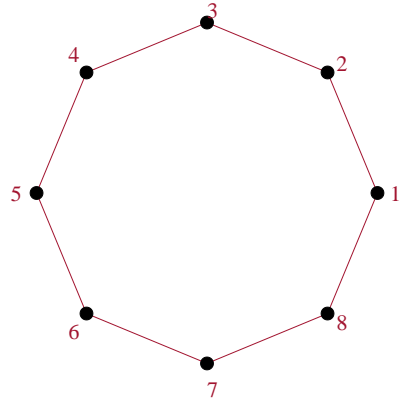
For the case of sparse four nodes graph, the coupled-AFTJ network is still able to accurately estimate the chromatic number, as illustrated in Fig. 5.7 (b). However, for higher-sparsity graphs, the accuracy of the coupled oscillator network is expected to decrease. The coupled-oscillator simulation results for a sparse pairwise connected graph of eight nodes is illustrated in Fig. 5.8 (a). Although the chromatic number of the graph is two, the phase of different oscillators within the same class has significant variance. The reason behind the large intra-class variance is due to lack of the force that attracts the uncoupled oscillator to exhibit the same phase due to sparsity. In contrast, the coupled oscillators have a force that pushes these oscillators away in phase space. Therefore, introducing a resistive coupling between the oscillators that are not connected in the adjacency matrix of the graph could reduce the intra-class variance [60]. However, this solution requires N^2 resistive pairwise connection. A more optimal solution is to introduce a single virtual node that has a resistive coupling to all other nodes. This reduces the number of required connection from N^2 to only N connections, as illustrated in Fig. 5.8 (b). Interestingly, the intra-class variance is reduced significantly.

The HSPICE circuit simulation for a graph from DIMACS [72] second implementation challenge is illustrated in Fig. 5.9. The graph has 11 nodes and 20 edges. The graph chromatic number is four. The AFTJ-coupled oscillator network could accurately estimate the chromatic number of the graph.

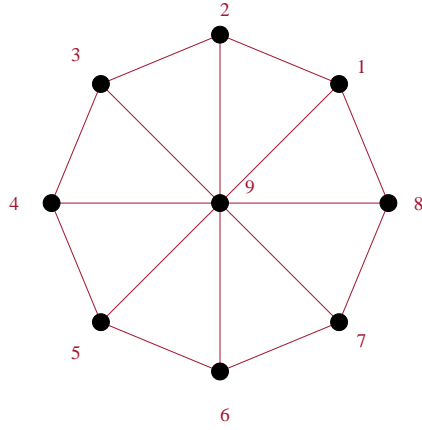
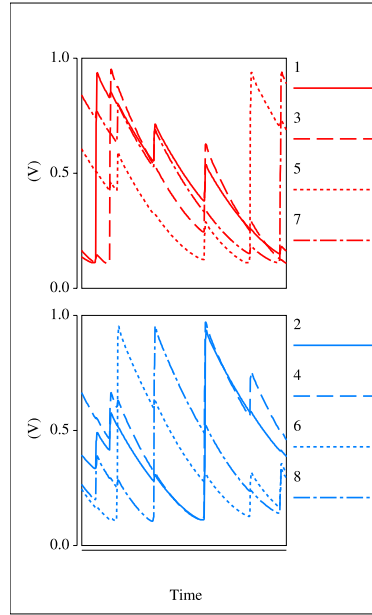
The HSPICE circuit simulation is not efficient for large graphs. The AFTJ circuit model requires fine time-step because of the antiferroelectric material response time. In contrast, the oscillation of AFTJ exhibits much larger periodic time because of the circuit time constant. Therefore, the simulation has a fine time-step and long simulation period. In addition, the circuit simulation time scales as the square of the number of nodes N^2 . Consequently, the circuit simulation is not efficient for large graphs. In the next section, we demonstrate an approximate version of the circuit model to solve large graphs with a reasonable efficiency.

5.4 The Approximate AFTJ Based coupled-oscillator network model

For large number of nodes, the HSPICE transient simulation is not efficient. Therefore, we used an approximate model that is appropriate for large graphs. The reduced circuit



(a)



(b)

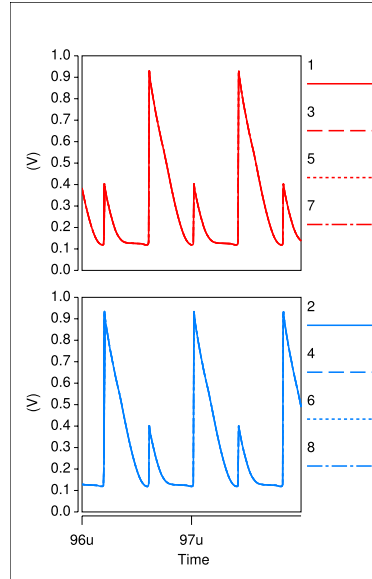


Figure 5.8. Sparse pairwise connected graph of eight nodes. (a) The coupled-oscillator network solution of the coloring problem. (b) The coupled-oscillator network solution of the same problem with extra virtual node is added to the graph.

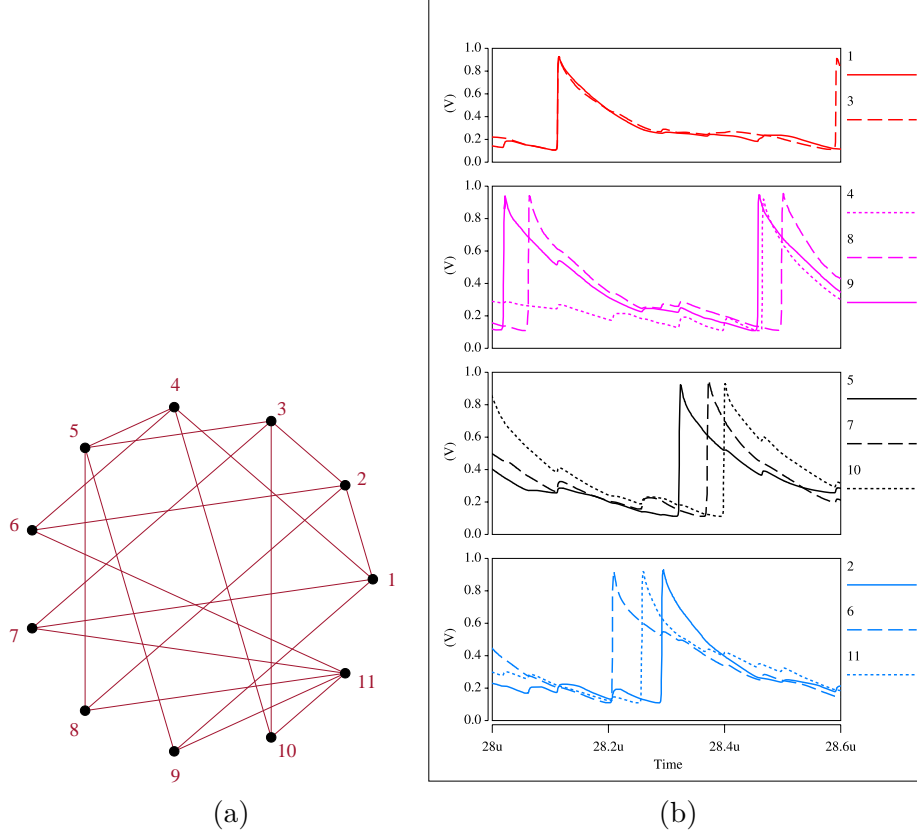


Figure 5.9. (a) Graph connections of myciel3. (b) AFTJ based coupled-oscillator simulation result for the graph myciel3.

model has the same topology as the original AFTJ based coupled-oscillator network, as illustrated in Fig. 5.10. However, the AFTJ is replaced by an average $R_{AFTJ,i}$, where $R_{AFTJ,i} = r_h$ at the high resistance state of the AFTJ (discharging), and $R_{AFTJ,i} = r_l$ at the low resistance state of the AFTJ (charging). The approximate circuit illustrated in Fig. 5.10 is a linear circuit. Therefore, we can apply the Kirchhoff's current law at each oscillator node V_1 to V_N and formulate N independent linear equations to be solved simultaneously. The coupled-oscillator network dynamics could be formulated in matrix form as [62]

$$\frac{dV(t)}{dt} = -(C_l + C_c)^{-1}[G(S)V(t) + H(s)], \quad (5.15)$$

where $V(t)$ is the vector of the voltages of oscillator $V(t) = [V_1(t), \dots, V_i(t), \dots, V_N(t)]$, S is the vector of the states of the oscillators $S = [S_1, \dots, S_i, \dots, S_N]$, $S_i = 1$ at low state of AFTJ

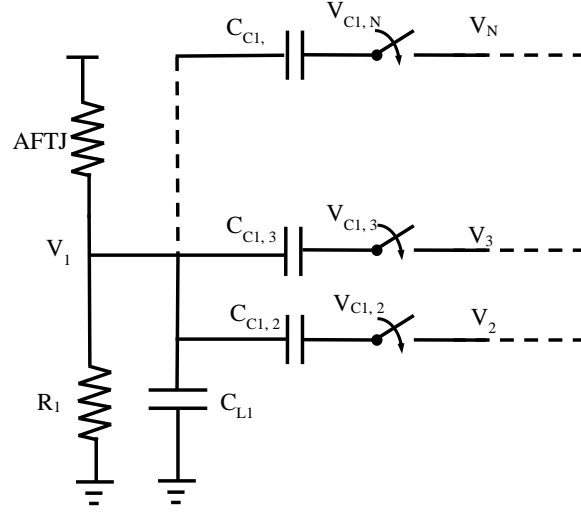
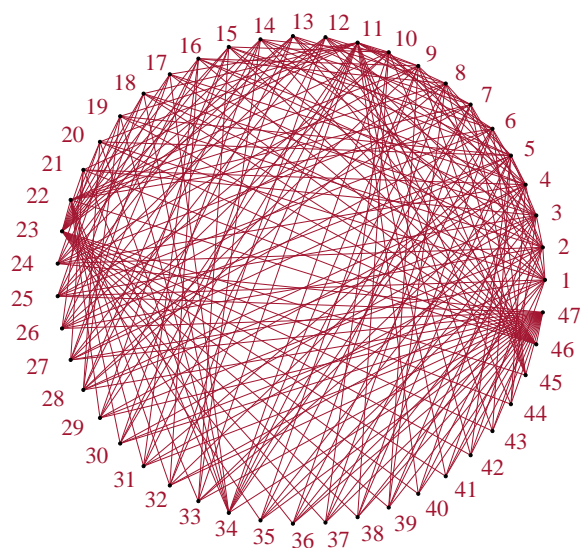


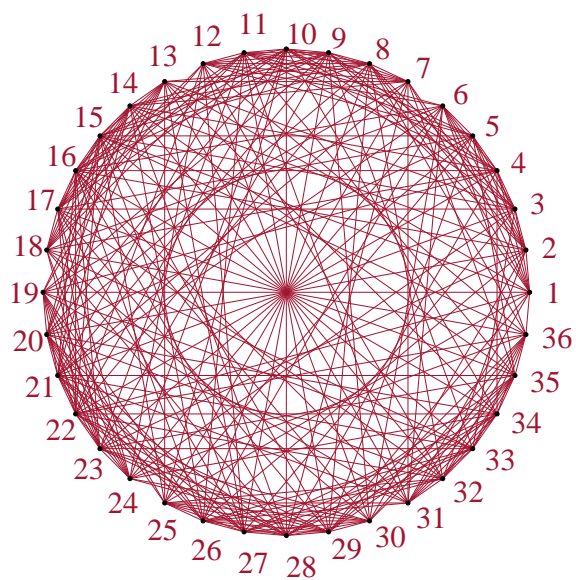
Figure 5.10. The approximate coupled-oscillator model. The AFTJ is replaced by an average resistance r_l and r_h for the low and high resistance states, respectively.

(charging), $S_i = 0$ at high resistance state of AFTJ (discharging), and C_l is a diagonal matrix with the k^{th} oscillator load capacitance at the k^{th} diagonal element. C_c is the coupling matrix that is defined as $C_c = c_c[D - A]$, where c_c is the coupling capacitance, A is the adjacency matrix of the graph, and D is diagonal matrix with the degree of k^{th} node at the k^{th} diagonal element of the matrix. $G(S)$ is a diagonal matrix. The diagonal elements of $G(S)$ are defined as $G_{i,i} = \frac{1}{R_{AFTJ,i}(S_i)} + \frac{1}{R_i}$.

The integration of (5.15) is done by 4th order Runge-Kutta method with constant time step. All the voltage are scaled by the V_d voltage. The phase of each oscillator is estimated by a time average XOR gate. The coupled-oscillator network is applied to a set of graphs from DIMACS implementation challenge. A sample of the DIMACS implementation challenge is illustrated in Fig. 5.11. The results of the coupled-oscillator network solution for a set of graphs from DIMACS data set is illustrated in Table 5.3. The results demonstrate the ability of the coupled-oscillator network to approximate the chromatic number of the graphs. As the number of nodes increases, the accuracy of the coupled-oscillator network is reduced. This reduction in accuracy is expected for large graphs because the solution space increases exponentially with the problem size. The increase in the size of the solution space increases the probability of settling at local minimum points.



myciel5



queen6_6

Figure 5.11. The myciel5 and queen6_6 graphs contain 47 nodes and 36 nodes, respectively.

Table 5.3. The results of the reduced model for practical graph coloring problem.

Graph	Nodes	edges	Chromatic Number:	
			Optimal	Proposed
huck	74	301	11	14
myciel3	11	20	4	4
myciel4	23	71	5	5
myciel5	47	236	6	7
myciel6	95	755	7	14
david	87	406	11	14
queen5_5	25	160	5	7
Queen6_6	36	290	7	11
Queen7_7	49	476	7	14
Queen8_8	64	728	9	19

6. A NEW OSCILLATOR COUPLING FUNCTION FOR IMPROVING THE SOLUTION OF GRAPH COLORING PROBLEM

Conventional Boolean computational methods are inefficient in solving complex combinatorial optimization problems such as graph coloring or traveling sales man problem. In contrast, the dynamics of coupled oscillators could efficiently be used to find an optimal solution to such a class of problems. Kuramoto model is one of the most popular mathematical descriptions of coupled oscillators. However, the solution to the graph coloring problem using the Kuramoto model is not an easy task. The oscillators usually converge to a set of overlapping clusters. In this section, we mathematically derive a new coupling function that forces the oscillators to converge to a set of non-overlapping clusters with equal distance between classes [73]. The proposed coupling function shows significant performance improvement compared to the original Kuramoto model.

Solving the class of nondeterministic polynomial time (NP) problems have been a challenging task for Boolean von Neumann computing [58], [74]. The solution space of such class of problems expands as an exponential function of the problem size. The sequential exploration of such large space to find an optimal solution is an exhaustive process. On the other hand, many systems in biology and physics could directly organize a population of primitive elements e.g., atoms or neurons in a minimum energy state or a set of synchronous clusters to accomplish certain functions [75]. These systems have a congenital self-organizing function that is distributed over the primitive constitutive elements. The distributed nature of such systems provides robust and parallel capabilities that aid the system to reach its optimally organized state.

One popular mathematical description of these biological systems is the coupled-population of oscillators formulated by Kuramoto [76]–[78]. Kuramoto model has been originally utilized to explain the behavior of certain chemical and biological systems. Recently, the model has been found applicable to the optimization of certain combinatorial problems e.g., graph coloring problem [60], [79].

The graph coloring problem is one of the classical computer science problems that have NP time complexity [80]. The graph coloring problem has been found applicable in many real-world problems [81]–[85]. The problem is defined as follows. Given a certain number of nodes that are connected to constitute a graph, determine the minimum number of colors that label each node in the graph with the constraint that the directly connected nodes have different colors. The minimum number of colors is the chromatic number of the graph. Although the problem has a short and simple description, the solution has NP time complexity that makes the problem with hundreds of nodes a challenging task for modern computers.

Wu [79] has shown the ability of a coupled-oscillator network to approximate the solution of the graph coloring problem. Each oscillator represents a node in the graph. The phase of the oscillator represents the color of the node. The oscillators have to converge to a set of clusters in the phase space. Each cluster of oscillators represents a set of nodes that can be colored with the same color. To approximate the solution of the graph coloring problem, the oscillator clusters have to satisfy the following properties: First, each cluster has to have the minimum intra-cluster phase difference between the members of the cluster. Second, the inter-cluster phase difference has to be maximized. However, these properties are not always granted by the formulation of the Kuramoto model. The oscillators could converge to a number of clusters that is different from the chromatic number depending on the strength of the coupling between oscillator. Moreover, the clusters are not well defined due to the spread of the cluster members over a wide range of phases. This spread may result in overlap between clusters.

In this section, we derive an oscillator coupling function that forces the oscillators to converge to clusters that have minimum intra-cluster spread with maximum inter-cluster distance. The results show a significant performance improvement compared to the original Kuramoto model.

The proposed coupling function is formulated as follows. **First**, we formulate the *density function* of the oscillators that has minimum intra-cluster distance and maximum inter-cluster distance. **Second**, we formulate the interaction between the oscillators in *the general form*. Third, we substitute by the *density function* from the first step in the

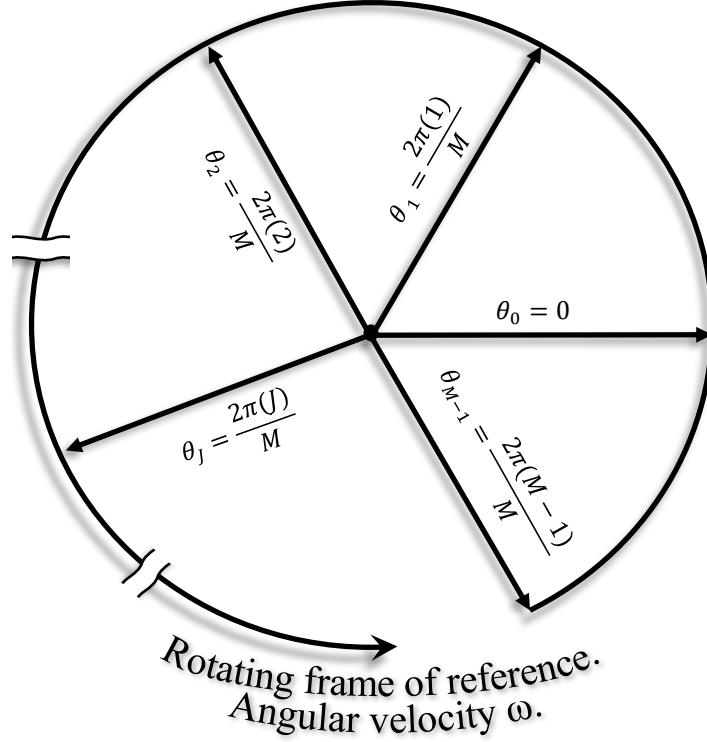


Figure 6.1. The final oscillator density (6.4) relative to a frame of reference is rotating with angular velocity ω .

general interaction form from second step to derive the corresponding coupling function. Finally, we discuss the stability of the solution.

We assume a set of N oscillators that have an equal natural frequency ω , and a phase θ_i , where $i = 1, 2, \dots, N$. In case of strong coupling condition, the phase shift between oscillators is constant, and hence we can write the phase of each oscillator as

$$\theta_i = \omega t + \theta_{0,i}, \quad (6.1)$$

where $\theta_{0,i}$ is the constant phase shift between oscillator i and the origin under steady-state condition. In the case of continuum $N \rightarrow \infty$, we can redefine θ as

$$\theta = \omega t + \theta_0. \quad (6.2)$$

Now, we define the steady-state oscillators density function. For a graph that has chromatic number M , the solution density function has to be a superposition of M delta functions to achieve zero intra-class distance. The maximum distance between the M classes has to be $2\pi/M$ which is the maximum possible distance. Therefore, we can define the density of oscillators ρ as

$$\rho(\theta_0, t) = \sum_{J=0}^{M-1} C_J \delta \left(\omega t + \theta_0 - \frac{2\pi J}{M} \right). \quad (6.3)$$

where C_J is a constant proportional to the number of oscillators in the class J . The density ρ consists of M delta functions that rotate with a constant angular velocity ω . To simplify the problem, we transfer the equation to a frame of reference that rotates with angular velocity ω . The density function ρ is defined relative to the rotating frame of reference as

$$\rho(\theta_0) = \sum_{J=0}^{M-1} C_J \delta \left(\theta_0 - \frac{2\pi J}{M} \right). \quad (6.4)$$

The density function $\rho(\theta_0)$ is illustrated in Fig. 6.1.

The time derivative of the phase of an oscillator (6.2) is formulated as

$$\dot{\theta} = \omega + \dot{\theta}_0, \quad (6.5)$$

where $\dot{\theta}$ and $\dot{\theta}_0$ are the time derivative of θ and θ_0 , respectively. The term $\dot{\theta}_0$ represents the influence of interaction between oscillators that drives the system to steady-state then it vanishes. Therefore, we define $\dot{\theta}_0$ as

$$\dot{\theta}_0 = \int_0^{2\pi} \rho(\phi_0) f(\phi_0 - \theta_0) d\phi_0, \quad (6.6)$$

where ϕ_0 is an arbitrary integration variable over the phase space, and $f(\phi_0 - \theta_0)$ is the coupling function between the oscillators that have phases ϕ_0 and θ_0 . We substitute by the definition (6.4) in (6.6) to get

$$\dot{\theta}_0 = \int_0^{2\pi} \sum_{J=0}^{M-1} C_J \delta \left(\phi_0 - \frac{2\pi J}{M} \right) f(\phi_0 - \theta_0) d\phi_0. \quad (6.7)$$

The order of the integration and the summation could be exchanged to evaluate the integration analytically as follows

$$\dot{\theta}_0 = \sum_{J=0}^{M-1} C_J f\left(\frac{2\pi J}{M} - \theta_0\right). \quad (6.8)$$

The steady-state condition is defined as $\dot{\theta}_0 = 0$ at $\theta_0 = \frac{2\pi i}{M}$ for $i = 1, 2, \dots, M$. A possible ansatz of f that satisfies the steady-state condition for arbitrary value of C_J is

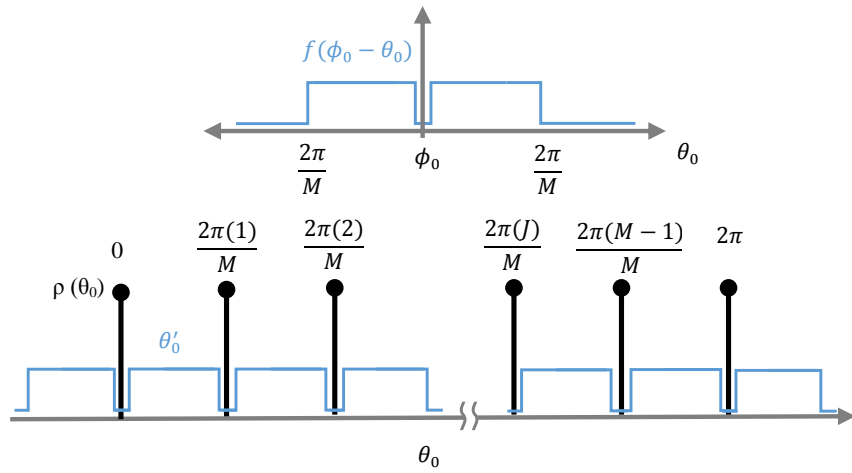
$$f(\phi_0 - \theta_0) = \begin{cases} 0, & \phi_0 = \theta_0 \\ \Gamma_{\frac{4\pi}{M}}(\phi_0 - \theta_0), & o.w., \end{cases} \quad (6.9)$$

where $\Gamma_{4\pi/M}$ is a rectangular function of width $4\pi/M$, as illustrated in Fig. 6.2a. The function f defined in (6.9) satisfy the steady-state condition $\dot{\theta}_0 = 0$ at $\theta_0 = \frac{2\pi i}{M}$ for $i = 1, 2, \dots, M$ that could be confirmed by inspecting equation (6.8). However, the function defined in (6.9) is an even function. The even interaction function results in the acceleration of the coupled oscillators in the same direction, and hence they maintain a constant phase difference. Therefore, the term $\dot{\theta}_0$ does not vanish and the system never reaches the steady-state. In contrast, an odd interaction function accelerates the coupled oscillators in opposite directions. Consequently, the distance between the oscillators in the phase space increases until they reach the steady-state where $\dot{\theta}_0$ vanishes, as illustrated in Fig. 6.2b. Therefore, we define f as

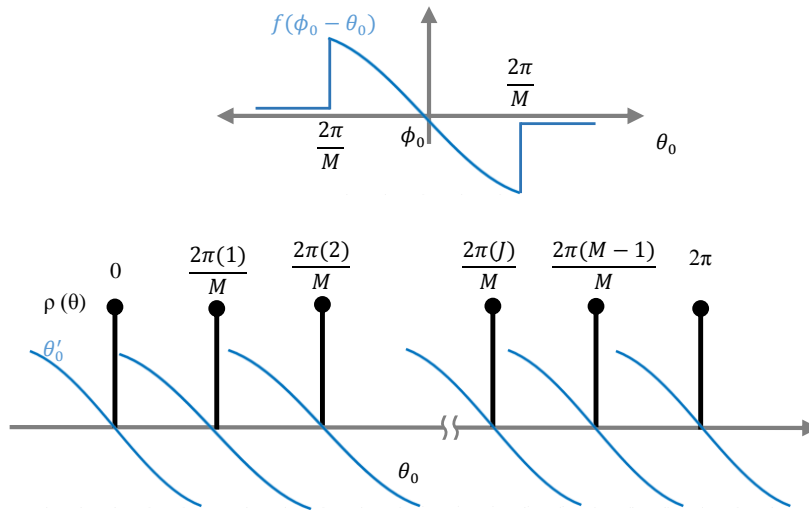
$$f(\phi_0 - \theta_0) = \Gamma_{\frac{4\pi}{M}}(\phi_0 - \theta_0) \sin(\phi_0 - \theta_0), \quad (6.10)$$

We can get the final oscillator coupling equation by substituting (6.10) in (6.4) and convert the integration to summation as follows

$$\dot{\theta}_i = \omega + C_{ik} \sum_k^N \Gamma_{\frac{4\pi}{M}}(\theta_k - \theta_i) \sin(\theta_k - \theta_i). \quad (6.11)$$



(a)



(b)

Figure 6.2. The oscillator density function and the coupling function. (a) Even coupling function. (b) Odd coupling function.

The oscillator network has two outputs: the chromatic number and the coloring schema. The chromatic number is an input parameter of the proposed coupling function M and is an output parameter at the same time. We estimate M using an iterative procedure discussed in Section 3.

The circuit-level implementation of the proposed coupling function is simple. According to the coupling function in equation (6.10), the coupling between two oscillators has to be switched off if the phase difference between the two oscillators is higher than $\frac{2\pi}{M}$. The phase difference between the oscillators may be measured using an XOR gate followed by an integrator that consists of a resistor and a shunt capacitor. The output of the integrator is proportional to the phase difference between the two oscillators. The output of the integrator controls a switch that could turn off the coupling between the two oscillators.

6.1 Stability analysis

In this section, we discuss the stability of the final state of the oscillators. We assume that the graph under investigation has a chromatic number M . In the case of steady-state motion, the oscillators are distributed according to the density function formulated in (6.4). First, we substitute the coupling function (6.10) in (6.8) as follows

$$\dot{\theta}_0 = \sum_{J=0}^{M-1} C_J \Gamma_{\frac{\pi}{M}} \left(\frac{2\pi J}{M} - \theta_0 \right) \sin \left(\frac{2\pi J}{M} - \theta_0 \right). \quad (6.12)$$

We focus our investigation on a single oscillator i that belongs to class J . This assumption does not limit the generality of the analysis because we did not assume any specific properties of the oscillator i and the class J . The summation in (6.12) can be reduced for specific oscillator i as follows

$$\begin{aligned} \dot{\theta}_{0,i} &= C_{J-1} \Gamma_{\frac{\pi}{M}} \left(\frac{2\pi(J-1)}{M} - \theta_{0,i} \right) \sin \left(\frac{2\pi(J-1)}{M} - \theta_{0,i} \right) + \dots \\ &\quad C_J \Gamma_{\frac{\pi}{M}} \left(\frac{2\pi J}{M} - \theta_{0,i} \right) \sin \left(\frac{2\pi J}{M} - \theta_{0,i} \right) + \dots \\ &\quad C_{J+1} \Gamma_{\frac{\pi}{M}} \left(\frac{2\pi(J+1)}{M} - \theta_{0,i} \right) \sin \left(\frac{2\pi(J+1)}{M} - \theta_{0,i} \right). \end{aligned} \quad (6.13)$$

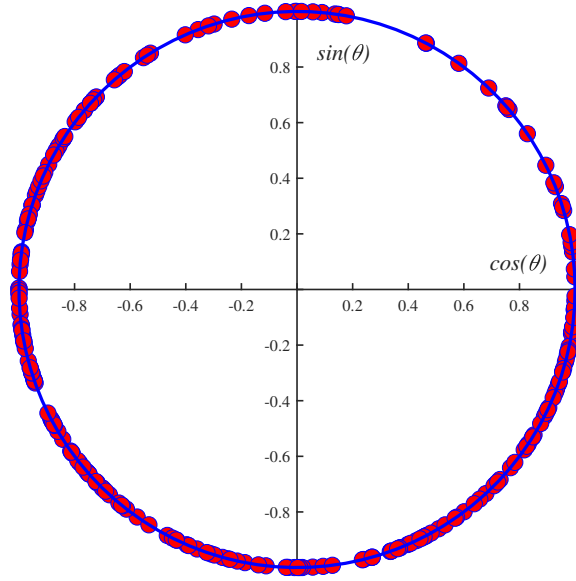
The oscillator i belongs to the class J , and hence $\theta_{0,i} \approx \frac{2\pi J}{M}$. No edge connects the oscillator i and any oscillator in the class J because they belong to the same class. Therefore, the second term in (6.13) that represents the interaction between oscillator i and the oscillators in the class J has to vanish.

Let us now investigate the behavior of the remaining two terms in (6.13). In the case of **a small positive perturbation** $+\eta$, the phase of the oscillator i is $\theta_{0,i} \approx \frac{2\pi J}{M} + \eta$. The first term in (6.13) is vanishing because of the rectangle function. The third term is negative, and hence $\theta_{0,i}$ decreases toward $2\pi J/M$. In the case of **a small negative perturbation** $-\eta$, the first term is positive and the third term is 0, and hence $\theta_{0,i}$ increases toward $2\pi J/M$. In other word, the points $2\pi J/M$ for $J = 1, 2, \dots, M$ are stable points. Note, these points are stable relative to a rotating frame of reference, as illustrated in Fig. 6.1. In other words, The stability of theses points relative to the rotating frame of reference does not contradict with the oscillatory behavior of the system relative to the original frame of reference.

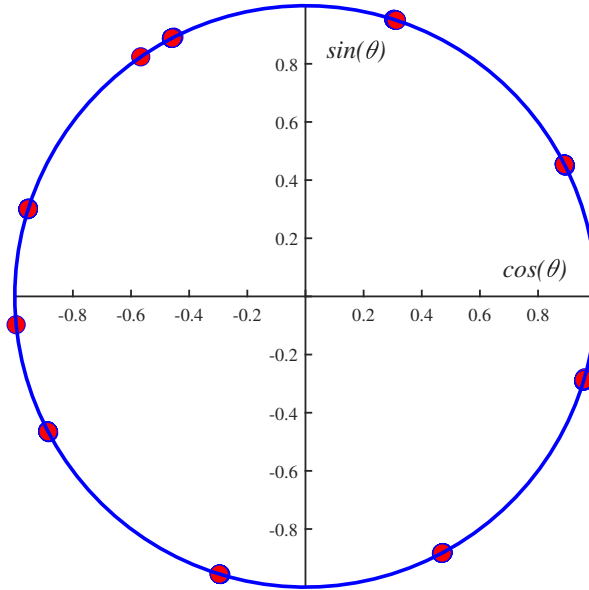
6.2 Simulation Results and Discussion

In this section, the graphs from DIMACS[72] second implementation challenge are used for numerical simulations. The numerical integration of the initial value problem is implemented using the 4th order Runge-Kutta method with a constant time step. The simulation results of the original Kuramoto model and the proposed coupling function are illustrated in Fig. 6.3a and Fig. 6.3b, respectively for the graph QUEEN8 from DIMACS[72]. The graph QUEEN8 has 64 nodes, 728 edges, and a chromatic number of 9 colors. Interestingly, the simulation results confirm our theoretical analysis. The proposed model forces the oscillators to converge to a set of distinct clusters with minimum intra-cluster phase distance and maximum inter-clusters distance, as illustrated in Fig 6.3b. In contrast, the limits between clusters are not easy to identify in the case of the original Kuramoto model, as illustrated in Fig 6.3a.

Although the proposed model results in 9 clusters which is equal to the graph chromatic number, some of these classes may contain nodes that can not have the same color. In other words, there are errors in the color assignment schema. The original Kuramoto model also has errors in the color assignment schema. Therefore, we need to define a criterion that



(a)



(b)

Figure 6.3. The graph coloring results for QUEEN8 that contains 64 nodes, 728 edges, and chromatic number of 9 colors. The parameters used are the same for both results. (a) The Kuramoto model has no clear separation between classes. (b) The proposed model has a clear 9 distinct classes.

effectively quantifies the performance of the proposed model. For a fair comparison, we adopted the criterion suggested in [62] as we explain in the following discussion.

The results of the original Kuramoto model does not show a distinct limit between classes. Therefore, a post-processing step is applied to the results. The post-processing is defined as follows. First, the final phase of the oscillators is sorted in ascending order. Second, the list of ordered phases is scanned in sequential order. Third, the scanned oscillator is added to the class l as long as the oscillator does not have a direct connection to the oscillators in that class. Forth, the third step is repeated until we reach an oscillator that has a direct connection to any oscillator in class number l . Then, we increment the class index $l = l + 1$ and add the oscillator to the new class and go back to the third step. The final number of clusters is considered as an estimate of the chromatic number. The post-processing step does not affect the performance of the algorithm as it has a polynomial time complexity.

The results of both models are dependent on the initial phase of the oscillators. Therefore, we selected the initial phases randomly from a uniform distribution. For each graph, we repeat the simulation for 1000 different initial phases and select the minimum chromatic number for both models. The same steps are applied to both models for a fair comparison. The results of the simulation are illustrated in Table 6.1. The performance of the proposed model is strictly better than the original model for all graphs. The difference in performance between the two models is higher in the case of large graphs. The approximate solution could predict the optimal chromatic number for small size graphs. In contrast, the approximate chromatic number of both methods is higher than the optimal solution in the case of large size graphs.

The initial distribution of oscillator phases has a major effect on the final solution. In general, the initial point of any optimization algorithm is a major factor that may lead the optimization algorithm to get stuck at local minima or reaches the global minima. On the other hand, the sparsity of the graph increases the number of valid solutions of the graph coloring problem. Therefore, some of the oscillators have fewer constraints and may randomly get stuck at a single phase out of a range of possible phases.

Wu et al proposed a positive nonzero value of the parameter C_{ik} to couple unconnected nodes on the graph [60]. They used a grid search to find the value of the positive and

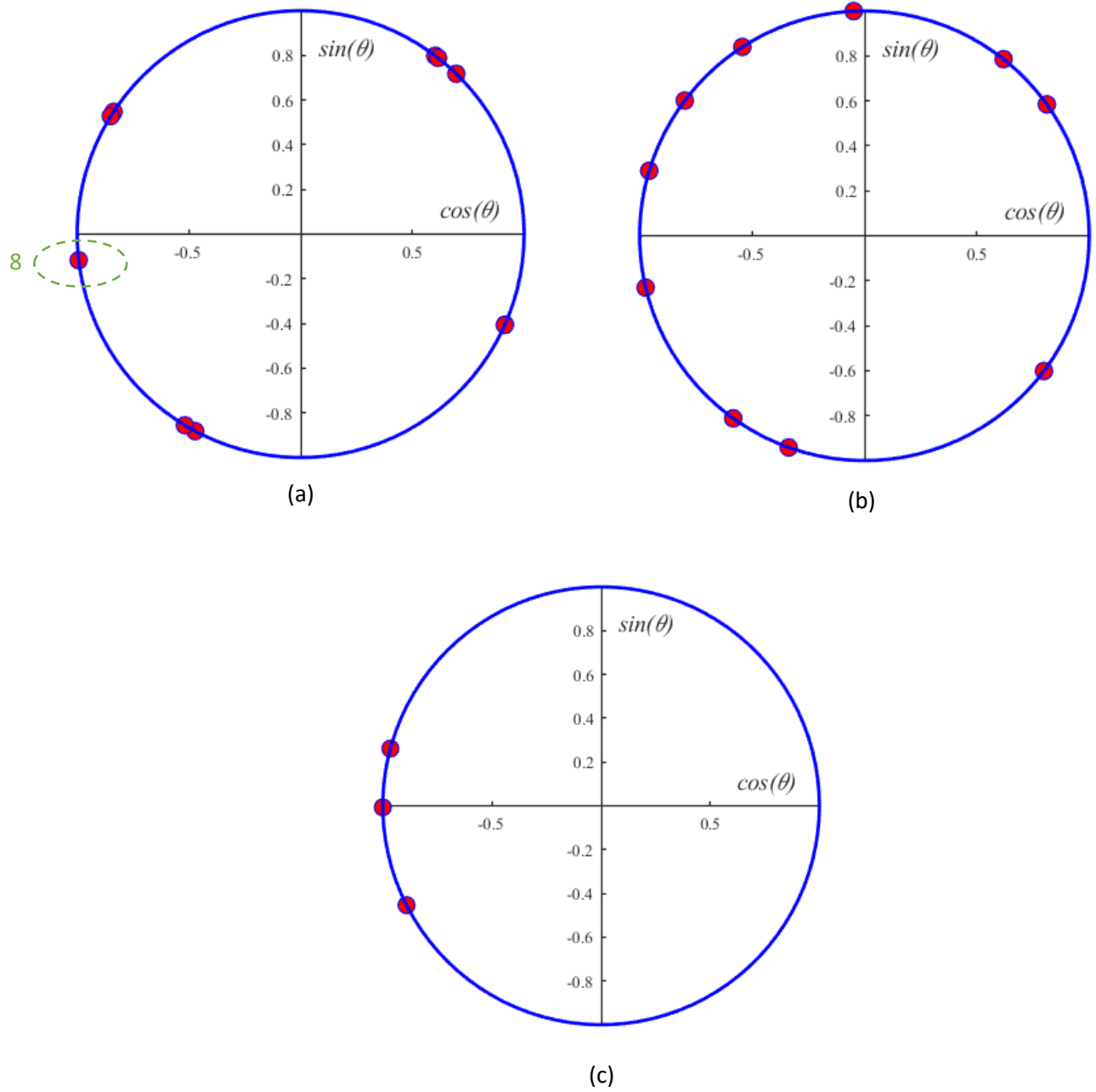


Figure 6.4. The simulation results of the graph myciel3. (a) The results of the proposed coupling function where $C_{ik} = 0$ for unconnected nodes and $C_{ik} = -16$ for connected nodes. (b) The results of the Kuramoto model where $C_{ik} = 23$ for unconnected nodes and $C_{ik} = -16$ for connected nodes. (c) The results of the Kuramoto model where $C_{ik} = 24$ for unconnected nodes and $C_{ik} = -16$ for the connected nodes.

Table 6.1. The results of the proposed model compared to the Kuramoto model.

Graph	Nodes	edges	Chromatic Number:		
			Optimal	Kuramoto	Proposed
huck	74	301	11	18	11
myciel3	11	20	4	4	4
myciel4	23	71	5	5	5
myciel5	47	236	6	6	6
myciel6	95	755	7	7	7
david	87	406	11	15	11
Queen5	25	160	5	7	5
Queen6	36	290	7	10	8
Queen7	49	476	7	15	10
Queen8	64	728	9	20	12

negative weights C_{ik} that minimize the intra-class distance. The simulation results of that grid search algorithm are illustrated in Fig. 6.4 (b). The distance between the classes is not uniform. The process of finding the optimal value of C_{ik} is not easy. A small change in the value of C_{ik} forces all the oscillators to have the same phase, as illustrated in Fig. 6.4 (c). In contrast, our proposed coupling function (6.10) shows 4 distinct classes, as illustrated in Fig. 6.4 (a). Note, the oscillator 8 marked by the green oval does not constitute a separate class. However, oscillator 8 could belong to the class that follows it or the one that proceeds it because of the sparsity of the graph.

Finally, we mentioned earlier that the chromatic number of the graph is an output of the oscillator network and is an input parameter of the proposed coupling function M . Toward resolving this conflict, we propose a binary search criterion that starts from an educated guess of the start and the end of an interval that includes the chromatic number. The initial guess of the chromatic number has to be tested by solving the problem using the oscillators network. The algorithm continues testing different values in the interval between these initial limits using a binary search. A higher (lower) next guess of the chromatic number can be selected if the classification error is higher (lower) than the required target. The search process ends if an acceptable classification error is reached.

7. PROPOSAL FOR AN AREA-EFFICIENT NON-VOLATILE FLIP-FLOP BASED ON SPIN HALL EFFECT

Recently, systems that rely on energy harvested from ambient sources are gaining increased attention due to their possible usage in numerous low power applications including Internet of Things (IoT). Owing to the unreliable nature of such ambient energy sources, these systems suffer from supply voltage degradations and power-cutoffs. Therefore, the computational scheme for such energy harvesting systems is divided into small incremental steps along with non-volatile memory elements that conserve the data between subsequent power-cutoffs. Towards that end, in this section, we propose a new non-volatile flipflop (NVFF) that exhibits better energy efficiency and denser area as compared to previous works [86]. The proposed NVFF utilizes a single spin Hall effect based magnetic tunnel junction (SHE-MTJ) due to its favorable device characteristics like high spin injection efficiency and decoupled read-write paths [86]. Furthermore, we also propose a new restore mechanism, wherein a CMOS inverter is used as a *gain element* to attain robust restore operation with single SHE-MTJ per NVFF. A detailed device-circuit simulation including variational analysis is reported to ascertain the robustness of the proposed NVFF.

Attempts to design energy harvesting systems have relied on the unprecedented progress in realizing ultra-low power electronics enabled by the CMOS technology [87] and the present emphasis on applications like smart cities and Internet of Things (IoT) [88]. However, the fragile nature of the ambient energy sources exposes the underlying circuits to supply voltage degradations and power cutoffs. Therefore, these systems use an alternative computational scheme, wherein the computing time is divided into set of small time slots based on the availability of the ambient power source, along with non-volatile memory elements that hold the data during power outages. As such, the system has to be equipped with non-volatile memories like FLASH, resistive RAMs (ReRAMs), phase change memories (PCM) or spin transfer torque magnetic RAMs (STT-MRAM) [89].

Besides the inferior performance of these non-volatile memories, the transfer of data between the computational core and the non-volatile memory storage over a long bus limits the performance of the system due to the well known von-Neumann bottleneck. Intuitively,

the von-Neumann bottleneck can be mitigated to certain extent by moving the non-volatile memory elements close to the computing cores. Towards this goal, a class of non-volatile flip-flops (NVFF) that are in close proximity with the computing circuits are being extensively investigated [90]–[93]. Such NVFFs aim to save and restore the computed data from the computing cores *in-situ* in a massively parallel manner through the non-volatile elements.

The most well know conventional non-volatile FLASH memories are based on injecting charges in a floating gate by Fowler-Nordheim tunneling mechanism [66]. The Fowler-Nordheim tunneling process requires high voltage in range of 12V that impairs the power dissipation and slows down the performance. On the other hand, emerging non-volatile technologies like the STT-MRAM, the ReRAMs *etc.* exhibits lower read and write voltages compared to the FLASH memory.

Out of all known emerging non-volatile technologies, STT-MRAM exhibits almost unlimited endurance which is a key metric for the extreme longevity requirement of energy harvesting systems. In addition, the back-end-of-line CMOS process compatibility and higher areal density of the STT-MRAM adds to its advantages. Consequently, STT-MRAM is contemplated as future replacement for conventional non-volatile memory [94]. Furthermore, more efficient MRAM write mechanisms are recently emerging in literature like the Spin Hall Effect (SHE) mechanism that utilizes the spin Hall phenomena to convert the charge current to spin-polarized current [95]. At the same time, SHE based Magnetic Tunnel Junction (MTJ) has separate read and write current paths that allow optimizing both paths in a decoupled manner to improve the read margin and the write efficiency, simultaneously.

Let us summarize some of the previous works related to NVFFs. NVFFs using ReRAMs and PCM elements can be found in [96], [97], respectively. The early published work on NVFF based on STT based magnetic tunnel junction (STT-MTJ) was presented in [91]. However, STT-MTJ has a write current in range of hundreds of micro-amperes [98] which is a limiting factor, in addition to its coupled read and write paths that complicate circuit design. SHE-MTJ based NVFF has been considered recently in literature [93], [99], [100]. SHE-MTJ has higher spin current injection efficiency compared to STT-MRAM which makes it more attractive. Further, more recently complex complementary polarized magnet MTJ devices are also considered for NVFF in [101], [102]. Although, the complex stack of the

complementary polarized magnet MTJ provides attractive and efficient capabilities, they require complex device structures raising large scale fabrication concerns. Recently, it was demonstrated in literature that more than 2x areal density improvement could be achieved for SHE-MTJ based MRAM [103].

In this section, we propose a new SHE based NVFF that has $\sim 3.2\times$ energy and $\sim 1.6\times$ area improvement compared to the previously published work [99]. The work in [99] can be considered as a representative work with respect to SHE based NVFF due to its differential operation as well as simple circuitry. Majority of the work related to nonvolatile flipflop in literature utilized differential read and write operations [104]. Instead of utilizing differential read and write operations that consume extra power, a single SHE-MTJ is used for the proposed NVFF which improves the power dissipation and area efficiency. Although the non-differential read has less read margin compared to differential read, the proposed NVFF uses tightly coupled CMOS inverters as *gain element* to enhance the robustness of the read process. The robust behavior of our proposed read mechanism has been confirmed by extensive Monte-Carlo analysis.

7.1 The SHE-MTJ Device

Spin Hall effect is a phenomena that originates due to spin orbit coupling (SOC) [105]. A charge current propagating in a heavy metal splits into up-spin and down-spin current due to spin dependent scattering owing to the SOC phenomenon. If such a heavy metal is in physical contact with an adjoining ferromagnet, the spin current at the interface between the heavy metal and ferromagnet junction exerts spin torque on the ferromagnet that could switch its magnetization similar to the STT phenomenon. The spin injection efficiency of the SHE mechanism is much higher than the conventional STT phenomenon [106].

The SHE-MTJ that is used for the proposed NVFF has elliptic shaped nanomagnet that has minor axis diameter of 20 nm, major to minor diameter ratio of 3, and free layer thickness of 2.4 nm, as shown in Fig. 7.1. The MTJ stack consists of a *free* ferromagnet (FL) and a *pinned* ferromagnet (PL) separated by a non-magnetic spacer. A parallel (anti-parallel) orientation of the PL and FL results in low (high) resistance. The dimensions of the free layer are selected to achieve in-plane anisotropy and an energy barrier of $> 60KT$ that grants

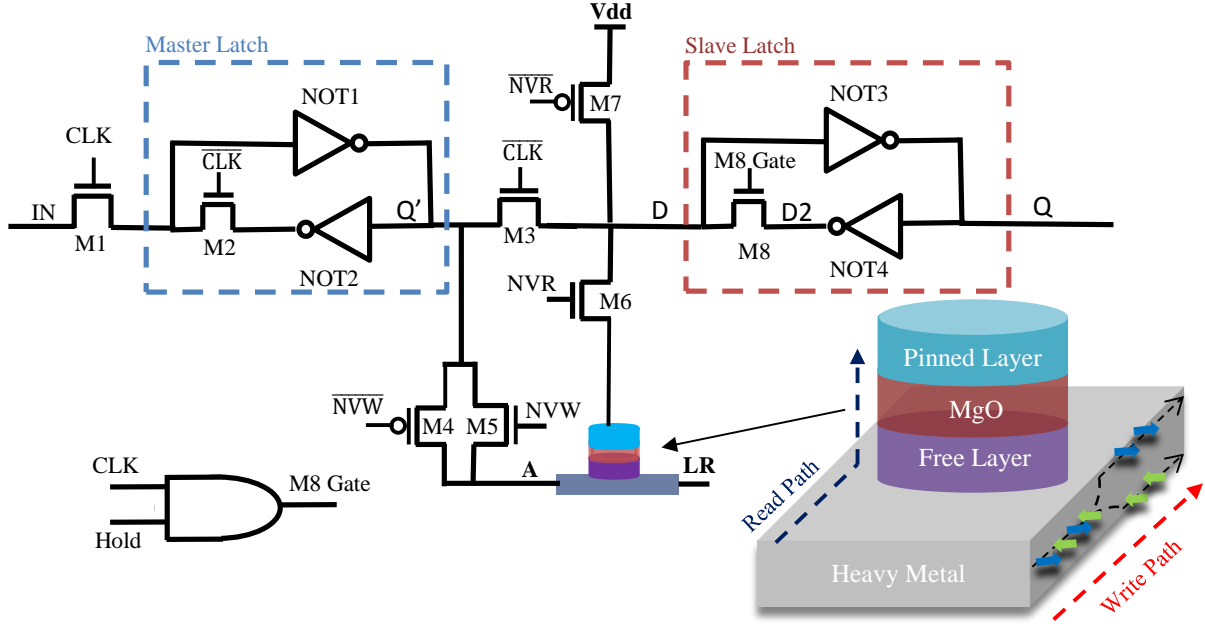


Figure 7.1. The proposed circuit of the NVFF. The SHE-MTJ is included as inset. The V_{dd} is 1.1 V.

more than 10 years retention time. The MTJ stack is based on the experimental study [107] for the well-known Ta, CoFeB, and MgO heterostructure that has the following parameters: saturation magnetization (M_s) is 1257.3 emu/cm^3 , interfacial anisotropy (K_i) is 1.3 erg/cm^2 . Also based on the non-equilibrium Green's function compact resistance model presented in [108], the MgO oxide thickness was chosen to be 1.05 nm, with the tunnel magneto resistance (TMR) ratio of 170%.

Switching current ($57 \mu\text{A}$) for a switching time of 4ns is estimated by numerical solution of the *Landau-Lifshitz-Gilbert-Slonczweski* (LLGS) equation [43] along with stochastic thermal field [46]. A detailed description of the LLGS equation and the resistance transport model used in this work can be found in [108], [109]. The write current of $57 \mu\text{A}$ achieves less than 7.95×10^{-7} write error rate at iso-Switching time of 4ns. The stochastic nature of thermal variations in the nano-magnet is considered by running the LLGS equations over 5000 times, within each run the thermal variation is randomly chosen from normal distributed population with zero mean and temperature dependent standard deviation as illustrated in [109].

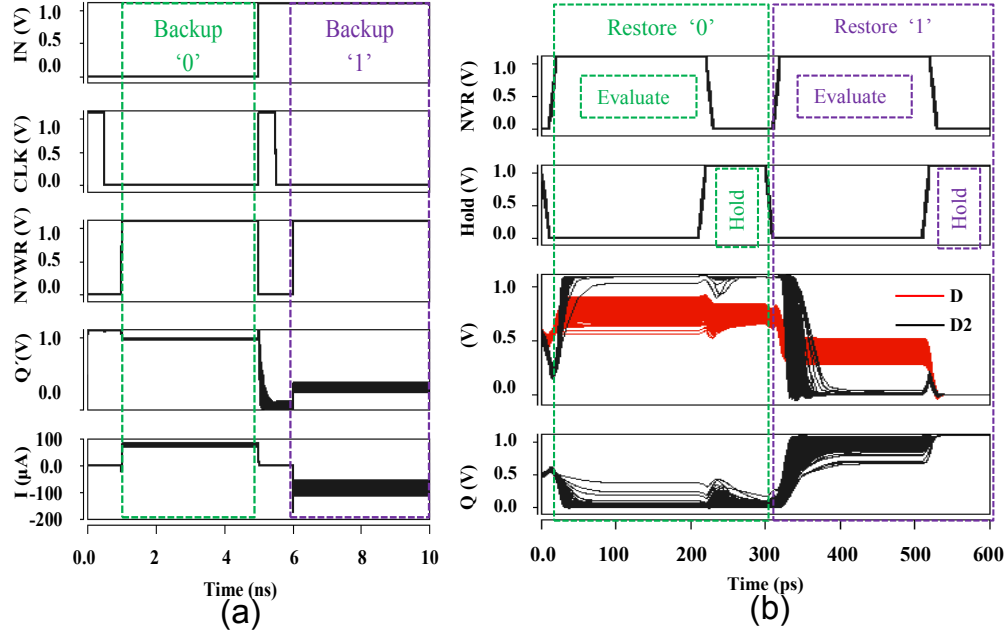


Figure 7.2. (a) The time diagram of the backup operation of '0' and '1'. The diagram is the result of 1000 samples of Monte Carlo simulations. (b) The time diagram of the restore operation of '0' and '1'. The diagram is the result of 1000 samples Hspice Monte Carlo simulations.

7.2 The Proposed SHE-MTJ based NVFF

The proposed circuit is illustrated in Fig. 7.1. The operation of the proposed NVFF can be divided into three different modes – normal operation, backup operation and restore operation. 1) Normal Operation: wherein the NVFF acts as a conventional FF 2) Back-up Operation: wherein the data stored in the FF is saved into the non-volatile SHE-MTJ 3) Restore operation: wherein the data saved in the SHE-MTJ is restored back to the FF for subsequent normal operations.

7.2.1 Normal operation

The NVFF circuit, shown in Fig. 7.1, consists of the usual cascaded master latch which is a positive-clock level triggered latch, and a slave latch which is a negative-clock level triggered latch. The master latch is transparent for input (IN) during positive clock level which turns off M2 and M3, and opens the closed loop consisting of NOT1/NOT2. The slave

latch is transparent for the signal D during the negative clock level which turns off M8, and opens the closed loop consisting of NOT3/NOT4. The overall behavior of the circuit is the well-known negative edge triggered flipflop. During normal operations, the inputs NVR and NVW are low to disconnect the SHE-MTJ and the associated circuitry from the rest of the flipflop.

7.2.2 Backup operation

During the backup operation the data stored as electrical charges in the FF circuit is written into the associated non-volatile SHE-MTJ. The backup operation starts by turning the NVW high while keeping the CLK low for 4ns as illustrated in Fig. 7.2(a). While the CLK signal is low, the loop connecting NOT1/NOT2 is closed. The SHE metal terminal LR is connected to $V_{DD}/2$ during the backup phase. In case of backup of logical '0' ($Q = '1'$ and $Q = '0'$), the SHE metal contact A is connected to V_{DD} by NOT1 PMOS transistor and M4-M5 transmission gate. Thereby, a charge current flows from node 'A' to node 'LR'. Transistors M4-M5 are sized such that it provides the required write current for switching the SHE-MTJ device to anti-parallel (AP) state. Similarly, in case of backup for logical '1' ($Q = '0'$ and $Q = '1'$), the SHE-MTJ metal contact A is connected to ground through the NOT1 NMOS transistor and transmission gate M4-M5. The charge current flow in this case is in opposite direction (from node 'LR' to 'A') resulting in switching of the SHE-MTJ to parallel (P) state. Thus, after the backup operation is completed, the SHE-MTJ ends up in P state for logical '1' ($Q = '0'$ and $Q = '1'$) and in AP state for logical '0' ($Q = '1'$ and $Q = '0'$).

7.2.3 Restore operation

During the restore operation, the data stored as P or AP state within the SHE-MTJ is restored back to the NVFF in form of electrical charges. Once the restore operation is completed the NVFF is ready to be used as a normal flip-flop. The restore operation starts by setting HOLD to low and NVR to high (NVW is low) to provide a path from V_{DD} to ground through the SHE-MTJ - M6 and M7. M7 - M6 and the SHE-MTJ forms a voltage divider.

Thereby, the voltage at the node D is dictated by the voltage divider effect and depends on the resistance state of the MTJ. The circuit is designed such that when the SHE-MTJ is at the low resistance P state, the voltage at node D is less than the switching threshold of the inverter NOT3. Due to the amplification action of the inverter NOT3, the output at the node Q will be almost high while the point D2 will be close to zero, as illustrated in Fig. 7.2(b). When the transistor M8 is turned on towards the end of the restore operation, the node D is dragged to zero by the amplified output of the path NOT3/NOT4 (D2), and the data is held in the slave latch. Note, when the gate of M8 is pulled high, NVR is pulled low to avoid any contention at node D. The same scenario is valid during the restore of logical '0' except that the SHE-MTJ is in high resistance state R_{ap} , the voltage at node D is designed to be higher than the trip point of the inverter NOT3, the output Q is zero, and node D2 is at V_{DD} . The CLK is kept at logical '1' during the restore operation. Thus, the gate of M8 is controlled by HOLD signal only. In contrast, the gate of M8 will be controlled by the CLK only during normal operations. The overhead required for this switching between CLK/Hold at gate of M8 is one extra AND gate that is shared between many flipflops that do the same operation simultaneously. Therefore, this AND gate is not part of the flipflop but it is part of the control circuit. The AND gate has two inputs which are CLK and Hold. The output of the AND gate is connected to the gate of M8.

In summary, the small voltage difference developed at the node D due to the voltage divider effect is amplified by the inverter NOT3 resulting in higher sense margin and robust restore operation. It is also worth mentioning that we do not require additional inverter during the restore operation as a gain element rather we rely on inverter NOT3 which originally is a part of the slave latch.

7.2.4 Results and analysis

We performed Monte Carlo analysis to ascertain the robustness of the proposed NVFF in presence of process variations. The transistor threshold voltage variations were modeled by a normal distribution with standard deviation $\left(\sigma\sqrt{\frac{W_{min}L_{min}}{WL}}\right)$, where W , L , W_{min} , and L_{min} are the width, length, minimum width, and minimum length of the transistor[110], respectively and σ was chosen to be 25mV. In the same manner, the MTJ oxide thickness is varied

Table 7.1. The summary of the simulations results.

	NVFF	DNVFF [99]	Improvement
Restore Energy (fJ)	6	21.4	3.5x
Backup Energy (fJ)	218	638.8	2.9x
Restore Time (ps)	300	300	-
Backup Time (ns)	4	4	-
Area (μm^2)	3.4455	5.796	1.68x

according to a normal distribution with 1.05 nm mean and 1.5% standard deviation [111]. Simulation results for 1000 Monte Carlo runs for backup and restore operations are shown in Fig. 7.2 (a)-(b). The circuit simulations are done using MTJ model developed in [108]. The transistor model used is the predictive technology model (PTM) for high performance 45 nm node [112], [113]. The comparison is done using the same SHE-MTJ device for both cases. The MTJ used has energy barrier higher than 60KT which is more suitable for practical applications [114].

The results are summarized in Table 7.1, where the second column are the results from [99] for differential SHE based flipflop (DNVFF). The results show a factor of 2.9x improvement in backup power, due to the use of a single MTJ in NVFF. Although reducing the number of MTJ by one is expected to give only a factor of 2x improvement, the transistor scaling to provide the higher current and the overlap of backup and restore paths in case of DNVFF results in higher energy consumption. The restore power is improved by a factor of 3.5x in case of NVFF. This energy benefit results from the fact that the proposed NVFF uses only one SHE-MTJ in addition to the fact that the DNVFF requires a precharge step prior to the restore operation which consumes additional energy. Further, in contrast to the DNVFF, the proposed NVFF restore operation only requires two signaling steps – evaluation and hold and does not require a precharge step, thereby simplifying the requirement for external control circuitry.

Although the SHE-MTJ has decoupled read and write paths, the circuit topology of DNVFF can not take advantage of this property as the circuit backup and restore paths are

overlapped *i.e* the circuit associated with the slave latch is responsible for both the backup and the restore operation. In contrast, NVFF uses the master latch for backup and the slave latch for restore that allows independent sizing of the transistors in the master and the slave latch as required for proper functioning of the NVFF. As a consequence, the proposed NVFF has a wider design space and better robustness.

The area is estimated using the layout rules in [115]. It is clear from the above discussion that 1.6x area improvement is expected as a result of using a single SHE-MTJ and lesser number of transistors.

For completeness we compared the proposed NVFF performance to the minimum scaled CMOS flipflop at the same technology node. The average energy dissipation per bit during normal operation is 10 (fJ) for NVFF compared to 4.7 (fJ) for minimum scaled flipflop. The worst case time delay from the CLK falling edge to output ready at Q is 103 (ps) and 71 (ps) for NVFF and minimum scaled flipflop, respectively.

8. FUNCTIONAL READ ENABLING IN-MEMORY COMPUTATIONS IN 1TRANSISTOR - 1RESISTOR MEMORY ARRAYS

In-memory computing is an emerging paradigm that attempts to embed some aspects of logic computations inside memory arrays leading to higher throughput and lesser energy-consumption. Consequently, various in-memory compute proposals using emerging non-volatile technologies based on *functional read* - wherein multiple word-lines are simultaneously activated and a Boolean function of the constituent activated rows is read, is being extensively investigated. In this section, we first show that the conventional sensing scheme for such functional reads, operated on 1 Transistor - 1 Resistor (1T-1R) memory arrays, is limited theoretically by low sense-margin. We demonstrate that the sense-margin *does not* improve even if the ON-OFF resistance difference is increased from low values to considerably higher values [116]. Subsequently, we present a new sensing scheme based on skewed sense-amplifiers and staggered world-line activation as a method for enabling functional read operations. We show that in-memory XOR, IMP (implication) and bit-wise comparison can be easily implemented through the proposed scheme.

The unprecedented scaling of the metal oxide semiconductor field effect transistors (MOS-FETs) have powered the ever increasing compute efficiency and throughput on silicon chips [117]. Specifically, the drastic improvement in compute efficiency in past few decades can be traced back to the availability of larger memory capacity and the speed-up obtained due to shrinking transistor sizes [118]. However, transistor scaling has slowed down significantly as the dimensions of the transistors approach their physical limits [119]. Further, the existence of the well-known ‘memory-bottleneck’ inherent in the state-of-the-art von-Neumann computing model poses a major constrain for energy efficient and high throughput computations.

Researchers are actively investigating a two-pronged solution to keep-up with the compute requirement for future data-intensive tasks. On one hand, beyond CMOS emerging non-volatile resistive technologies are being widely investigated to achieve high-density, low stand-by power memory systems [120], [121]. While on the other, there is a renewed quest for embedding computations close to the memory units enabling ‘in-memory’ processing that

can to some extent mitigate the ‘memory-wall bottleneck’ [122]. With respect to in-memory vector Boolean computations, the general approach is to activate two rows of a memory array, simultaneously. In response to the activated rows, bit-wise Boolean operation of the data stored in the two individual rows is performed by minimal modification to the memory array and peripherals.

Intuitively, one would expect that with improvement in ON-OFF resistance ratios of the constituting memory devices, drastic improvements in read sense-margin for functional read schemes can be achieved. We start by pointing out that within the constrain of using the well-known cross-coupled inverter based sense-amplifiers, the conventional sensing scheme is unsuitable for in-memory operations. Furthermore, the sense-margin *does not* improve with improved ON-OFF ratios. As such, whether the ON-OFF ratio is high or low, the conventional sensing scheme would result in high sensing failure rate with respect to in-memory computing. Toward that end, we propose a novel sensing scheme suitable for in-memory computing with the major advantage that the sensing-robustness steadily improves with improving ON-OFF ratios. Furthermore, we only rely on the well-known cross-coupled inverted based sense-amplifiers that are used in almost all large-scale chips fabricated based on emerging devices [123], [124].

8.1 Proposed Sensing Scheme for Bit-wise In-Memory operations

We start by first describing that the conventional ‘*simultaneous row activation scheme*’ is fundamentally limited by low sense-margin irrespective of the ON-OFF resistance ratio of the constituting resistive memory element.

8.1.1 Simultaneous Row Activation

To understand the conventional sensing involving simultaneous row activation, let us assume we have to compute vector bit-wise Boolean operation corresponding to the bit-stream stored in two arbitrary rows in a memory-array. The simultaneous activation dictates that both the rows storing the data to be computed are activated simultaneously by activating the access transistors through the wordline signals WL1 and WL2 as shown in Fig. 8.1. With WL1 and WL2 activated, the two memory elements X1 and X2 effectively form a parallel

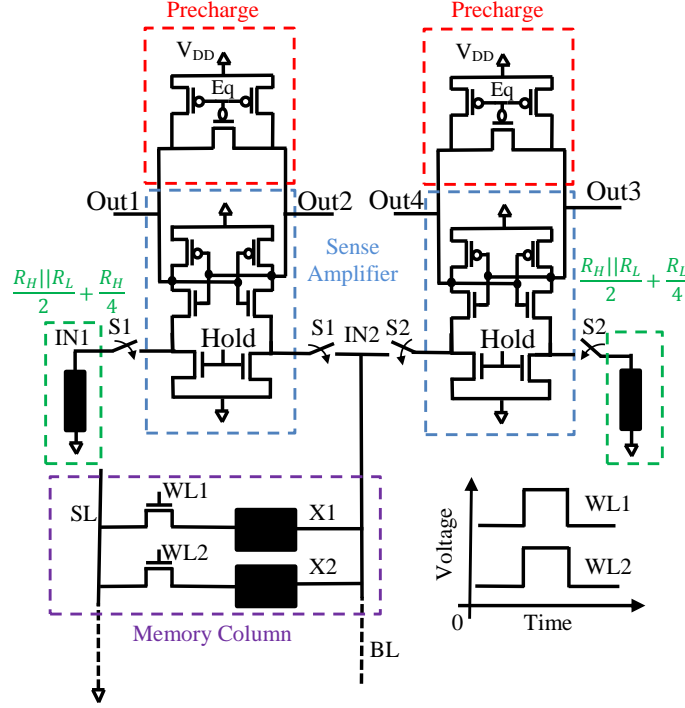


Figure 8.1. The circuit schematic of simultaneous memory activation scheme.

combination (ignoring the presence of the access transistors). This parallel configuration has three possible resistance states - $R_H/2$, $R_L/2$ and $R_H||R_L$ (R_H = High Resistance and R_L = Low Resistance). Assuming R_H represents a digital ‘1’ and R_L a digital ‘0’, if one can sense the presence of $R_H/2$, it would represent an AND gate, since AND (NAND) is ‘1’ only when both the inputs are high. Similarly, if $R_L/2$ is sensed OR (NOR) logic can be accomplished, since OR is zero only when both inputs are zero. The AND (NAND) and OR (NOR) output thus generated can be combined easily to achieve an XOR gate [125].

Thereby, in order to sense $R_H/2$ and $R_L/2$ from among $R_H/2$, $R_L/2$ and $R_H||R_L$ two sense-amplifiers can be used as shown in Fig, 8.1. Each of the sense-amplifiers has one of its input connected to the bit-line (BL) while the other input is connected to a reference resistance. As shown in Fig 8.1, the reference resistance for comparing between $R_H/2$, $R_L/2$ is set to average of $R_H/2$ and $R_L/2$, while the reference resistance for the other sense-amplifier is designed to be the average of $R_L/2$ and $R_H||R_L$. As such, the two sense-amplifiers accomplish two comparisons and ascertain if the parallel combination of the memory elements X1 and X2 is $R_H/2$ or $R_L/2$.

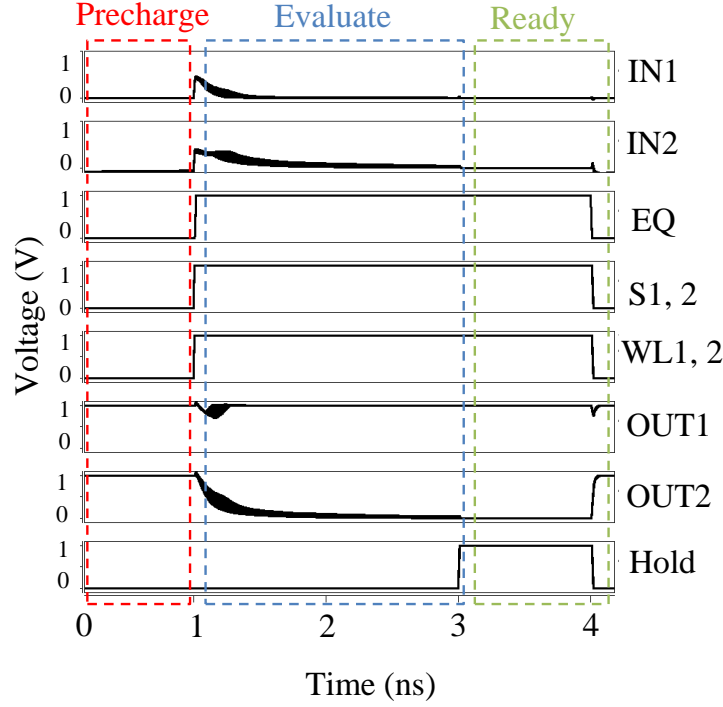


Figure 8.2. The time diagram of simultaneous memory activation schema that is simulated by Hspice Monte Carlo for 1000 samples.

The time sequence of the simultaneous row activation consists of three stages. First, the sense amplifier outputs are precharged to the same voltage level. Second, the memory word-lines WL1 and WL2 are enabled while the precharge circuit has been disconnected. Finally, the memory word-lines WL1 and WL2 are disabled and the Hold signal is enabled to latch the sense amplifier outputs. The time diagram of the the simultaneous row activation is illustrated in Fig. 8.2.

It is important to note that, as a function of the improved ON-OFF ratio between the resistances of the memory elements the sensing robustness for one of the sense-amplifiers in Fig. 8.1 would steadily improve, while the sensing-margin for the other sense-amplifier stays relatively constant irrespective of improvement in the ON-OFF ratio. Specifically, for the sense amplifier differentiating between $R_H/2$ and $R_H||R_L$, the sense-margin improves due to improvement in the resistance value R_H . In sharp contrast, the sense-margin for the sense-amplifier sensing between the resistance levels $R_L/2$ and $R_H||R_L$ remains almost constant and independent of the increased R_H/R_L ratio. This is because the resistance value

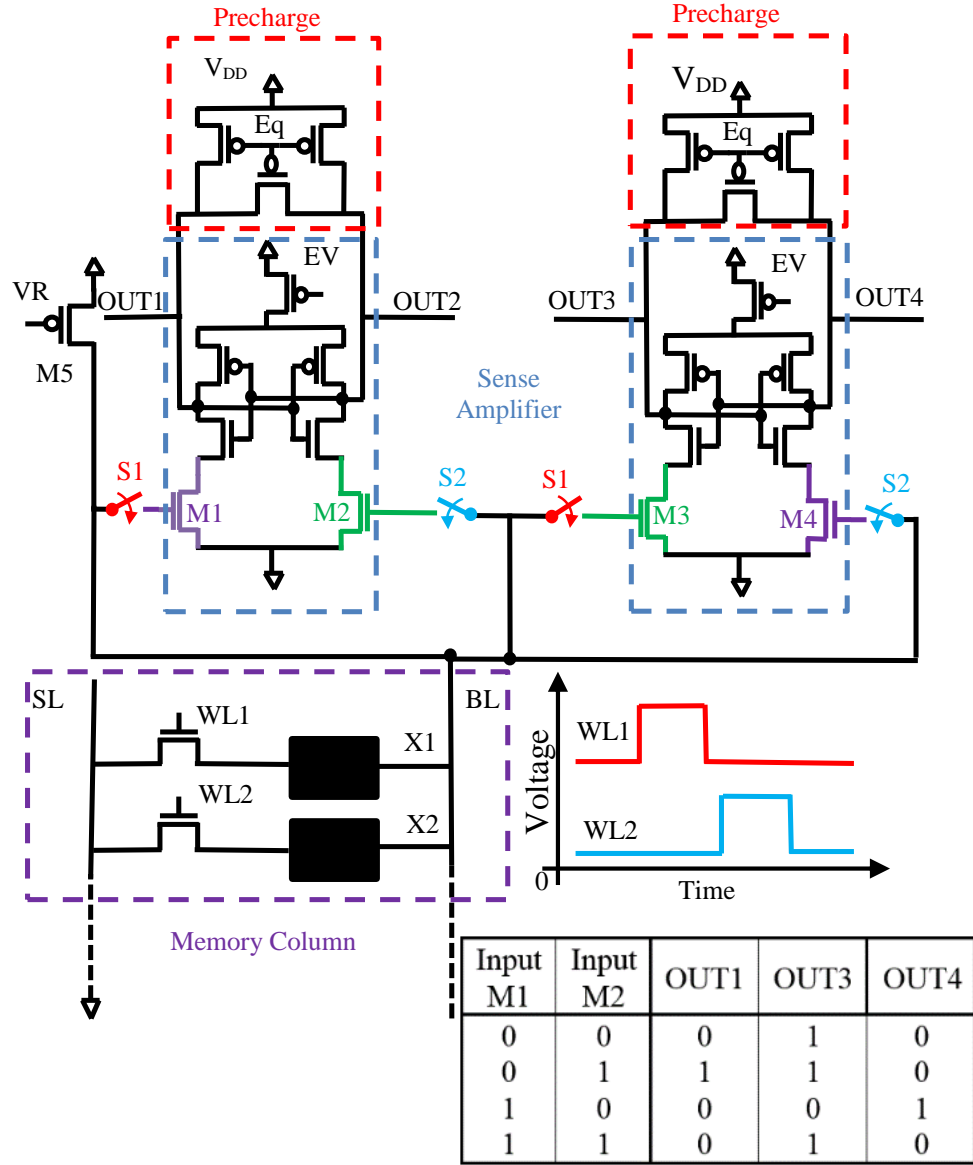


Figure 8.3. The circuit schematic of staggered memory activation schema.

$R_H||R_L$ is theoretically bounded by R_L , therefore, irrespective of the improved value of R_H the resistance difference that the sense-amplifier has to sense remains constant. In summary, the conventional scheme wherein both the WLs are simultaneously activated is limited by the poor sense-margin of one of the sense-amplifiers that is independent of the R_H/R_L ratio of the memory element.

8.1.2 Proposed Staggered Memory Cell Activation

The proposed staggered memory activation scheme dictates that the WL1 should be activated first for $1ns$ with the switch S1 closed and S2 open and VR is pulled low allowing a voltage-divider to be formed between transistor M5 and the bit-cell. Thereby, the resultant voltage on BL representing the memory bit-cell X1 is stored on the parasitic capacitances at the gate of transistor M1 and M3. Subsequently, WL1 is deactivated and WL2 is activated while switch S2 is closed and S1 is kept open. During this time, the voltage on the BL corresponding to the memory bit-cell X2 is stored on gates of transistors M2 and M4. Thereafter, both S1 and S2 are opened and the sense-amplifiers are ready to be activated.

Note, at this stage the two sense-amplifiers have voltages at each of their input terminals proportional to the data stored in the memory elements X1 and X2, respectively. Four combinations are possible for X1 and X2 – (0,0), (0,1), (1,0), (1,1). For the case of (0,1) or (1,0) the voltages developed on the two inputs of the sense-amplifiers will be different. As such, the sense-amplifiers sense the difference in voltages and results in $OUT1 = 1$ and $OUT3 = 1$ for the case (0,1) and (1,0), respectively, as shown in the table in Fig. 8.3. However, for the case (0,0) and (1,1) the voltages on the two sides of the sense-amplifiers would be same since the data in X1 and X2 are the same. This can lead to an ‘unpredictable state’ for the sense-amplifier output. We circumvent this issue by asymmetrically sizing the sense-amplifiers such that M1 is sized greater than M2 and M4 is sized larger than M3. Because of such asymmetric sizing, for the cases (0,0) and (1,1) *i.e.* when the voltages on both the inputs of the sense-amplifiers are the same, the sense-amplifiers will end up switching according to the *in-built* skew of the constituting transistors. Accordingly, for both the cases (0,0) and (1,1) $OUT1 = 0$ and $OUT3 = 1$, respectively, as mentioned in the table in Fig. 8.3.

The table of Fig. 8.3 implies that, if we OR $OUT1$ with the NOT of $OUT3$, XOR logic can be easily accomplished. Additionally, the logic levels corresponding to $OUT3$ represents the truth table for IMP (implication logic). Not only XOR is an important functionality for various bit-wise operations, it can also be used for ‘in-memory’ ADD operations by including additional peripheral circuits. Furthermore, XOR and IMP form a universal basis set, hence,

in general, any bit-wise Boolean functionality can be achieved through repeated use of XOR and IMP operations. Another, key aspect of the presented proposal as opposed to previous works is the fact that we can achieve bit-wise Boolean in-memory comparison operation. To understand how this can be achieved, let us observe the truth table of 8.3. OUT1 is ‘1’ only when the input data is (0,1) while OUT4 is ‘1’ only for the input data (1,0). Thereby, OUT1 represent $X1 < X2$ and OUT4 represents $X1 > X2$, while if OUT1 and OUT4 are both ‘0’ it indicates $X1 = X2$. Thus, the proposed sensing scheme allows for in-memory XOR, IMP as well as bit-wise comparison.

It is important to note that the skewing of the sense-amplifier although helps to avoid the ‘unpredictable state’ for the cases (0,0) and (1,1) it slightly degrades the sense-margin for the cases (1,0) and (0,1). However, as shown in the next section despite the slight degradation of the sense-margin the proposed scheme performs better than the conventional simultaneous activation and the sense-margin notably improves with improvement in R_H/R_L ratio.

Notably, the most remarkable aspect of the proposed staggered activation is that the sensing-robustness steadily improves with improvement in the R_H/R_L ratio. Intuitively, this is because of the fact that for the staggered activation scheme the sense-amplifiers either compares same voltages and fall to their ‘default skewed’ state or they compare R_H with R_L the difference of which increases significantly with increase in R_H/R_L ratio. Recall, in contrast the simultaneous activation is constrained by sensing between $R_L/2$ and $R_H||R_L$ the ratio of which remains constant irrespective of the R_H/R_L ratio.

8.2 Simulation Results and Discussions

In order to ascertain the resilience of the proposed sensing scheme against process variations, a Monte Carlo circuit simulation is conducted considering normally distributed resistance of the storage element within 5% standard deviation (STD).

The transistor threshold voltage variations are modeled by a normal distribution with standard deviation $\left(\sigma\sqrt{\frac{W_{min}L_{min}}{WL}}\right)$, where W, L, W_{min} , and L_{min} are the width, length, minimum width, and minimum length of the transistor, respectively and σ was chosen to be 30mV [86], [110], [111]. A supply voltage V_{DD} of 1V is used for all simulations in this study.

A total of 10,000 Monte Carlo samples is used for estimating all the results in this study using the predictive technology model (PTM) for 45 nm node [112], [113].

For a fair comparison, we used similar sizing for all the transistors which is $2w_{min}$ for PMOS and w_{min} for NMOS, where w_{min} is the minimum transistor sizing. This sizing is used for both the simultaneous and staggered sense amplifier except for M1, M2, M3, and M4. The sizing for M1, M2, M3, and M4 are $1.2w_{min}$, $5w_{min}$, $1.2w_{min}$, and $5w_{min}$, respectively. Additionally, the supply voltage is 1V. All switches are transmission gates consisting of NMOS and PMOS transistors. The read error rate is inverse proportional to the time period of the read operation, we strict all the simulation to iso-switching time of 4ns.

The timing diagram of the staggered memory activation is illustrated in Fig. 8.4 and 8.5 for the inputs ‘01’ (or ‘10’) and ‘00’ (or ‘11’), respectively. The proposed staggered read scheme illustrated in Fig. 8.3 starts by connecting the two sense amplifier terminals to the same BL through two different transmission gates that are enabled in staggered order. First, while WL1, WL2 and VR are ‘1’, ‘0’ and ‘0’, respectively, the BL is charged by the transistor M5 and the developed voltage at (BL) is stored in the gate capacitance of M1. Second, while WL1, WL2 and VR are ‘0’, ‘1’ and ‘0’, respectively, the BL is charged by the transistor M5 and the developed voltage at (BL) is stored in the gate capacitance of M2. Intuitively, the stored charges in M1 and M2 gate capacitance are proportional to the resistance of the first and second memory cell, respectively and hence, to the logical value stored in the cell. Finally, the charging circuit is disabled to start the evaluation phase to develop the final values of OUT1 through OUT4 which is the result of the comparison of the voltage developed by the two memory cells at BL. The values of OUT1 and OUT2 are retained by the latch that consists of the two cross-coupled NOT gates. It is worth noticing from the timing waveforms of Fig. 8.5, OUT1 falls to zero due to in-built skew of the sense-amplifier. On the other hand the output of Fig. 4 is decided based on the difference in the voltage levels at the gate of transistors M1 through M4. Note, although not shown, OUT3 and OUT4 would produce similar timing behavior except that the sense-amplifiers are skewed in opposite direction.

The comparison of number of failing cases of the staggered and simultaneous memory cell activation is illustrated in Fig. 8.6. The results are presented for different R_H/R_L ratio

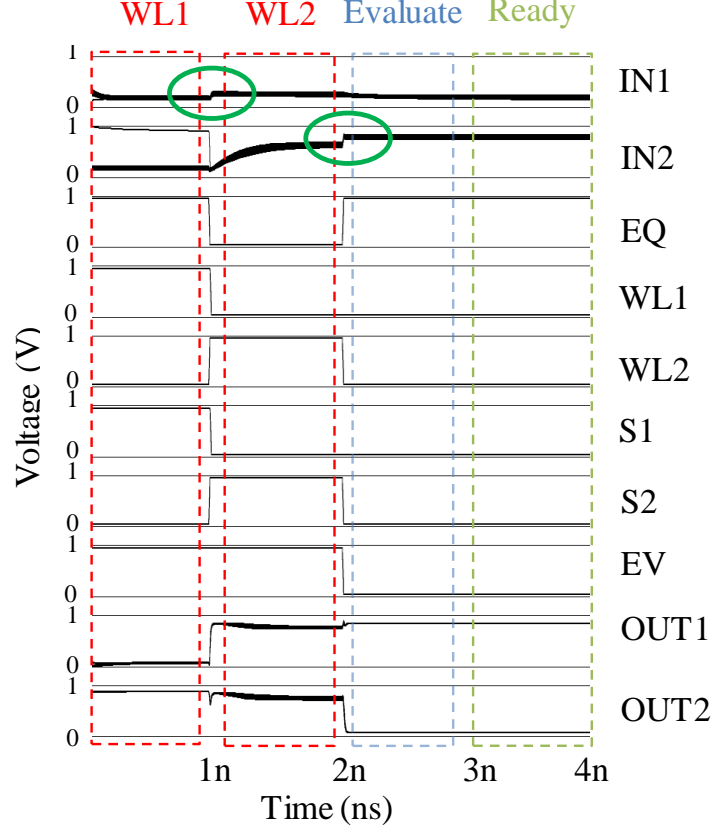


Figure 8.4. The time diagram of staggered memory activation schema for '01' simulated by Hspice Monte Carlo for 1000 samples. The charge sharing and charge injection happen due to switching off the transmission gates are marked by the green oval.

ratios. Few key observations from Fig. 8.6 are as follows: 1) For all cases the overall error for staggered activation is better than the conventional simultaneous activation. 2) The overall error for simultaneous activation remains relatively constant across all R_H/R_L ratio values. This is because although OUT1 (i.e. sensing between $R_H/2$ and $R_H||R_L$) improves due to increasing R_H , OUT3 (i.e. sensing between $R_H||R_L$ and $R_L/2$) remains almost constant. 3) In contrast, the number of failing case decreases steadily with the increase in R_H/R_L ratio for the proposed staggered sensing scheme. Of particular interest is the fact that by enabling staggered activations of the word-lines the presented proposal can be used in conjunction with well-known cross-coupled inverter based sense-amplifiers to accomplish in-memory XOR, IMP, bit-wise comparison and also more complex operations like ADD as

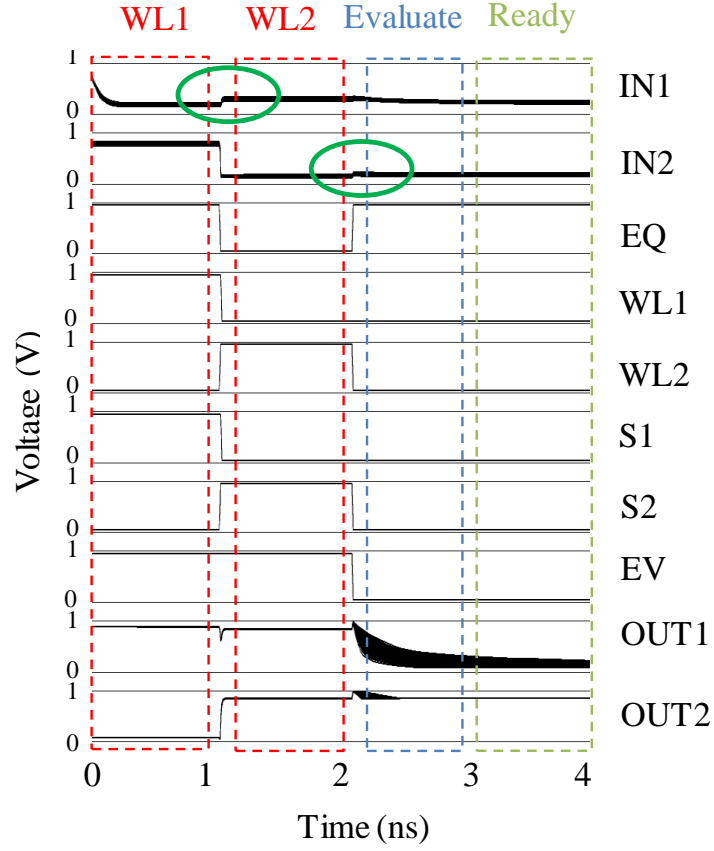


Figure 8.5. The time diagram of staggered memory activation schema for '00' simulated by Hspice Monte Carlo for 1000 samples. The charge sharing and charge injection happen due to switching off the transmission gates are marked by the green oval.

shown in [126]. For comparison the power consumption for both the simultaneous and staggered are $26.74 \mu W$ and $14.56 \mu W$, respectively. The energy of the simultaneous and staggered activation is 106.9 fJ and 58.24 fJ , respectively. The area of the staggered sense circuit is $44 \mu m^2$. The area of simultaneous activation sense circuit is $22 \mu m^2$. To quantify the temperature variations effect we repeated the same simulation at 50° . The simulation results shows almost the same performance for both architectures, as illustrated in Fig. 8.7. The performance of the staggered activation is still dominating the simultaneous activation at 10% lower supply voltage, as illustrated in Fig. 8.8. The distribution of the threshold

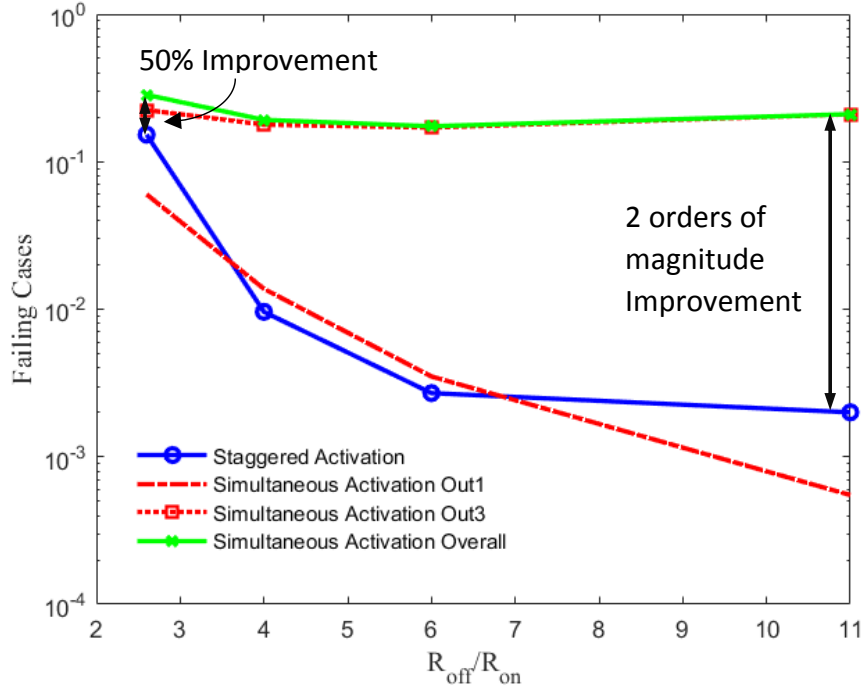


Figure 8.6. The number of failing cases for staggered and simultaneous memory activation schemes as a function of different ON-OFF resistance ratios 25°C .

voltage and sense amplifier inputs for the staggered memory activation are illustrated in Fig. 8.9 and Fig. 8.10 for on-off ratio of 10.

The voltage stability is determined by two factors the value of gate capacitance and the leakage current. Based on simulations, the time constant of the gate was found to be $16\mu\text{s}$ according to spice simulations. This means that the time needed for 1% change in gate voltage by leakage current is 100ns. The entire read operation requires 4ns which is 25x less than the gate retention time. Additionally, such sensing schemes wherein a voltage is stored as a charge on gate capacitance during sensing has been explored in various fabricated chips in prior literature (although not in the context of in-memory computing). One such work is [94] where charges were stored on the gate capacitance of the sense amplifier one by one to enable robust sensing for VCMA based MRAM cells. Finally, we would like to mention that the proposed staggered functional read scheme is valid, in general, for any class of 1T-1R arrays. We evaluated the staggered activation using the filament-based resistive

RAM variations from [127]. The device in [127] has large variations and a high on-off ratio of 600. The error rate reaches zero for such a high on-off ratio.

The AND, OR, NAND, and NOR can be supported with slight modifications. In table in Fig 8.3, if the input to M2 and M4 is negated then OUT4 is an AND, OUT3 is a NAND, OUT1 is a NOR, and OUT2 is an OR function. The negation of the memory voltage level could be achieved by the circuit in [111]. The delay of the negation circuit (NOT gate) is neglected compared to the memory access time. For all these functions, the memory cell access is done once. Additionally, IMP and XOR form a complete basis set hence any Boolean function can be achieved by repeated use of IMP and XOR functionality. If the input of the second memory cell is replaced by a reference cell that contains a known value then the proposed scheme becomes similar to a conventional read based sensing scheme. Furthermore, as long as the ON-OFF ratio is high the in-built skew of the sense-amplifier would not lead to any read failure concerns since the input voltage to the sense-amplifiers will be large enough to over-ride the in-built skew.

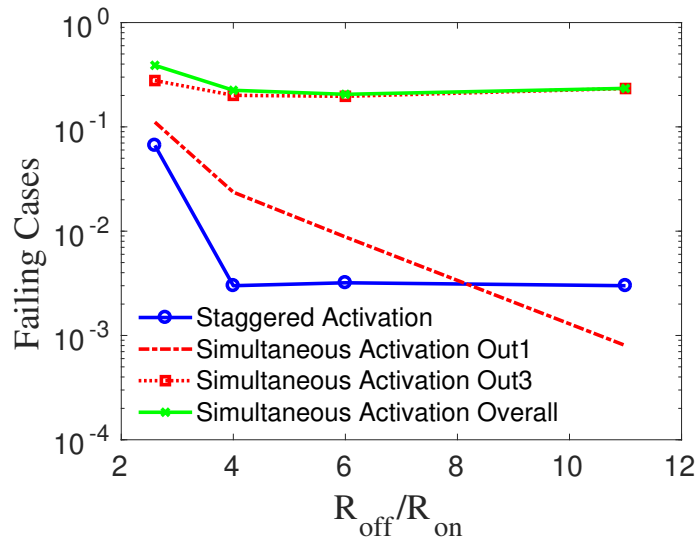


Figure 8.7. The number of failing cases for staggered and simultaneous memory activation schemes at 50°C .

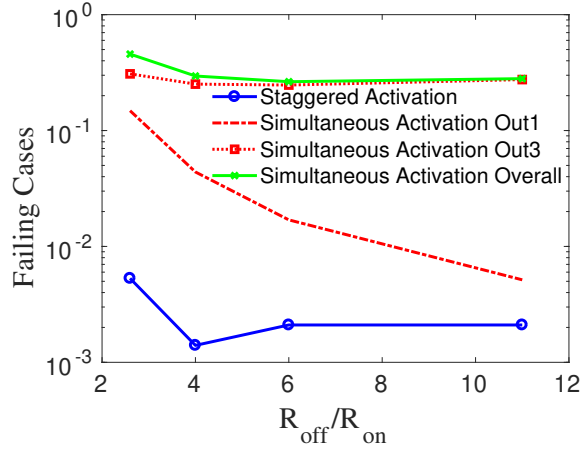


Figure 8.8. The number of failing cases for staggered and simultaneous memory activation schemes at 10% lower supply voltage.

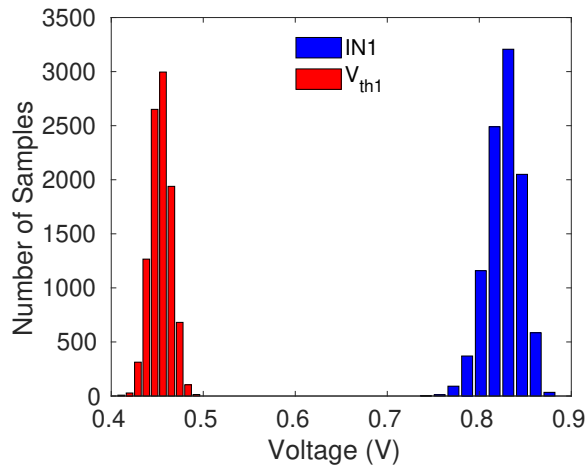


Figure 8.9. The distribution of the threshold voltage variations and the voltage input of the transistor M1.

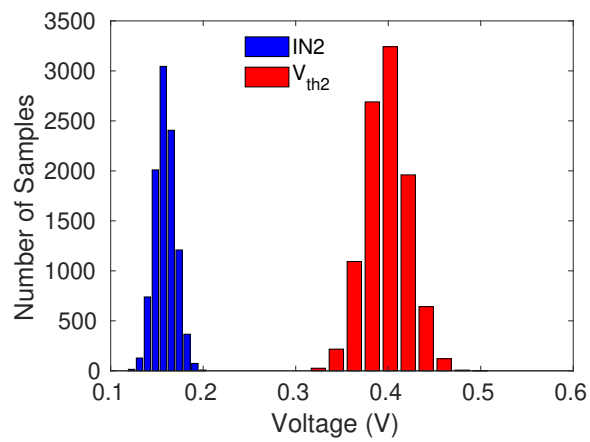


Figure 8.10. The distribution of the threshold voltage variations and the voltage input of the transistor M2.

9. DESIGN AND COMPARATIVE ANALYSIS OF SPINTRONIC MEMORIES BASED ON CURRENT AND VOLTAGE DRIVEN SWITCHING

Spin transfer torque (STT) based switching of magnetic random access memories (MRAMs) have stimulated considerable research interest in recent years. The non-volatility of STT-MRAMs, high areal density and low static power dissipation makes them a strong contender for possible replacement of conventional silicon based memories. However, a major bottleneck associated with STT-MRAMs is their high write current requirement. Recently, it has been demonstrated that the high write current of the STT switching mechanism can be improved by using other magnetic switching techniques like voltage controlled magnetic anisotropy (VCMA), spin Hall effect (SHE), and magneto-electric effect (ME). Interestingly, each of these new physics increases the design space to be explored and presents interesting trade-offs with respect to read and write mechanisms. It is, therefore, important to analyze these devices with respect to their readability, writability and areal density in a unified framework that is based on the state-of-the-art experimental results.

Recently, the scaling of SRAM on-chip memory for high-speed low power computing is facing many challenges. The major obstacles are low areal density, high static power dissipation and reduced bit-cell stability due to transistor scaling [2]–[4]. Spin transfer torque magnetic random access memory (STT-MRAM) is a promising candidate for future on-chip cache memory due to its non-volatility, low static power dissipation, and dense bit-cell integration [2], [4], [109]. Although many STT-MRAM proof-of-concept memory arrays have been demonstrated in recent years [128], yet STT-MRAMs are plagued with certain issues that have to be addressed before they become the next workhorse of on-chip cache memories.

The two major issues concerning STT-MRAM are the high write current (in the order of few hundreds of micro Amperes), and the low sense margin due to limited device tunnel-magneto-resistance (TMR)[129]. The high write current not only leads to energy inefficient write operations, it also severely constrains the scalability of the driving transistors. In addition, the limited TMR along with the shared read/write paths of the conventional STT-MRAM memory bit-cell leads to severely constrained design space. As such, more ef-

efficient write techniques based on voltage controlled magnetic switching (VCMA), spin Hall effect (SHE) , and magneto-electric coupling (ME) are being investigated in the literature to improve the write performance of the memory cells.

Owing to the high spin injection efficiency coupled with the low resistance write path, SHE based bit-cells are expected, in general, to outperform the standard STT-MRAM with respect to write energy requirement [95], [130]. VCMA is a single-phase coupling between the electric field and the interfacial anisotropy, which improves the switching efficiency and allows precessional switching at a higher voltages leading to fast and energy efficient switching mechanism [131]. In addition, the magneto-electric coupling is a two-phase coupling between the electric field and the magnetization that could switch the magnetization by use of electric field instead of spin-polarized currents [132]. The main advantage of ME based switching is that it has zero steady state current leading to ultra-low energy switching mechanism. Moreover, SHE and ME based devices are three-terminal devices that allow one to have de-coupled read/write paths and hence have better readability and writability. However, the three-terminal nature of these devices inevitably leads to larger bit-cell area due to requirement of multiple transistors and associated contacts.

Given the various aforementioned embodiments of spin devices (STT, SHE, VCMA, ME) with potentials of replacing the current silicon based cache memories, it is imperative to put these devices in proper perspective through a detailed comparative power-performance-area analysis. Prior work on analyzing various aspects of spin devices can be found in the literature. Chun *et. al.* [4], have presented scaling trends for in-plane and perpendicular anisotropy based STT-MRAM bit-cells. However, the work in [4] use analytical approximations as opposed to rigorous numerical simulations of magnetization dynamics and resistance model. Another work that compares in-plane versus perpendicular STT-MRAM can be found in [133], which uses numerical computations for solving magnetization dynamics. Further, the work in [109], discusses scaling trends not only for STT-MRAMs but also with respect to the SHE based bit-cells. In addition, independent works discussing design aspects of specific devices like the VCMA bit-cell, the ME-MRAM and the SHE based bit-cells can be found in [134], [135] and [136], respectively. A recent work that compares in detail VCMA bit-cells with STT-MRAMs has been reported in [137].

Despite such works, a comprehensive analysis that discusses all the different genres of spin devices in a comparative manner in a single work under common design constraints has been missing in the literature. Towards that end, in this section we analyze bit-cells based on the aforementioned spin devices using a coupled magnetization dynamics and electron transport model in a comparative manner [138]. Our analysis is based on various design metrics like the write current requirement, layout area, device tunnel-magneto-resistance (TMR), cell-TMR (CTMR), read disturb margin (RDM), read sensing margin (RSM) *etc.* Each of these design metrics are defined in respective sections of the manuscript.

Let us begin by understanding the basic magnetic device called the magnetic tunnel junction (MTJ) which is a magnetic-heterostructure consisting of a non-magnetic insulating oxide sandwiched between two ferro-magnets. A ferromagnetic material is a material that maintains net magnetization in absence of external field. Due to the material property and the asymmetry in the nanomagnet dimensions, there is a certain axis along which the magnetization alignment is preferred (*easy axis*). Along the *easy axis*, the total energy is in the minimum state, as shown in Fig. 9.1. The direction of the easy axis depends on material, the interface, as well as the dimensions [139]. The energy needed to switch the magnetization along the easy axis by an angle of 180° is called the energy barrier (E_B). Based on the direction of the easy axis, we can define two categories of magnetic layers: *in-plane magnetic anisotropy* (IMA), and *perpendicular to the plane magnetic anisotropy* (PMA)[107].

As explained earlier, the MTJ consists of two layers of ferromagnetic material separated by an oxide layer. The first layer is a nanomagnet that holds the information stored in the memory (*free layer*). The other magnetic layer is a permanent ferromagnetic layer that works as a current polarizer (*pinned layer*), as illustrated in Fig. 9.1. The resistance of the MTJ is a function of the angle between the magnetization directions of the pinned layer and the free layer [26], [28]. The high resistance antiparallel state (AP) represents logic ‘1’, and the low resistance parallel state (P) represents logic ‘0’.

The difference in resistance of the parallel state (R_p), and the antiparallel state (R_{ap}) could be understood in the light of the band diagram shown in Fig. 9.2. The spin orbit coupling in the magnetic layer is modeled by a shift in the energy bands of the majority spin

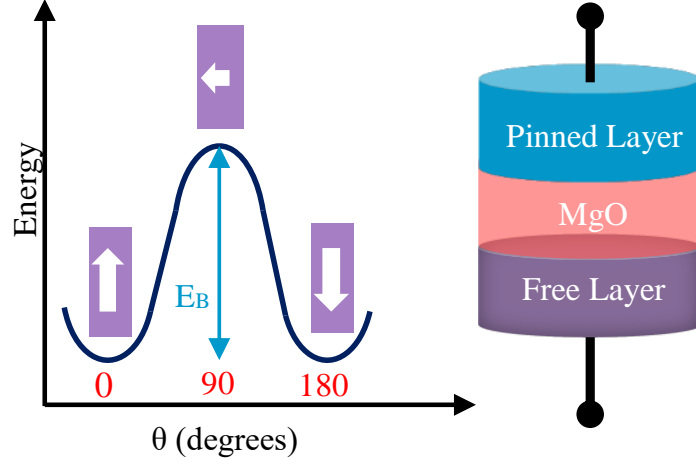


Figure 9.1. The energy as function of the angle θ between the pinned layer and free layer magnetization.

and *minority spin* carriers [26]–[28]. In the case of the antiparallel alignment, if the oxide thickness is much less than the spin flip length, which is a valid assumption, the *majority spin* current tunnels from the permanent magnet to the minority states in the free layer. Simultaneously, the minority spin current in the permanent magnet (shown in red) tunnels to the majority states in the free layer. The overall current is, thus, limited by the minority spin density of states (DOS), thereby resulting in low current or high resistance. In the case of parallel alignment, the majority spin current tunnels to the majority spin states of the magnetic layer on the other side of the oxide. In contrast to the antiparallel case, this current will be limited by the majority spin DOS leading to relatively high current or low resistance.

The widely used 1T-1MTJ bit-cell, which consists of 1 transistor and 1 MTJ, is shown in Fig. 3. The writing of **logical 0 (switching from AP to P state)** is accomplished by applying a positive voltage (V_{DD}) to the bit-line, while the source-line is grounded. The current flows from the (V_{DD}) to the ground and the electrons flow from the pinned layer to the free layer in the opposite direction. The electron current is polarized according to the pinned layer magnetization direction [140]. The spin current scatters at the free layer interface and the spin torque is transferred from the pinned layer to the free layer. The torque, which is exerted on the free layer, switches its magnetization direction so as to be aligned with the

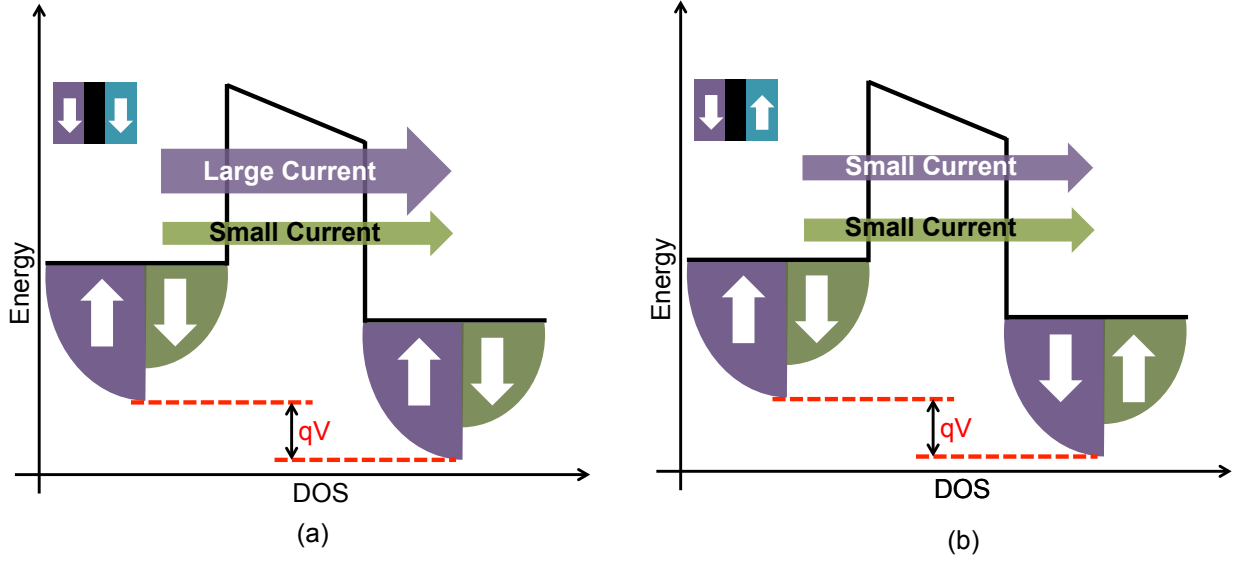


Figure 9.2. The density of states of MTJ in the case of the parallel alignment of magnetization and antiparallel alignment of magnetization.

pinned layer which is ***P state***. In contrast, the writing of ***logic 1 (switching from P to AP state)*** is performed by reversing the voltage polarity of the bit-line and source-line. The electron majority spin current flows from the free layer to pinned layer. The majority spin current passes through the pinned layer and minority spin current accumulates on the oxide interface. The excess minority spin carriers that are accumulated on the interface, exert a torque on the free layer, and switch it to the ***AP state***.

The switching of MTJ state is asymmetric due to two factors: first, the difference in polarization efficiency of the magnetic layers, second, the source degeneration effect of the driving transistor. The current needed in switching from P to AP is higher because the polarization efficiency of the pinned layer is stronger than the free layer. On the other hand, the source degeneration effect can be understood as follows. In the case of writing ‘0’, the gate voltage of the transistor V_G is equal to V_{DD} and the source voltage is grounded, as shown in Fig. 9.3. In contrast, the source voltage is greater than zero in the case of writing ‘1’, and hence ($V_{GS} < V_{DD}$) which leads to source degeneration and reduces the ON current of the transistor [141].

Before we proceed, let us define some useful metrics that would help us to compare the various spin devices considered in this work. The tunneling magneto resistance ratio

(TMR) is $TMR = (R_{ap} - R_p)/R_p$ [26], [28]. The TMR will be used later in this section to evaluate the read performance of the MTJ. Furthermore, another more realistic estimate of the bit-cell read performance is the cell tunneling magneto resistance ratio (CTMR) which is defined as $CTMR = (R_{cell,p}/R_{cell,ap} - 1)$, where $R_{cell,p}$ and $R_{cell,ap}$ are the AP state and the P state cell resistances, respectively. In contrast to the TMR, the CTMR includes the transistor conductance in the calculations of the cell resistance. The TMR and the CTMR are inversely proportional to the read decision failure. In addition, the *read disturb failure* rate is also inversely proportional to *read disturb margin* (RDM) which is defined as $RDM = (I_c/I_p - 1)$, where I_c is the critical write current [142], and I_p is the read current flowing in the low resistance parallel state of the MTJ. The read sensing margin (RSM) is the worst-case difference in the current or voltage at the input of the sense-amplifier corresponding to the P and the AP state. These four metrics *viz.* the TMR, the CTMR, the RDM and the read sensing margin (RSM) would be used to study the readability of various memory bit-cells based on different spin devices.

In the next section, a detailed explanation is given about the numerical and circuit models that are used in the study. Then the physics of each of the devices and the structures of bit-cells is explained along with the write current requirement and cell-layout area, followed by the design and performance of the sense amplifier circuit. In the last section, the results of the simulations with respect to readability and writability will be discussed in a comparative manner.

9.1 Coupled model for magnetization dynamics and electron transport

Over the last century, magnetic fields have been used to manipulate the magnetization direction of the ferromagnetic material. Slonczewski [140], [143] demonstrated theoretically that a spin current polarized by a permanent magnetic layer could transfer torque to a thin layer of ferro-magnet and can switch its magnetization direction. The physics of the magnetization dynamics in response to an external magnetic field or a spin current can be described by stochastic-Landau-Lifshitz-Gilbert-Slonczewski (s-LLGS) equation [43], [44]. The s-LLGS equation is written below in (9.1), where t is time, m is a unit vector in direction of magnetization, H_{eff} is the effective magnetic field, α is the Gilbert damping constant, and

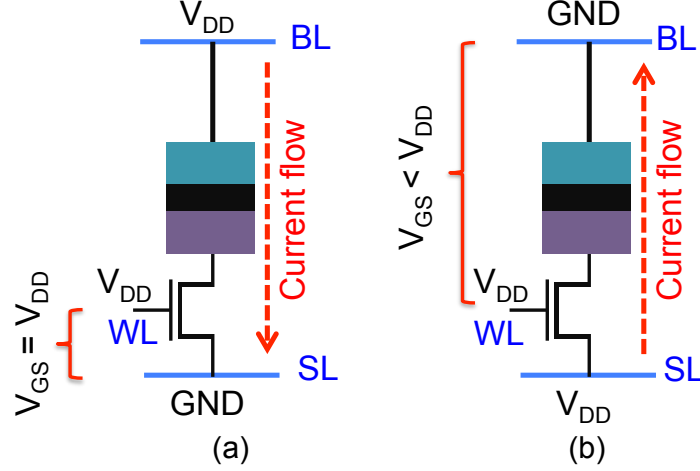


Figure 9.3. The schematic of 1T-1MTJ bit-cell at writing logic ‘0’ and writing logic ‘1’. The source degeneration problem happens in the case of write ‘1’ (switching to antiparallel state).

γ is the gyromagnetic ratio. The s-LLGS equation (9.1) contains three terms: the left term describes the precessional motion of the magnetization due to the effective magnetic field. The second term models the damping of the magnetization vector towards the direction of the effective magnetic field. The third term represents the torque due to the spin transfer phenomenon.

$$\frac{\partial m}{\partial \tau} = -m \times H_{eff} - \alpha m \times m \times H_{eff} + \frac{1}{\gamma} (\alpha m \times STT + STT) \quad (9.1)$$

$$\tau = \frac{|\gamma|}{(1 + \alpha^2)} dt \quad (9.2)$$

The H_{eff} consists of a linear summation of the demagnetization field (H_{demag}), the thermal field (H_{therm}), and the anisotropy field (H_{anis}) (9.3). The anisotropy field is defined in (9.4), [144], where K_i is the interfacial anisotropy, t_{fl} is the free layer thickness, and μ_0 is the free space permittivity. The demagnetization term is defined by (9.5) [145], where N_{xx} , N_{yy} , and N_{zz} are the normalized demagnetization components in x, y and z directions, respectively. The variables m_x , m_y , and m_z are the normalized components of the magnetization. The random variation in the magnetization due to thermal excitations is modeled by effective magnetic field H_{therm} (9.6) [46], where K is Boltzmann’s constant, T is the temperature, V is

the free layer volume, dt is the numerical time step, and ζ is a vector with random components which are selected from standard normal distribution. The thermal term represents the effect of the thermal excitations [46]. This stochastic process is the main source of randomness in the switching probability of nanomagnets.

$$H_{eff} = H_{anis} + H_{demag} + H_{therm} \quad (9.3)$$

$$H_{anis} = \frac{2K_i}{\mu_0 M_{stfl}} \hat{z} \quad (9.4)$$

$$H_{demag} = -M_s (N_{xx} m_x \hat{x}, N_{yy} m_y \hat{y}, N_{zz} m_z \hat{z}) \quad (9.5)$$

$$H_{therm} = \zeta \sqrt{\frac{2\alpha KT}{|\gamma| M_s V dt}} \quad (9.6)$$

The STT term is defined by (9.7) [146], where P is normalized pinned layer magnetization vector, J is electronic charge current, and P_{PL} , Λ_{PL} , P_{FL} and Λ_{FL} are fitting parameters [109].

$$STT = |\gamma| \beta (m \times (\epsilon m \times P + \dot{\epsilon} P)) \quad (9.7)$$

$$\beta = \frac{\hbar J}{2e\mu_0 M_{stfl}} \quad (9.8)$$

$$\epsilon = \frac{q_+}{A_+ + A_-(m \cdot P)} + \frac{q_-}{A_+ - A_-(m \cdot P)} \quad (9.9)$$

$$q_{\pm} = P_{PL} \Lambda_{PL}^2 \sqrt{\frac{\Lambda_{FL}^2 + 1}{\Lambda_{PL}^2 + 1}} \pm P_{FL} \Lambda_{FL}^2 \sqrt{\frac{\Lambda_{PL}^2 - 1}{\Lambda_{FL}^2 - 1}} \quad (9.10)$$

$$A_{\pm} = \sqrt{(\Lambda_{FL}^2 \pm 1)(\Lambda_{PL}^2 \pm 1)} \quad (9.11)$$

The atomistic effective mass non-equilibrium Greens function (NEGF) method is usually used to solve the electron transport in semiconductor and ferromagnetic materials. The high computational effort of NEGF makes it inappropriate for circuit level simulations. For circuit level simulation, we used a compact model fitted using data generated by NEGF simulations. The model is integrated with SPICE circuit simulator. The details of the NEGF model used in this work can be found in [53], [108].

Further, for circuit analysis we used the FinFET model based on the Predictive Technology Modeling for Multi-gate devices (PTM-MG) [112]. The PTM model mainly captures the FinFET parameters from different vendors to fit the Berkeley Short-channel IGFET Model

- Common Multi Gate (BSIM-CMG) standard FinFET compact model [113]. The BSIM-CMG is based on a closed form approximated solution of Poisson equation that is used to calculate the charge density. A transport model based on Gradual Channel Approximation (GCA) is used to calculate the drain current. The quantum effects are added to the model as correction terms. The model is verified against numerical models and experimental data and used as a standard for the industry. Thus, the magnetization dynamics, the resistance model and the PTM FinFET model provides us a device-to-circuit level simulation framework for analysis of various bit-cells considered in this work.

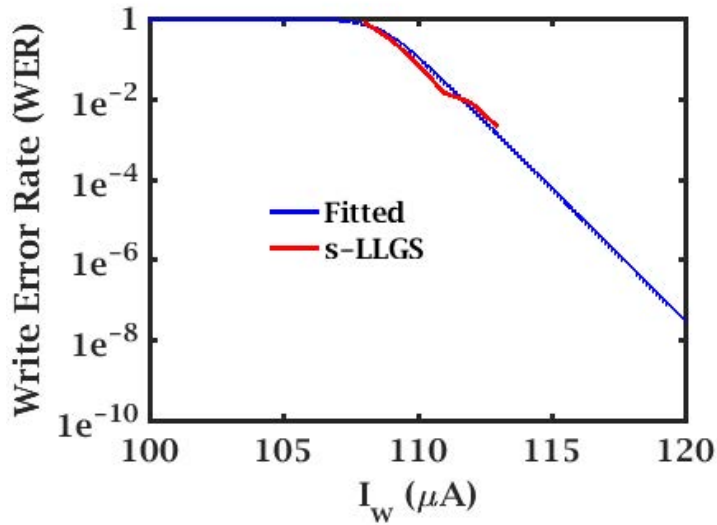


Figure 9.4. The semi-log plot of the WER of PMA based memory cell at iso-Switching time of 4 ns. The simulation is done for 5000 sample using s-LLGS and the parameters in Table 9.1.

9.2 Study overview

The difference between the various MRAM devices discussed in the section is the write mechanism. As such write power and current are key factors that distinguish the devices. Write current is strongly dependent on the WER and the switching time. We, therefore, decided to fix WER and switching time and evaluate other design metrics centered around these. Fig. 9.6 illustrates the generic overview of the comparative analysis presented later in the manuscript. The material parameters: saturation magnetization M_s , and interfacial

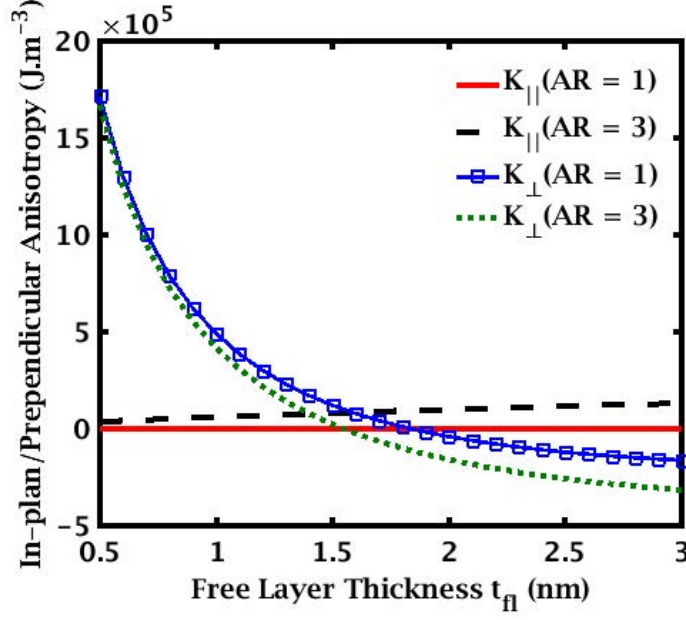


Figure 9.5. The in-plane and perpendicular anisotropy versus free layer thickness for PMA (AR = 1), and IMA (AR=3). The parameters used in these calculations are listed in Table 9.1.

anisotropy (K_i) are selected from recent experimental results [107]. The write current (I_w) is chosen to achieve iso-write error rate (iso-WER) of less than 7.95×10^{-7} at iso-switching time of 4ns [133]. The write current is estimated by running the s-LLGS equation for a sample of size greater than 5000 samples. The random thermal variations in the initial angle results in a distribution of switching time for a given write current. The current that achieves the desired write error probability is estimated by fitting WER after the transformation $\log(\frac{1}{WER} - 1)^{-1}$. The s-LLGS results and fitted curve are illustrated in Fig. 9.4.

The bit-cell layout is constructed according to the layout rules in [115]. The area is calculated in units of the minimum feature (F^2), and the half of the minimum feature $\lambda = F/2$. The minimum number of fins, that achieves the required write current, is selected using the compact MTJ SPICE model and the PTM FinFET model [108]. Finally, the read current, the write current, the read power and the write power are estimated using SPICE simulations.

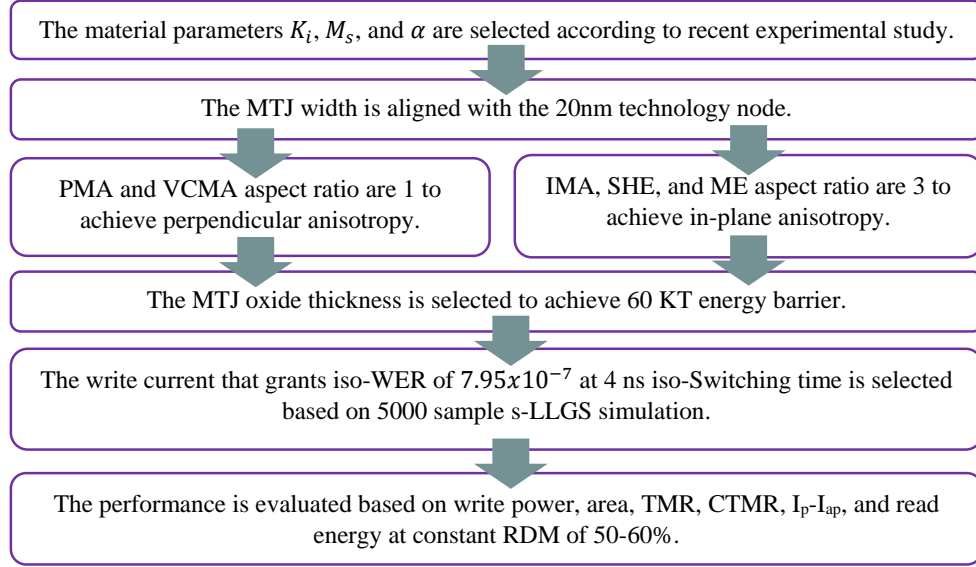


Figure 9.6. The overview of the study flow and the criterion of selecting the device parameters.

Table 9.1. Parameters used in s-LLGs simulations.

	PMA	IMA
Interface Anisotropy (K_i) erg/cm^2	1.3 [107]	1.3 [107]
Saturation Magnetization (M_s) emu/cm^3	1257.3 [107]	1257.3 [107]
Damping factor	0.05	0.01
Energy Barrier (E_B) KT	65	61.8
Aspect Ratio (AR)	1	3
Free Layer Minimum Diameter nm	20	20
Free Layer Thickness (t_{fl}) nm	0.5	2.4

9.3 PMA and IMA based bit-cells

The basic constraint applied to all the magnetic devices under study is to have an energy barrier (EB) greater than 60KT [114]. Recall, the energy barrier is a function of the FL dimensions and material parameters. Specifically, equations (9.12) – (9.14) [147], shown below, were used to estimate the energy barrier.

$$K_{\perp} = \frac{K_i}{t_{fl}} - \frac{1}{2}\mu_0 M_s^2 (N_{zz} - N_{xx}) \quad (9.12)$$

$$K_{\parallel} = \frac{1}{2}\mu_0 M_s^2 (N_{yy} - N_{xx}) \quad (9.13)$$

$$E_B = \begin{cases} K_{\perp} V & \text{PMA} \\ K_{\parallel} V & \text{IMA} \end{cases} \quad (9.14)$$

As expected, equations (9.12) – (9.14) demonstrate that for PMA (IMA) the perpendicular anisotropy (K_{perp}) should be greater (less) than the in-plane anisotropy (K_{\parallel}) for establishing the required EB. Using the material parameters shown in Table 9.1, we have plotted the K_{perp} and K_{\parallel} in Fig. 9.5. Based on Fig. 9.5, the selected FL thicknesses and aspect ratios for PMA and IMA are mentioned in Table 9.1.

Through our s-LLGS simulations, it was observed that the switching time is strongly influenced by the initial angle, which in turn, is a function of the random fluctuations caused due to thermal noise. Therefore, the write current that achieves the desired WER at 4ns iso-switching time was selected by running the s-LLGS equations over 5000 samples with different initial angles. The WER was estimated by extrapolation similar to the technique illustrated in Fig. 9.4. The write current for P-MTJ and I-MTJ for the required WER was found to be $117.8\mu A$ and $229\mu A$, respectively. The number of fins needed is 4 at $V_{DD} = 1.1V$. The MTJ resistance of PMA is higher than IMA based MTJ due to smaller cross-section area. The high resistance of PMA increases the source degeneration effect and requires the same number of fins as IMA, although IMA write current is higher than PMA.

The layout of the memory cell is shown in Fig. 9.8. The layout is for two fingers, four fins, and one MTJ bit-cell. The SL-Line and BL-line are assigned to metal 2, and 4, respectively. Metal 1 connects the fins. The two fingered layout is preferred because of the denser area compared to a single finger layout. The total bit-cell area is $48F^2$. Another advantage of the two fingered layout is the existence of two WL-lines compared to a single WL-line as in the case of the single finger design. Both WL-lines are raised during the write operation.

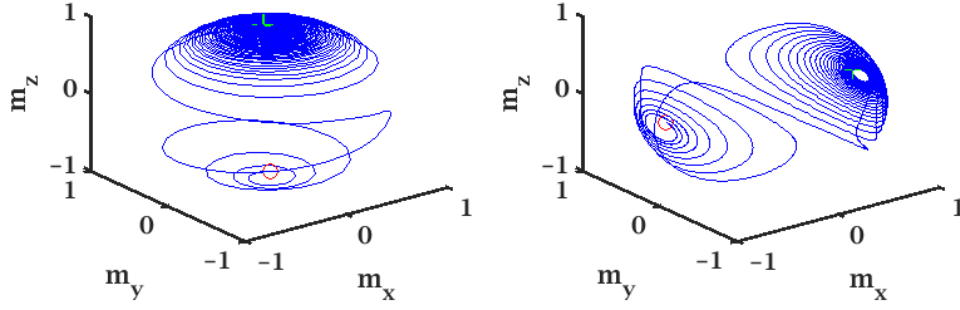


Figure 9.7. The magnetization trajectory of the PMA and IMA. The starting point is marked by the green plus sign, and the end point is marked by a red circle. The parameters used in this calculations are listed in Table 9.1.

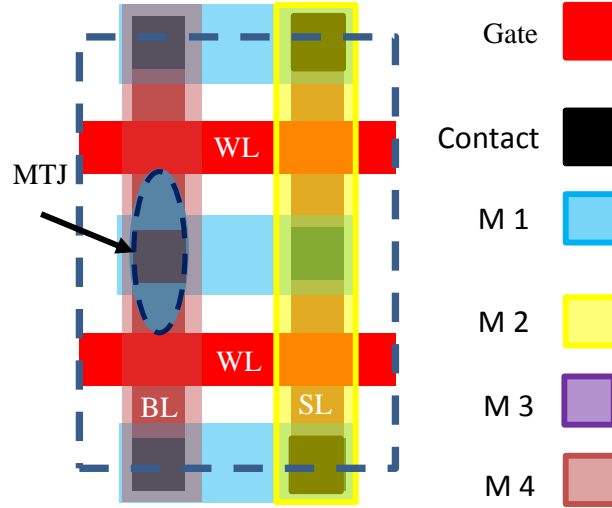


Figure 9.8. The layout of the 1T-1MTJ bit-cell. The width is 2 metal line limited of 12λ . The total area is $48F^2$.

During the read operation, either two WL-lines or single WL-line could be used to control the read current.

9.4 VCMA based bit-cells

As mentioned in the above sub-section, the typical current requirement for STT based memories is in range of $\sim 100\mu\text{A}$. Voltage controlled magnetic anisotropy (VCMA) [94], [131],

[134] has recently emerged as a viable option for reducing the switching current requirement for MTJ devices. The VCMA mechanism can be understood as follow, the applied voltage on the free layer of P-MTJ results in accumulation of charges on the interface between the magnet and the oxide layer. The accumulation of electrons at the interface changes the occupation of energy levels. The change in orbital occupation changes the perpendicular interface anisotropy due to the spin-orbit coupling [148].

The relation between the change in interfacial anisotropy due to the VCMA effect and the applied voltage is described in (9.15)[149], [150], where V_{MTJ} is the MTJ voltage, and ζ is the coupling parameter. If V_{MTJ} is increased until it reaches the critical voltage, $V_c = \frac{t_{ox}K_i}{\zeta}$ then $H_{anis}(V_c)$ will be zero and in presence of small in-plane field, the magnetization vector would start precessing around the in-plane field [94], [149], as shown in Fig. 9.9. Such precessionally switched VCMA MTJs have been reported and analyzed in various previous works including [94], [134], [137]. In addition, other switching mechanisms exploiting the VCMA effect, for example, as presented in [151] can be found in the literature. Authors in [151], use the VCMA effect and a fixed magnetic field to switch from the P to the AP state. For the AP to P switching, the pulse amplitude is increased, leading to increase in ‘Slonczewski’s STT’ as well as the ‘field like STT’ torque which switches the magnetization direction. However, proper functioning of the switching mechanism presented in [151] relies on close interplay between the VCMA and the STT effect. Specifically, for the VCMA dominated P to AP switching, when the switching probability is close to 1, the STT dominated AP to P switching should be zero to avoid any inadvertent switching and *vice-versa*. This requirement highly constrains the material and device design space for VCMA based bit-cells based on the switching mechanism proposed in [151]. We therefore rely on a more robust two step VCMA based write operation based on precessional magnetization dynamics explained below.

The two step write process is accomplished as follows and was originally proposed in [152]. In the first step, we apply a relatively high voltage pulse (V_{vcma}) to initiate the precessional motion, when the magnetization has made a half-cycle around the hard-axis we apply the second voltage pulse of a lower magnitude (V_{STT}) as shown in Fig. 9.9. The second pulse stabilizes the magnetization in the desired direction due to the STT effect. Thus, by exploiting combined VCMA and STT phenomenon we can achieve 180° switching of the

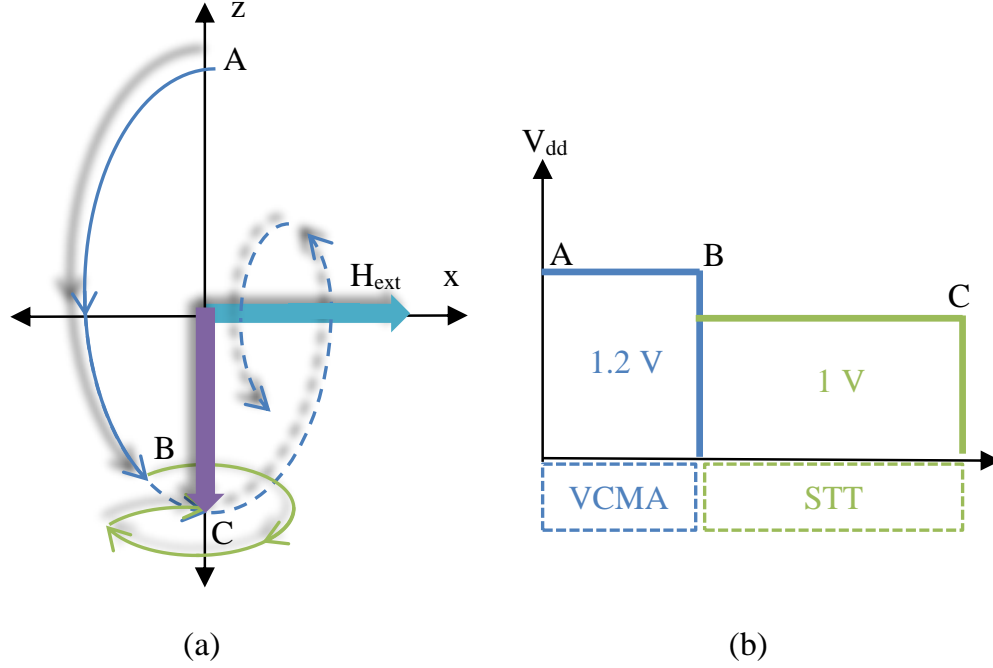


Figure 9.9. The VCMA write operation [134]. (a) The magnetization trajectory of the VCMA write mechanism. The blue line is the VCMA dominated phase. The green line is the STT dominated phase. (b) The supply voltage during the VCMA and STT dominated pulses.

magnetization direction. Note, the polarity of the second voltage pulse has to be changed from positive to negative depending whether the magnetization is being switched in P or AP direction.

However, with the current technology and material parameters, obtaining precessional switching in small cross-section VCMA-devices is a challenge. This is because at small dimensions in order to maintain a high E_B , the interface anisotropy has to be increased. The present experimentally demonstrated VCMA coefficients are not large enough to sufficiently reduce the interface anisotropy within desired voltage range on application of an electric field with such large interface anisotropy. As such, with the present parameters for smaller cross-section (20nm in this case), VCMA effect can only reduce the effective E_B , it is not able to sufficiently reduce the interface anisotropy required for precessional switching dynamics. Therefore, we used a predictive value of $\zeta = 1100 fJ/(V.m)$ which is the minimum value

that allows precessional switching at such small free layer dimensions corresponding to the parameters presented in Table 9.1.

$$H_{anis}(V_{MTJ}) = \frac{2}{\mu_0 M_{stfl}} \left(K_i - \frac{\zeta V_{MTJ}}{t_{ox}} \right) \hat{z} \quad (9.15)$$

By incorporating equation (9.15) [149], [150] in the s-LLGS equations, we ran 5000 simulations including both the ‘read-before-write’ and the two step switching process of Fig. 9.9. The obtained probability distribution is extrapolated for iso-WER and 4ns iso-switching time which is divided into 2ns for the read operation and 2ns for the write operation. The write current is $64\mu A$ at a supply voltage of $V_{DD} = 1.2V$ for the first pulse (VCMA dominated) and $37\mu A$ at 1V supply voltage for the second pulse (STT dominated). Note, these current values are almost half as compared to the STT based MTJs. This low switching current requirement allows one to increase the oxide thickness for the VCMA MTJ, in order to improve the sense margin, which would be explained in detail in later part of the manuscript. The chosen oxide thickness for VCMA MTJs is mentioned in Table 9.2.

Two fins were used to drive the MTJ. The cell layout and transistor connections are same as in Fig. 9.8 except that the number of fins is reduced to two and they are connected as one finger. A vertical distance of 3λ has to be added between the cells to separate the metal lines. The bit-cell area is $42F^2$.

Table 9.2. Summary of the bit-cells write bias. The VCMA has two voltage pulses P1 and P2.

	PMA	IMA	VCMA		SHE	ME
			P1	P2		
Supply voltage (V)	1.1	1.1	1.2	1	0.7	0.3
Write current (μA)	117.8	229	64	37	54	-
Oxide thickness (nm)	0.95	0.95	1.08		1.13	1.13
Number of <i>fins</i>	4	4	2		2	2

9.5 SHE based memory

As opposed to the two terminal devices like the STT and the VCMA based MTJs, three terminal devices with potential of achieving low write current as well as decoupled read and write ports are being actively investigated. The well-known spin Hall effect (SHE) provides an efficient mechanism for generating spin-polarized currents. SHE is a phenomenon in which a charge current can generate a spin current, wherein the spin generation efficiency can be greater than 1 [153]. SHE was predicted in 1971 by Dyakonov [154] and was later experimentally demonstrated by Hirsch [155]. The SHE based switching conventionally was used mainly for switching magnetization of IMA. Recently, Miron *et. al.* [156] observed experimentally that current in heavy metal could switch PMA as well. Miron *et. al.* [156] initially assumed that SHE is not enough to explain the stable switching of PMA and argued that the switching is dominated by Rashba effect field-like torque. Later Buhrman *et. al.* [95] could prove that SHE damped-like torque is the dominant driving force in PMA switching. Although the PMA has many attractive properties compared to IMA, deterministic PMA switching using SHE requires external magnetic field to break the symmetry [130]. Recently, Buhrman *et. al.* [157] demonstrated a deterministic switching of PMA using Spin Hall effect in absence of external magnetic field by engineering the energy landscape. SHE based MTJ has many attractive advantages compared to STT-MTJ as SHE-MTJ has lower write energy and lower write path resistance [130]. We limited this study to SHE-IMTJ as it has low write current compared to perpendicular SHE-PMTJs. Nevertheless, the trade-offs highlighted in the results section for SHE-IMTJ are qualitatively valid for SHE-PMTJ as well.

A SHE based MTJ is shown in Fig. 9.10. It consists of an MTJ stack etched on top of a heavy metal. When a charge current is passed through the heavy metal, the electron current splits into spin polarized current as shown in Fig. 9.10. This spin polarized current can be used to switch the free layer of the MTJ stack in contact with the heavy metal.

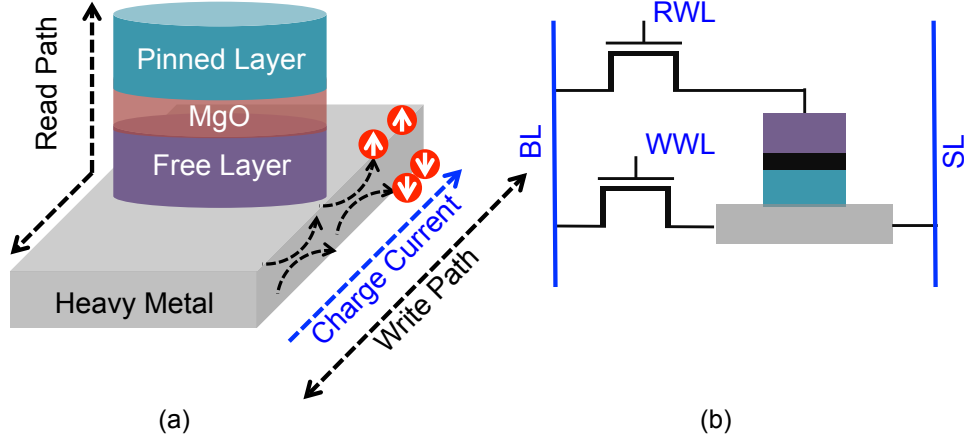


Figure 9.10. The schematic of SHE based MTJ stack and the schematic of SHE based memory bit-cell.

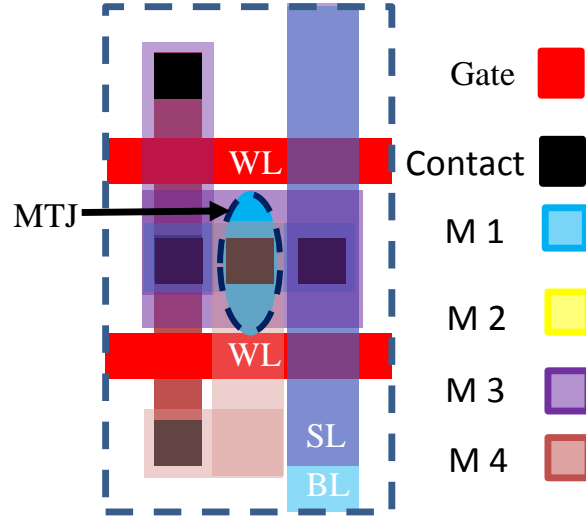


Figure 9.11. The layout of SHE based memory bit-cell. The total area is $66 F^2$.

The efficiency of the spin current generation by SHE is defined by equation (9.16), where P_{SHE} is the spin injection efficiency, ω is the width of the free layer, t is the thickness of the heavy metal, θ_{SHE} is the spin Hall angle and λ_{st} is the spin flip length [153].

$$P_{SHE} = \frac{I_{spin}}{I_{charge}} = \frac{\pi\omega}{4t}\theta_{SHE} \left(1 - \text{sech}\left(\frac{t}{\lambda_{st}}\right)\right) \quad (9.16)$$

Fig. 9.10 shows the circuit schematic for SHE based bit-cell. The circuit contains two transistors for read and write to avoid sneak paths [158]. The write operation is accomplished by applying a voltage between the SL-line and the BL-line. Reversing the voltage on the SL-line and BL-line will reverse the state of the MTJ. The read operation is carried out using the MTJ stack connected between the BL-line and SL-line through the transistor connected to the read word line. As the read and write have different paths, we can engineer the two paths independently to achieve the required write current. At the same time, the read path could be engineered to achieve higher TMR ratio by increasing the oxide thickness t_{ox} . The write current was estimated by running the s-LLGS equations over 5000 samples as in the case of STT. The write current that achieves iso-WER at iso-switching time of 4ns is $54\mu A$. The write supply voltage used is 0.7 V.

The layout of SHE based bit-cell is illustrated in Fig. 9.11. The BL-line and SL-line are assigned metal 1, and metal 3, respectively. The width of the cell is two metal limited. The total area is $66 F^2$, which is larger than both the STT and the VCMA based bit-cells due to the three terminal nature of the SHE device.

9.6 ME based memory

As opposed to current induced switching in case of STT or SHE based MTJs and voltage assisted switching in case of VCMA MTJs, there have been active investigation of pure voltage driven switching of ferro-magnets using the magneto-electric (ME) effect. For example, a two-phase coupling arises when a voltage is applied to piezoelectric material that is in contact with a magnetostrictive ferromagnetic layer. The dimensions of piezoelectric material change under the effect of the external voltage. This change in dimensions strains the magnetostrictive material that induces a resulting strain anisotropy which could switch the magnetization [159]–[161]. In addition, materials like $BiFeO_3$ and Cr_2O_3 are able to couple the electric field applied across the material to the exchange bias field that could switch a nanomagnetic layer by switching the exchange bias surface interaction [162].

In this study, we use a compact model of the magneto-electric coupling phenomena which is defined in (9.17) [163] where, H_{ME} is the induced magnetic field, V_{ME} is the applied voltage, α_{ME} is the magneto-electric coupling constant, and t_{ME} is the thickness of the

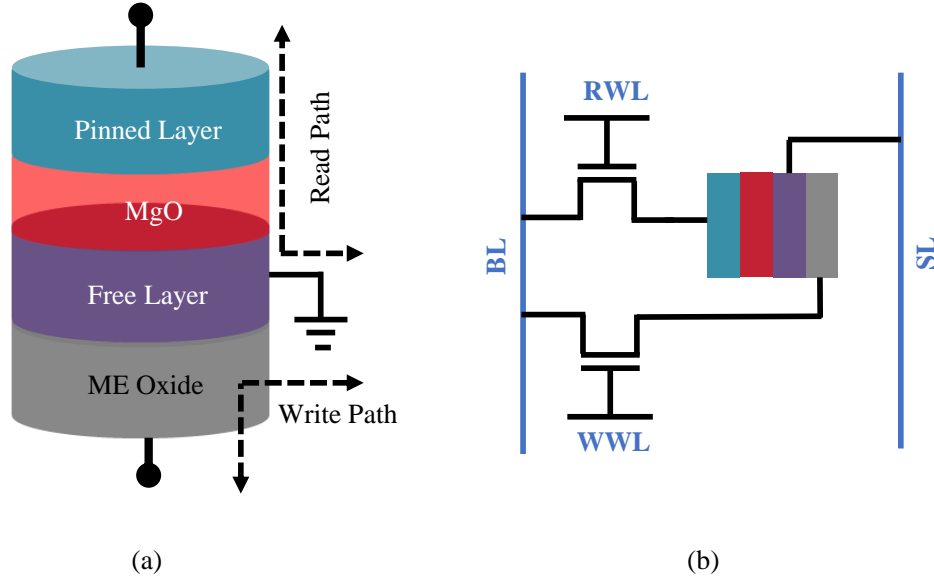


Figure 9.12. ME based memory bit-cell with the read and write paths are annotated on ME stack.

piezoelectric layer. The magnetic field in (9.17) is added to H_{eff} in (9.3) during the numerical solution of the s-LLGS equation. In most of the experimental and numerical studies, the magneto-electric coupling constant α_{ME} is between 40 and 60 mV/(cm.Oe). In this study, $\alpha_{ME} = 50 \text{ mV}/(\text{cm.Oe})$ [163] and $t_{me} = 2.4 \text{ nm}$ are used in all of the simulations.

$$H_{ME} = \frac{\alpha_{ME} V_{ME}}{t_{ME}} \quad (9.17)$$

ME based memory cell is illustrated in Fig. 9.12 with the read and write paths annotated. The separate read and write paths allow improving the TMR of the memory cell by increasing the oxide thickness, without affecting the write operation. When a positive (negative) voltage is applied across the ME oxide, the MTJ switches to P (AP) state. ME switching does not incur static energy dissipation due the fact that ME oxides are expected to be insulators and hence would not lead to any static current flow during the write operation. The read operation is accomplished by passing read current through the MTJ stack as demonstrated in Fig. 9.12.

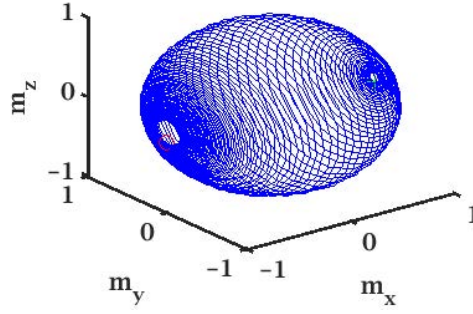


Figure 9.13. The magnetization trajectory of ME based memory. The start and end points are marked by the green plus sign and red circle, respectively. The parameters used for this simulation is listed in Table 9.1.

The write voltage is selected based on the same criterion that is used for all memory cells. Based on 5000 samples of different initial angles, the voltage that achieves iso-WER at iso-switching time of 4ns is 0.2 V. Leaving some margin, the supply voltage was selected to be 0.3 V. The trajectory of the magnetization during the switching process is illustrated in Fig. 9.13.

The layout of ME based memory cell is same as SHE based memory cell Fig. 9.11. The bit-line (BL) and source-line (SL) are assigned to metal 1 and metal 3, respectively. The width of the cell is two metal limited and the total area is $66F^2$. As expected, both the SHE and the ME devices are three terminal devices and need two transistors per bit-cell as a result they have the same bit-cell area.

In sections 9.3-9.6, we have seen how the various physics of the switching mechanisms dictate the write current requirement, the device structure, the bit-cell circuit, the transistor sizes and the layout area. We would now concentrate on the other important aspect of memory devices *i.e.* the read operation or the sensing scheme. We would first discuss the sense amplifier used for our read analysis. Subsequently, we will use some key metrics to analyze the effectiveness of the read operation for the different spin based devices considered in this work.

9.7 Sense amplifier

The sensing of almost all forms of spin based devices exploits the well-known physics of the tunnel magneto resistance (TMR) phenomenon. Although numerous sense-amplifiers for spin based memories [98], [164]–[166] have been presented in various previous works, the fundamental principle is to sense the resistance difference of the MTJ using either a current or a voltage based sense-amplifier. For a realistic evaluation of the read robustness, energy and performance for various bit-cells discussed in this work, it is imperative to include the sense-amplifier circuit for proper evaluation of the key sensing metrics. In this section, we would focus on the well know cross-coupled inverter based current and voltage sense amplifiers. Although more complex sense amplifiers using voltage boosting [90], negative differential resistance [167] etc. have been proposed in the literature, but the overhead associated with such complex sense amplifiers make them unattractive from practical implementation point of view. In fact, almost all STT-MRAM array level demonstrations use some variant of the cross-coupled inverter based sense-amplifier [168], [169]. In this section, we would describe voltage based sense-amplifiers used for read analysis of the various bit-cells and we will justify the rational behind focusing on the voltage sense amplifier.

The operation of the differential voltage amplifier that is illustrated in Fig. 9.14 can be understood as follows. After charging OUT1 and OUT2 to an equal voltage by the pre-charge circuit, the charging circuit is disconnected and WL is raised high and SE2 is set low to drive the voltage at V1 and V2 to its steady state value. After V1 and V2 reach the steady state, the CL signal will be turned high to connect the memory to the sense amplifier. The reference and memory cell are connected to V_{DD_read} using pFET. The voltage on V1 and V2 are determined only by the resistance of the memory cell independent of the capacitance at steady state, as illustrated by the time diagram in Fig. 9.15. Beside simplicity of the voltage sense amplifier, the evaluation of the MTJ resistance relies only on the steady state voltage difference $|V1 - V2|$, which provides immunity against line capacitance difference between the reference cell and the long metal lines of the memory column. In contrast, the current sense amplifier relies on discharging the pre-charged (equalized) line capacitance through the memory MTJ and the reference MTJ. The asymmetry in the the bit-line capacitance

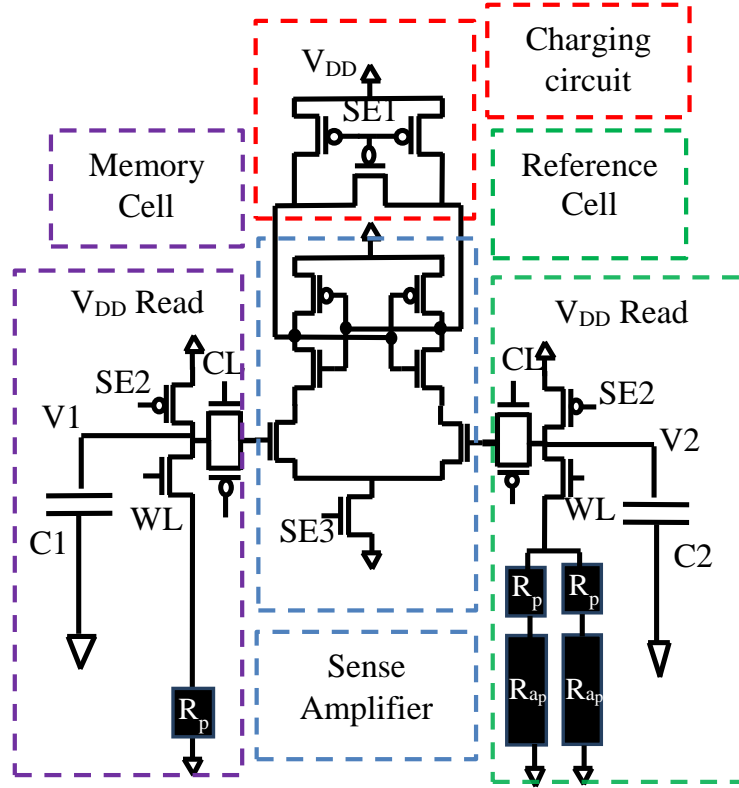


Figure 9.14. The schematic diagram of the differential voltage sense amplifier.

and the capacitance associated with the reference cell further complicates the functioning of current based sense amplifiers. On the other hand, the voltage sense amplifier rely on steady state voltage which is completely independent of the capacitance value. Moreover, the memory cell and reference cell are driven by a separate voltage level (V_{DD_read}) that is less than the actual supply voltage (V_{DD}) of the sense amplifier. Therefore, the read disturb failure probability can be lowered by appropriate choice of V_{DD_read} . A detailed analysis of the read operation using the sense amplifier described above is presented in the next section.

9.8 Results and analysis

9.8.1 Write Power and Bit-Cell area

We now present, the analysis results for various bit-cells considered in this work in a comparative manner. The major constrains that are forced for all memory cells, are an energy barrier over 60 KT , iso-WER lower than 7.95×10^{-7} at 4 ns iso-switching time and

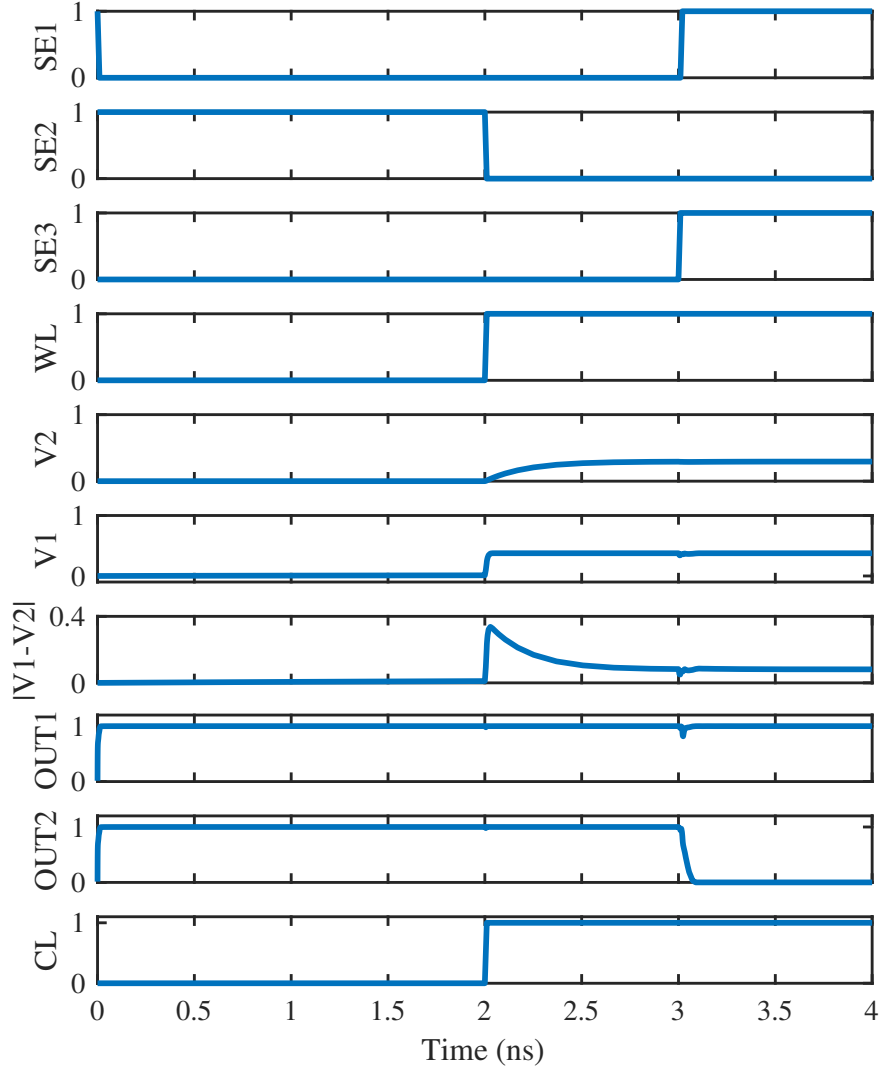


Figure 9.15. The simulation waveform of the differential voltage sense amplifier in case of $C1 \gg C2$. The simulation is done using SPICE. The OUT1 and OUT2 have the correct read output.

an RDM (read disturb margin) ratio of 50–60%. The readability of the bit-cells are evaluated using various performance metrics like, the TMR, CTMR (cell-TMR) and RSM (read sense margin). The TMR ratios of all the devices are computed at constant supply voltage of 0.25V. The RSM is defined as $|V_p - V_{ap}|$, where V_p and V_{ap} is the voltage at the input if the sense-amplifier when the MTJ is in P and AP state, respectively. The CTMR is evaluated

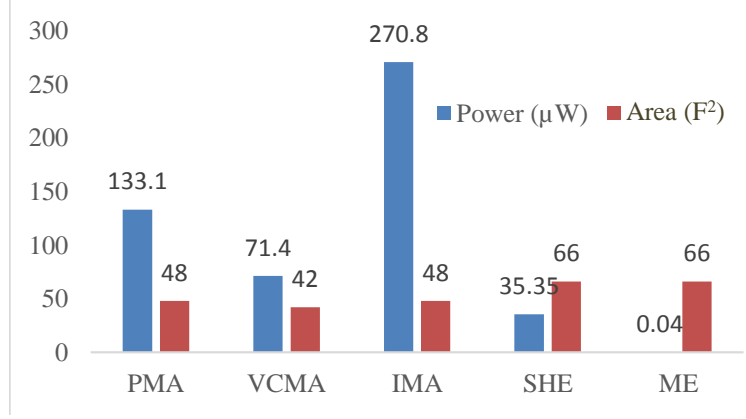


Figure 9.16. The average write power and layout area for the various bit-cells in units of (F^2).

at a constant RDM ratio between 50 – 60% for all the bit-cells. The high write current and the associated source degeneration limits the oxide thickness in case of PMA and IMA based bit-cells. The oxide thickness and biasing details of all the bit-cells are summarized in Table 9.2. Note, the oxide thickness for VCMA bit-cells can be kept higher due to its low switching current requirement. Higher oxide thickness of 1.13 nm for SHE and ME bit-cells are chosen due to existence of separate read-write paths. The sense amplifier energy consumption is included in the read energy calculations.

As shown in Fig. 9.16, ME based memory has the minimum write power which is less than SHE based memory and PMA/IMA based STT-MRAM because ME switching mechanism relies on electric field at zero static current. The ultra-low write power is a very attractive property of ME based memory compared to other magnetic switching methods. SHE based memory has a write power of $35\mu W$ which is a factor of 4 less than PMA based STT-MRAM and a factor of 8 less than IMA based STT-MRAM. This write efficiency of SHE is due to the better spin Hall effect efficiency of converting the charge current to spin current as compared to the STT based bit-cells. VCMA bit-cell has less write power compared to PMA because the voltage assisted switching is more efficient than STT based switching. The high write current and high write power of IMA bit-cell is due to the large volume of I-MTJ free layer which is elliptic with aspect ratio of 3 compared to the circular PMA cross-section.

SHE and ME are 3 terminal devices that have same number of fins per cell. As a consequence, SHE and ME based bit-cell have same area of $66F^2$ which is a factor of 1.4 higher than STT-MRAM that has an area of $48F^2$. VCMA has the minimum bit-cell area of $42F^2$ because VCMA has only 2 fins compared to 4 fins per bit-cell in case of PMA and IMA which is a consequence of the VCMA write efficiency. The PMA and IMA based STT-MRAM bit-cell have the same area and same number of fins because PMA has lower write current but higher resistance which increases the source degeneration and therefore requires same number of fins as IMA based bit-cell. The bit-cell areas of different memory cells are illustrated in Fig. 9.16. The point to highlight is the fact that the cell area of all the 5 memory technologies is limited by the metal lines and number of fins. In other words, the bit cell area is independent of the MTJ dimensions.

ME bit-cell has the lowest write power and largest cell area. In contrast, STT-MRAM (PMA and IMA) bit-cell has a denser bit-cell layout and the highest write power. For SHE based memory, write power is a compromise between the two extremes of STT-MRAM and ME based bit-cells. Furthermore, the write power of VCMA based memory is $53\mu W$ less compared to PMA based STT-MRAM and VCMA bit-cell area is slightly less compared to the STT-MRAM bit-cell. The comparative analysis described above illustrates the write-power and layout area trade-off presented by the various bit-cells due to difference in their underlying switching physics.

9.8.2 Read Performance

The TMR ratio for various bit-cells and their corresponding oxide thicknesses are illustrated in Fig. 9.17. Although the TMR of the various bit-cells are in the range of 150% – 160%, the absolute value of the parallel and anti-parallel resistances are substantially different. This is due the fact that the increase in oxide thickness increases the overall MTJ resistance exponentially. The increase in the MTJ resistances would imply higher RC time constant that would adversely effect the read sensing speed. Therefore, in Fig. 9.17 on the right hand side axis we have also plotted the the RC time constants for all the bit-cells as a function of their oxide thicknesses.

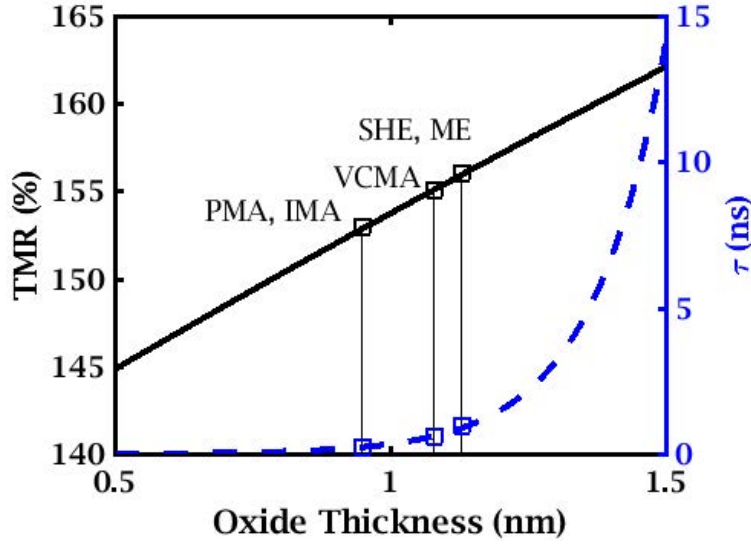


Figure 9.17. The TMR ratio for single fin and single IMA based MTJ versus oxide thickness at a constant supply voltage of 0.25 V. The time constant of the memory cell assuming 25 fF column metal line capacitance is plotted on the secondary axis.

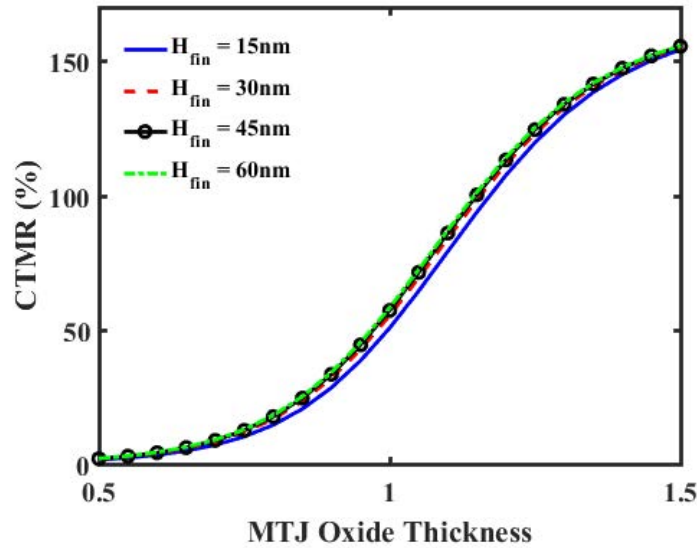


Figure 9.18. The CTMR ratio of a single fin and single IMA based MTJ versus oxide thickness at constant supply voltage of 0.25 V.

The CTMR, on the other hand, is a function of the oxide thickness as well as the size of the access (or the read) transistor. Higher the oxide thickness better is the CTMR Fig. 9.18, while a smaller read transistor tends to lower the CTMR ratio. Fig. 9.19 shows the CTMR

ratio for various bit-cells for a constant RDM in the range of 50%-60%. It can be observed that the CTMR for IMA, SHE and ME based bit-cells are in the same range. Although, SHE and ME bit-cells have higher oxide thickness as compared to the IMA bit-cell, yet they have smaller read transistors due to layout area constrain, thereby leading to comparable CTMR ratios. The CTMR for VCMA bit-cell is higher, since, although it has higher oxide thickness, being a two terminal device the access transistor size is larger as compared to the SHE and ME bit-cells leading to better CTMR ratio. For PMA bit-cell, the higher MTJ resistance due to smaller cross-section area coupled with the fact that the driving transistor size is larger than the SHE and ME devices leads to higher CTMR compared to the IMA, SHE and ME bit-cells. Thus, the CTMR ratio is dictated by the interplay between the device TMR, its absolute resistance and the resistance of the series access transistor.

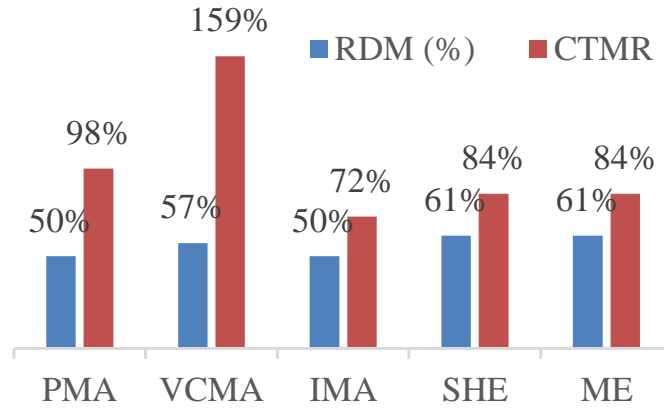


Figure 9.19. The RDM, and CTMR ratios calculated with RDM is kept limited between 50-60%.

Let us now consider the absolute difference in the read currents flowing through the various bit-cells in parallel and anti-parallel state. In Fig. 9.20 , we have plotted the $I_p - I_{ap}$ as a function of the oxide thickness for a particular device. As the oxide thickness increases the difference in current increases as well due to increase in device TMR. However, if the oxide thickness is further increased the rapid increase in the absolute resistance of the the device degrades the difference in the parallel and anti-parallel read current for constant read voltage. Thus, for sensing a difference in current there exists an optimum oxide thickness

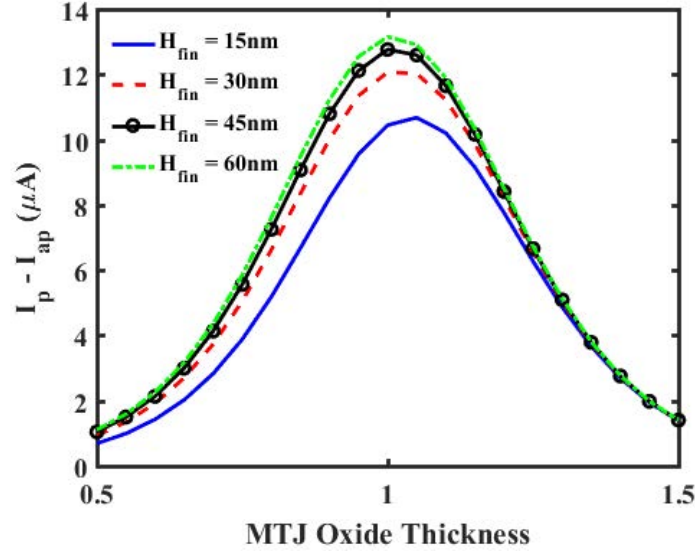


Figure 9.20. The parallel and antiparallel read current difference for single fin and single IMA based MTJ versus oxide thickness at constant supply voltage 0.25 V.

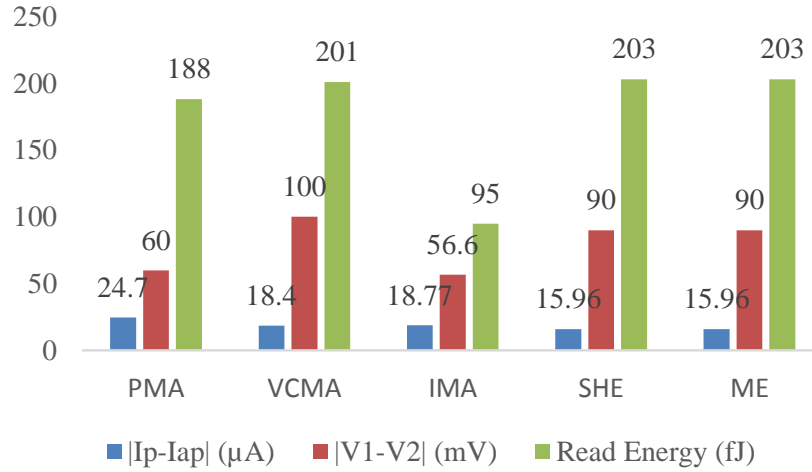


Figure 9.21. The parallel and antiparallel read current difference, the input voltage of the differential voltage sense amplifier, and the average read energy per single bit read using the differential voltage sense amplifier at constant RDM of 50 – 60%.

which leads to better TMR without degrading the current difference due to increased device resistance.

Based on the insights with respect to the CTMR and the $I_p - I_{ap}$ difference, we can now understand the current difference obtained for various bit-cells as shown in Fig. 9.21. SHE and ME based bit-cells have almost same $I_p - I_{ap}$ as the IMA based bit-cells due their similar CTMR ratios. Note, the $I_p - I_{ap}$ for SHE and ME bit-cells is slightly lower due to their higher resistances. On the other hand, although VCMA bit-cell has higher CTMR, the high resistance of the VCMA cell degrades its $I_p - I_{ap}$ difference. As such, PMA device, which has comparatively higher CTMR and also relatively lower resistance as compared to the VCMA, SHE and ME devices shows higher $I_p - I_{ap}$ margin. In summary, the read performance metric like the TMR, CTMR and the $I_p - I_{ap}$ difference is a strong function of the relative resistances of the magnetic device and the access transistors. In general, devices having higher absolute resistances, given the limited CTMR ratios, lead to degraded $I_p - I_{ap}$ that would make current based sensing difficult for such devices. In other words, there is design trade-off between the CTMR and $I_p - I_{ap}$.

9.8.3 Sense Amplifier and Read Energy

As discussed earlier, the differential voltage sense amplifier is preferred because it has two different supply voltages – one can be scaled for full output swing and the other could be scaled to achieve the required read current and RDM ratio. In addition, the asymmetric input capacitance is more tolerable in case of differential voltage sense amplifier. Therefore, we estimated the read energy based on the differential voltage sense amplifier.

The difference in voltage at the differential voltage sense amplifier inputs is shown in Fig. 9.21. VCMA has the highest difference of 100 mV because it has a higher oxide thickness than STT-MRAM and double the number of fins compared to SHE and ME, and hence higher CTMR as mentioned earlier. PMA based memory has a higher value for the difference $|V_1 - V_2|$ compared to IMA based memory, because IMA based STT-MRAM has larger MTJ surface area, and hence less CTMR ratio. SHE and ME have high $|V_1 - V_2|$ value of 90 mV because they have high oxide thickness of 1.13 nm. In contrast to the case of PMA and IMA, SHE and ME have different read and write paths which allow increasing the oxide thickness without degrading the writability.

The read energy of single bit read operation including the sense amplifier energy dissipation at almost constant RDM between 50 – 60% is illustrated in Fig. 9.21. IMA has the least read energy because IMA has the least MTJ resistance, and hence it has the least read voltage at constant RDM ($I_p = I_c/2$). Therefore, IMA has the lowest read voltage and the lowest read energy. In contrast, VCMA, SHE and ME have the highest read energy as they have higher read voltage and higher MTJ resistance at the same RDM. The contrast between IMA that has lowest read energy and lowest $|V1 - V2|$, and VCMA/SHE/ME that has highest read energy and highest $|V1 - V2|$ illustrate the expected tradeoff between the power consumption and readability. PMA readability is a compromise between the two extreme cases of IMA and VCMA/SHE/ME. Finally, it is important to mention that the read energy of ME is higher than its write energy which reflects the importance of the read energy in the scaling trend of ME based memories.

10. SUMMARY

In this thesis, we propose a modeling and simulation framework that captures the behavior of MFTJ as a four-state device. Furthermore, the DFT method is used to estimate the screening length of the electrodes that have a strong influence on the TER. The estimated screening lengths are used in the quantum transport calculations to mimic the realistic device behavior at different bias voltages. The TER and TMR estimated by the proposed framework is compared with the experimental results of LSMO/LCMO/BTO/LSMO [11]. The quantum transport and magnetization dynamics could show the dependence of the device resistance on the external applied magnetic field. The dependence of the MFTJ resistance on the external magnetic field is in agreement with the experimental results in [11] that confirms the transition from the FM to the AFM phase in the LCMO electrode.

Our analysis illustrates that not only the TMR but also the TER of the MFTJ depends on splitting energy because of the magnetoelectric effect at the interface that originates from the LCMO electrode phase transition from the FM to the AFM phase. On the other hand, the contrast between the weak and strong exponential dependence of the TER on the barrier height and electrodes screening length ratio, respectively is analyzed. The barrier height that is dependent on the electrodes and insulator work functions, could increase the MFTJ high and low resistance. Consequently, the power and speed of the MFTJ sensing could be enhanced by choosing the insulator and electrodes that have the appropriate work functions. However, the ratio of the electrodes screening length δ_1/δ_2 could exponentially enhance the TER ratio. Finally, our analysis reveals that the TER effect is improved by the asymmetry exhibited by the built-in potential that results in average barrier height modulation by electric polarization.

Based on the time-dependent perturbation theory, we could derive a mathematical formulation that relates the magnetic exchange interaction coefficient to the time evolution of electric polarization (3.20)-(3.21). This formulation is an important step toward a consistent model of MFTJs. The formulation emphasizes that the magnetization switching from FM to AFM alignment induced by polarization reversal follows a precessional motion. The transient response of the MFTJ exhibits a transition from Nordheim tunneling to direct tunneling

and back to Nordheim tunneling current during the polarization switching. The transient response of the MFTJ demonstrates a set of oscillations due to the magnetic precessional motion. Although the switching from the FM to AFM alignment is induced by the electric polarization switching, the thermal magnetic fluctuations still assist the magnetization motion especially at the start of the switching.

In section 5, we propose a model that explains the physical origin of the AFTJ high on/off current ratio. The proposed AFTJ model is fitted over experimental results to validate the ability of the model to predict the AFTJ current characteristics. The AFTJ model is implemented in Verilog-A. The study demonstrates the different biasing points of the AFTJ as an oscillator. The AFTJ based coupled-oscillator network is applied to solve the graph coloring problem. The HSPICE simulation of the AFTJ based coupled-oscillator network demonstrates the ability of the network to approximate the solution of the graph coloring problem. The simulations also show a significant improvement in the power dissipation compared to other emerging oscillators.

In section 6, we derive an oscillator-coupling function for improving the approximate solution of the graph coloring problem. The stability of the proposed model is investigated analytically. The proposed model tries to minimize the intra-cluster distance and maximize the inter-clusters distance. The proposed model shows a significant improvement compared to the original Kuramoto model. In section 7, a new area and energy efficient NVFF is proposed and investigated based on spin Hall effect magnetic tunnel junction. Our simulation results show 3.2x and 1.6x average power and area improvement, respectively compared to previous works. Finally, the factors that contribute toward the improvements in area and energy are analyzed insightfully. The analysis highlighted four factors behind the improvements: 1) the use of single SHE-MTJ instead of two SHE-MTJs, 2) the simplicity of the steady state voltage divider based restore operation, 3) the utilization of NOT gates to amplify the restore signal, and 4) the decoupled backup and restore circuit and device paths.

In section 8, we have proposed a new functional sensing scheme for in-memory Boolean operations based on 1T-1R memory arrays. We rely on the well-known cross-coupled inverter based sense amplifiers as the basic sensing circuit. We first show that the conventional scheme with the aforementioned sense-amplifiers are of limited applicability for in-memory

Boolean operations due to low-sense-margin. Further, the sense-margin does not improve with improvement in ON-OFF ratios. As such, to exploit high ON-OFF ratios of emerging memory technologies, we propose use of staggered activation of the word-lines and skewing the sense-amplifiers for robust read operations. We show in-memory XOR, IMP and bit-wise comparison can be easily accomplished by the use of presented staggered activation scheme. A key highlight of the presented proposal is the fact that as opposed to the conventional scheme, the sensing-robustness of the proposed scheme steadily increases with increase in the ON-OFF ratio of the constituting memory elements. Keeping in view the extensive research investigation for improved ON-OFF resistances we believe the presented proposal is well-suited for future non-volatile in-memory bitwise Boolean operations.

Spin based magnetic memories are front runners for potential replacement of on-chip silicon based caches. Recently, spin based memories based on various physical switching mechanisms have been explored in the literature. In section 9, we do a comprehensive, comparative analysis of different bit-cells based on the different switching mechanisms *viz.* the STT based IMA and PMA memories, VCMA driven bit-cells and bit-cells exploiting the SHE and the ME effect. Our analysis shows, STT based PMA and IMA memories offer dense areal integration, however suffer from both high write energy requirement and comparatively low read sense margins. On the other extreme, SHE and ME memories offer more energy efficient write operation and higher read sense margin at the cost of increased bit-cell area. The write energy for VCMA based bit-cells is a compromise between the STT based memories and the SHE/ME based memories. However, VCMA bit-cells have lowest layout area and also improved read sense margin. It can thus be observed that there is no single device that supersedes all the other devices with respect to readability, bit-cell area and write efficiency, simultaneously. As such, the comparative analysis presented in this manuscript helps to put the various bit-cells in proper perspective and highlights the different trade-offs.

REFERENCES

- [1] G. Moore, “Cramming More Components Onto Integrated Circuits,” *Proceedings of the IEEE*, vol. 86, no. 1, pp. 82–85, Jan. 1998. DOI: [10.1109/JPROC.1998.658762](https://doi.org/10.1109/JPROC.1998.658762).
- [2] M. Chang, P. Rosenfeld, S. Lu, and B. Jacob, “Technology comparison for large last-level caches (L3Cs): Low-leakage sram, low write-energy stt-ram, and refresh-optimized edram,” in *2013 IEEE 19th International Symposium on High Performance Computer Architecture (HPCA)*, 2013, pp. 143–154. DOI: [10.1109/HPCA.2013.6522314](https://doi.org/10.1109/HPCA.2013.6522314).
- [3] Y. Ye, S. Gummalla, C.-C. Wang, C. Chakrabarti, and Y. Cao, “Random variability modeling and its impact on scaled CMOS circuits,” *Journal of computational electronics*, vol. 9, no. 3-4, pp. 108–113, 2010, doi: [10.1007/s10825-010-0336-5](https://doi.org/10.1007/s10825-010-0336-5).
- [4] K. C. Chun, H. Zhao, J. D. Harms, T. Kim, J. Wang, and C. H. Kim, “A scaling roadmap and performance evaluation of in-plane and perpendicular MTJ based STT-MRAMs for high-density cache memory,” *IEEE Journal of Solid-State Circuits*, vol. 48, no. 2, pp. 598–610, 2013. DOI: [10.1109/JSSC.2012.2224256](https://doi.org/10.1109/JSSC.2012.2224256).
- [5] A. Chanthbouala, A. Crassous, V. Garcia, K. Bouzehouane, S. Fusil, X. Moya, J. Allibe, B. Dlubak, J. Grollier, S. Xavier, C. Deranlot, A. Moshar, R. Proksch, N. D. Mathur, M. Bibes, and A. Barthelémy, “Solid-state memories based on ferroelectric tunnel junctions,” *Nature Nanotechnology*, vol. 7, no. 2, pp. 101–104, 2012. DOI: [10.1038/nnano.2011.213](https://doi.org/10.1038/nnano.2011.213).
- [6] V. Garcia and M. Bibes, “Ferroelectric tunnel junctions for information storage and processing,” *Nature Communications*, vol. 5, no. 1, p. 4289, Dec. 2014. DOI: [10.1038/ncomms5289](https://doi.org/10.1038/ncomms5289).
- [7] Y. Yin and Q. Li, “A review on all-perovskite multiferroic tunnel junctions,” *Journal of Materiomics*, vol. 3, no. 4, pp. 245–254, 2017, ISSN: 23528478. DOI: [10.1016/j.jmat.2017.09.001](https://doi.org/10.1016/j.jmat.2017.09.001).
- [8] a. L. Esaki, R. B. Laibowitz, and P. J. Stiles, “Polar switch,” *IBM Tech. Discl. Bull*, vol. 13, no. 2161, p. 114, 1971.
- [9] D. Pantel and M. Alexe, “Electroresistance effects in ferroelectric tunnel barriers,” *Phys. Rev. B*, vol. 82, p. 134 105, 13 Oct. 2010. DOI: [10.1103/PhysRevB.82.134105](https://doi.org/10.1103/PhysRevB.82.134105).
- [10] J. D. Burton and E. Y. Tsymbal, “Prediction of electrically induced magnetic reconstruction at the manganite/ferroelectric interface,” *Physical Review B*, vol. 80, no. 17, p. 174 406, 2009. DOI: [10.1103/PhysRevB.80.174406](https://doi.org/10.1103/PhysRevB.80.174406). arXiv: [0904.1726](https://arxiv.org/abs/0904.1726).

- [11] Y. W. Yin, M. Raju, W. J. Hu, J. D. Burton, Y.-M. Kim, A. Y. Borisevich, S. J. Pennycook, S. M. Yang, T. W. Noh, A. Gruverman, X. G. Li, Z. D. Zhang, E. Y. Tsymbal, and Q. Li, “Multiferroic tunnel junctions and ferroelectric control of magnetic state at interface (invited),” *Journal of Applied Physics*, vol. 117, no. 17, p. 172 601, May 2015. DOI: [10.1063/1.4913753](https://doi.org/10.1063/1.4913753).
- [12] A. G. Zembilgotov, N. A. Pertsev, H. Kohlstedt, and R. Waser, “Ultrathin epitaxial ferroelectric films grown on compressive substrates: Competition between the surface and strain effects,” *Journal of Applied Physics*, vol. 91, no. 4, pp. 2247–2254, Feb. 2002. DOI: [10.1063/1.1427406](https://doi.org/10.1063/1.1427406).
- [13] H. Qu, W. Yao, T. Garcia, J. Zhang, A. V. Sorokin, S. Ducharme, P. A. Dowben, and V. M. Fridkin, “Nanoscale polarization manipulation and conductance switching in ultrathin films of a ferroelectric copolymer,” *Applied Physics Letters*, vol. 82, no. 24, pp. 4322–4324, 2003. DOI: [10.1063/1.1582366](https://doi.org/10.1063/1.1582366).
- [14] J. Rodriguez Contreras, H. Kohlstedt, U. Poppe, R. Waser, C. Buchal, and N. A. Pertsev, “Resistive switching in metal–ferroelectric–metal junctions,” *Applied Physics Letters*, vol. 83, no. 22, pp. 4595–4597, 2003. DOI: [10.1063/1.1627944](https://doi.org/10.1063/1.1627944).
- [15] M. Y. Zhuravlev, R. F. Sabirianov, S. S. Jaswal, and E. Y. Tsymbal, “Giant electroresistance in ferroelectric tunnel junctions,” *Phys. Rev. Lett.*, vol. 94, p. 246 802, 24 Jun. 2005. DOI: [10.1103/PhysRevLett.94.246802](https://doi.org/10.1103/PhysRevLett.94.246802).
- [16] M. Y. Zhuravlev, Y. Wang, S. Maekawa, and E. Y. Tsymbal, “Tunneling electroresistance in ferroelectric tunnel junctions with a composite barrier,” *Applied Physics Letters*, vol. 95, no. 5, p. 52 902, 2009. DOI: [10.1063/1.3195075](https://doi.org/10.1063/1.3195075).
- [17] J. A. Appelbaum, “Tunneling in solids. c. b. duke. academic press, new york, 1969. xii + 356 pp. illus. 16. solid state physics, supplement 10,” *Science*, vol. 167, no. 3922, pp. 1244–1244, 1970. DOI: [10.1126/science.167.3922.1244](https://doi.org/10.1126/science.167.3922.1244).
- [18] E. O. Kane, *Tunneling Phenomena in Solids eds E. Burnstein and S. Lundquist*. Springer, 1969.
- [19] E. L. Wolf, “Principles of Tunneling Spectroscopy, New York: Oxford Univ,” *Pres s*, 1985.
- [20] H. Kohlstedt, N. Pertsev, J. R. Contreras, and R. Waser, “Theoretical current-voltage characteristics of ferroelectric tunnel junctions,” *Physical Review B*, vol. 72, no. 12, p. 125 341, 2005.
- [21] N. Hinsche, M. Fechner, P. Bose, S. Ostanin, J. Henk, I. Mertig, and P. Zahn, “Strong influence of complex band structure on tunneling electroresistance: A combined model and ab initio study,” *Physical Review B*, vol. 82, no. 21, p. 214 110, 2010.

- [22] M. Fechner, I. Maznichenko, S. Ostanin, A. Ernst, J. Henk, P. Bruno, and I. Mertig, “Magnetic phase transition in two-phase multiferroics predicted from first principles,” *Physical Review B*, vol. 78, no. 21, p. 212 406, 2008.
- [23] S.-C. Chang, A. Naeemi, D. E. Nikonov, and A. Gruverman, “Theoretical approach to electroresistance in ferroelectric tunnel junctions,” *Phys. Rev. Applied*, vol. 7, p. 024 005, 2 Feb. 2017.
- [24] R. Andrawis and K. Roy, “Nonequilibrium green’s function and first-principles approach to modeling of multiferroic tunnel junctions,” *Phys. Rev. Applied*, vol. 12, p. 014 003, 1 Jul. 2019. DOI: [10.1103/PhysRevApplied.12.014003](https://doi.org/10.1103/PhysRevApplied.12.014003).
- [25] S. Datta, *Lessons from nanoelectronics: a new perspective on transport*. World Scientific publishing company, 2012, vol. 1.
- [26] M. Julliere, “Tunneling between ferromagnetic films,” *Physics Letters*, vol. 54, no. 3, p. 225, 1975, ISSN: 0375-9601. DOI: [https://doi.org/10.1016/0375-9601\(75\)90174-7](https://doi.org/10.1016/0375-9601(75)90174-7).
- [27] J. Mathon and A. Umerski, “Theory of tunneling magnetoresistance of an epitaxial Fe/MgO/Fe (001) junction,” *Physical Review B*, vol. 63, no. 22, 220403(R), 2001.
- [28] W. Butler, X.-G. Zhang, T. Schulthess, and J. MacLaren, “Spin-dependent tunneling conductance of fe| mgo| fe sandwiches,” *Physical Review B*, vol. 63, no. 5, p. 054 416, 2001, doi: [10.1103/PhysRevB.63.054416](https://doi.org/10.1103/PhysRevB.63.054416).
- [29] A. Quindeau, V. Borisov, I. Fina, S. Ostanin, E. Pippel, I. Mertig, D. Hesse, and M. Alexe, “Origin of tunnel electroresistance effect in pbti o 3-based multiferroic tunnel junctions,” *Physical Review B*, vol. 92, no. 3, p. 035 130, 2015.
- [30] V. S. Borisov, S. Ostanin, S. Achilles, J. Henk, and I. Mertig, “Spin-dependent transport in a multiferroic tunnel junction: Theory for co/pbtio 3/co,” *Physical Review B*, vol. 92, no. 7, p. 075 137, 2015.
- [31] M. Weisheit, S. Fähler, A. Marty, Y. Souche, C. Poinsignon, and D. Givord, “Electric field-induced modification of magnetism in thin-film ferromagnets,” *Science*, vol. 315, no. 5810, pp. 349–351, 2007. DOI: [10.1126/science.1136629](https://doi.org/10.1126/science.1136629).
- [32] S. Papers, “Large voltage-induced magnetic anisotropy change in a few atomic layers of iron,” *Nature nanotechnology*, vol. 161, no. 3, pp. 27–29, 2009.
- [33] L. W. Martin and R. Ramesh, “Multiferroic and magnetoelectric heterostructures,” *Acta Materialia*, vol. 60, no. 6-7, pp. 2449–2470, 2012. DOI: [10.1016/j.actamat.2011.12.024](https://doi.org/10.1016/j.actamat.2011.12.024).

- [34] E. Dagotto, T. Hotta, and A. Moreo, “Colossal magnetoresistant materials: The key role of phase separation,” *Physics reports*, vol. 344, no. 1-3, pp. 1–153, 2001.
- [35] P. G. De Gennes, “Effects of double exchange in magnetic crystals,” *Physical Review*, vol. 118, no. 1, pp. 141–154, 1960, ISSN: 0031899X. DOI: [10.1103/PhysRev.118.141](https://doi.org/10.1103/PhysRev.118.141).
- [36] C. H. Ahn, J. M. Triscone, and J. Mannhart, “Electric field effect in correlated oxide systems,” *Nature*, vol. 424, no. 6952, pp. 1015–1018, 2003. DOI: [10.1038/nature01878](https://doi.org/10.1038/nature01878).
- [37] Y. Moritomo, T. Akimoto, A. Nakamura, K. Ohoyama, and M. Ohashi, “Antiferromagnetic metallic state in the heavily doped region of perovskite manganites,” *Phys. Rev. B*, vol. 58, pp. 5544–5549, 9 Sep. 1998. DOI: [10.1103/PhysRevB.58.5544](https://doi.org/10.1103/PhysRevB.58.5544).
- [38] J. P. Perdew, K. Burke, and M. Ernzerhof, “Generalized gradient approximation made simple,” *Phys. Rev. Lett.*, vol. 77, pp. 3865–3868, 18 Oct. 1996. DOI: [10.1103/PhysRevLett.77.3865](https://doi.org/10.1103/PhysRevLett.77.3865).
- [39] P. Giannozzi, S. Baroni, N. Bonini, M. Calandra, R. Car, C. Cavazzoni, D. Ceresoli, G. L. Chiarotti, M. Cococcioni, I. Dabo, A. Dal Corso, S. de Gironcoli, S. Fabris, G. Fratesi, R. Gebauer, U. Gerstmann, C. Gougoussis, A. Kokalj, M. Lazzeri, L. Martin-Samos, N. Marzari, F. Mauri, R. Mazzarello, S. Paolini, A. Pasquarello, L. Paulatto, C. Sbraccia, S. Scandolo, G. Sciauzero, A. P. Seitsonen, A. Smogunov, P. Umari, and R. M. Wentzcovitch, “QUANTUM ESPRESSO: a modular and open-source software project for quantum simulations of materials,” *Journal of Physics: Condensed Matter*, vol. 21, no. 39, p. 395 502, Sep. 2009. DOI: [10.1088/0953-8984/21/39/395502](https://doi.org/10.1088/0953-8984/21/39/395502). arXiv: [0906.2569](https://arxiv.org/abs/0906.2569).
- [40] D. Vanderbilt, “Soft Self-Consistent Pseudopotential in a Generalized Eigenvalue Formalism,” *Physical Review B*, vol. 41, no. 11, pp. 7892–7895, 1990. DOI: <https://doi.org/10.1103/PhysRevB.41.7892>.
- [41] L. Colombo, R. Resta, and S. Baroni, “Valence-band offsets at strained Si/Ge interfaces,” *Physical Review B*, vol. 44, no. 11, pp. 5572–5579, 1991, ISSN: 01631829. DOI: [10.1103/PhysRevB.44.5572](https://doi.org/10.1103/PhysRevB.44.5572).
- [42] D. Cao, M. Q. Cai, W. Y. Hu, and C. M. Xu, “Magnetoelectric effect and critical thickness for ferroelectricity in Co/BaTiO₃/Co multiferroic tunnel junctions,” *Journal of Applied Physics*, vol. 109, no. 11, 2011, ISSN: 00218979. DOI: [10.1063/1.3587172](https://doi.org/10.1063/1.3587172).
- [43] T. L. Gilbert, “A phenomenological theory of damping in ferromagnetic materials,” *IEEE Transactions on Magnetism*, vol. 40, no. 6, pp. 3443–3449, 2004. DOI: [10.1109/TMAG.2004.836740](https://doi.org/10.1109/TMAG.2004.836740).

- [44] M. D'Aquino, "Nonlinear Magnetization Dynamics in Thin-films and Nanoparticles," Ph.D. dissertation, Universit degli Studi di Napoli Federico II, 2004, p. 155.
- [45] R. F. Evans, W. J. Fan, P. Chureemart, T. A. Ostler, M. O. Ellis, and R. W. Chantrell, "Atomistic spin model simulations of magnetic nanomaterials," *Journal of Physics: Condensed Matter*, vol. 26, no. 10, p. 103 202, 2014.
- [46] W. F. Brown, "Thermal Fluctuations of a Single-Domain Particles," *Phys. Rev.*, vol. 130, no. 1963, p. 1677, 1963. DOI: [10.1103/PhysRev.130.1677](https://doi.org/10.1103/PhysRev.130.1677).
- [47] D. V. Berkov, "Magnetization dynamics including thermal fluctuations: Basic phenomenology, fast remagnetization processes and transitions over high-energy barriers," *Handbook of Magnetism and Advanced Magnetic Materials*, vol. 2, 2007.
- [48] C. W. Gardiner, "Handbook of stochastic methods for physics, chemistry and the natural sciences," *Applied Optics*, vol. 25, p. 3145, 1986.
- [49] W. Scholz, J. Fidler, D. Suess, and T. Schrefl, "Langevin dynamics of small ferromagnetic particles and wires," in *Proceedings of 16th IMACS World Congress on Scientific Computation, Applied Mathematics and Simulation*, 2000.
- [50] D. Datta, B. Behin-aein, S. Salahuddin, and S. Datta, "Voltage Asymmetry of Spin-Transfer Torques," *IEEE Transactions on Nanotechnology*, vol. 11, no. 2, pp. 261–272, 2012, ISSN: 1536-125X. DOI: [10.1109/TNANO.2011.2163147](https://doi.org/10.1109/TNANO.2011.2163147).
- [51] Y. Liu, X. Lou, M. Bibes, and B. Dkhil, "Effect of a built-in electric field in asymmetric ferroelectric tunnel junctions," *Phys. Rev. B*, vol. 88, p. 024 106, 2 Jul. 2013. DOI: [10.1103/PhysRevB.88.024106](https://doi.org/10.1103/PhysRevB.88.024106).
- [52] E.-K. Tan, J. Osman, and D. Tilley, "Theory of Switching in Bulk First-Order Ferroelectric Materials," *physica status solidi (b)*, vol. 228, no. 3, pp. 765–776, Dec. 2001.
- [53] D. Datta, B. Behin-Aein, S. Salahuddin, and S. Datta, "Quantitative model for tnr and spin-transfer torque in mtj devices," in *Electron Devices Meeting (IEDM), 2010 IEEE International*, IEEE, 2010, pp. 22–8.
- [54] D. J. Griffiths and D. F. Schroeter, *Introduction to quantum mechanics*. Cambridge University Press, 2018.
- [55] A. Gruverman, D. Wu, H. Lu, Y. Wang, H. Jang, C. Folkman, M. Y. Zhuravlev, D. Felker, M. Rzchowski, C.-B. Eom, *et al.*, "Tunneling electroresistance effect in ferroelectric tunnel junctions at the nanoscale," *Nano letters*, vol. 9, no. 10, pp. 3539–3543, 2009.

- [56] R. Andrawis and K. Roy, “Antiferroelectric tunnel junctions as energy-efficient coupled oscillators: Modeling, analysis, and application to solving combinatorial optimization problems,” *IEEE Transactions on Electron Devices*, vol. 67, no. 7, pp. 2974–2980, 2020.
- [57] J. K. Lenstra and A. R. Kan, “Computational complexity of discrete optimization problems,” in *Annals of Discrete Mathematics*, vol. 4, Elsevier, 1979, pp. 121–140.
- [58] T. N. Theis and P. M. Solomon, “In quest of the “next switch”: Prospects for greatly reduced power dissipation in a successor to the silicon field-effect transistor,” *Proceedings of the IEEE*, vol. 98, no. 12, pp. 2005–2014, 2010.
- [59] E. M. Izhikevich, “Weakly pulse-coupled oscillators, fm interactions, synchronization, and oscillatory associative memory,” *IEEE Transactions on Neural Networks*, vol. 10, no. 3, pp. 508–526, 1999.
- [60] J. Wu, L. Jiao, R. Li, and W. Chen, “Clustering dynamics of nonlinear oscillator network: Application to graph coloring problem,” *Physica D: Nonlinear Phenomena*, vol. 240, no. 24, pp. 1972–1978, 2011.
- [61] G. Apachitei, J. J. Peters, A. M. Sanchez, D. J. Kim, and M. Alexe, “Antiferroelectric Tunnel Junctions,” *Advanced Electronic Materials*, vol. 3, no. 7, pp. 3–7, 2017, ISSN: 2199160X. DOI: [10.1002/aelm.201700126](https://doi.org/10.1002/aelm.201700126).
- [62] A. Parihar, N. Shukla, M. Jerry, S. Datta, and A. Raychowdhury, “Vertex coloring of graphs via phase dynamics of coupled oscillatory networks,” *Scientific reports*, vol. 7, no. 1, p. 911, 2017.
- [63] A. Sharma, Y. Kesim, M. Shulaker, C. Kuo, C. Augustine, H.-P. Wong, S. Mitra, M. Skowronski, J. Bain, and J. Weldon, “Low-power, high-performance s-ndr oscillators for stereo (3d) vision using directly-coupled oscillator networks,” in *2016 IEEE Symposium on VLSI Technology*, IEEE, 2016, pp. 1–2.
- [64] M. D. Pickett and R. S. Williams, “Sub-100 fj and sub-nanosecond thermally driven threshold switching in niobium oxide crosspoint nanodevices,” *Nanotechnology*, vol. 23, no. 21, p. 215 202, 2012.
- [65] C. Kittel, “Theory of antiferroelectric crystals,” *Physical Review*, vol. 82, no. 5, p. 729, 1951.
- [66] R. H. Fowler and L. Nordheim, “Electron emission in intense electric fields,” *Proceedings of the Royal Society of London. Series A, Containing Papers of a Mathematical and Physical Character*, vol. 119, no. 781, pp. 173–181, 1928.

- [67] L. H. Thomas, “The calculation of atomic fields,” in *Mathematical Proceedings of the Cambridge Philosophical Society*, Cambridge University Press, vol. 23, 1927, pp. 542–548.
- [68] W. A. Harrison, “Tunneling from an independent-particle point of view,” *Physical Review*, vol. 123, no. 1, p. 85, 1961.
- [69] R. Clerc, A. Spinelli, G. Ghibaudo, and G. Pananakakis, “Theory of direct tunneling current in metal–oxide–semiconductor structures,” *Journal of applied physics*, vol. 91, no. 3, pp. 1400–1409, 2002.
- [70] W. Brinkman, R. Dynes, and J. Rowell, “Tunneling conductance of asymmetrical barriers,” *Journal of applied physics*, vol. 41, no. 5, pp. 1915–1921, 1970.
- [71] S. H. Strogatz, *Nonlinear Dynamics and Chaos with Student Solutions Manual: With Applications to Physics, Biology, Chemistry, and Engineering*. CRC Press, 2018.
- [72] D. J. Johnson and M. A. Trick, Eds., *Cliques, Coloring, and Satisfiability: Second DIMACS Implementation Challenge, Workshop, October 11-13, 1993*. Boston, MA, USA: American Mathematical Society, 1996, ISBN: 0821866095.
- [73] R. Andrawis and K. Roy, “A new oscillator coupling function for improving the solution of graph coloring problem,” *Physica D: Nonlinear Phenomena*, vol. 412, p. 132617, 2020.
- [74] V. V. Zhirnov, R. K. Cavin, J. A. Hutchby, and G. I. Bourianoff, “Limits to binary logic switch scaling—a gedanken model,” *Proceedings of the IEEE*, vol. 91, no. 11, pp. 1934–1939, 2003.
- [75] J. A. Acebrón, L. L. Bonilla, C. J. P. Vicente, F. Ritort, and R. Spigler, “The kuramoto model: A simple paradigm for synchronization phenomena,” *Reviews of modern physics*, vol. 77, no. 1, p. 137, 2005.
- [76] Y. Kuramoto, *Chemical oscillations, waves, and turbulence*. Courier Corporation, 2003.
- [77] H. Sakaguchi and Y. Kuramoto, “A soluble active rotator model showing phase transitions via mutual entertainment,” *Progress of Theoretical Physics*, vol. 76, no. 3, pp. 576–581, 1986.
- [78] S. H. Strogatz, “From kuramoto to crawford: Exploring the onset of synchronization in populations of coupled oscillators,” *Physica D: Nonlinear Phenomena*, vol. 143, no. 1-4, pp. 1–20, 2000.

- [79] C. W. Wu, "Graph coloring via synchronization of coupled oscillators," *IEEE Transactions on Circuits and Systems I: Fundamental Theory and Applications*, vol. 45, no. 9, pp. 974–978, 1998.
- [80] D. B. West *et al.*, *Introduction to graph theory*. Prentice hall Upper Saddle River, NJ, 1996, vol. 2.
- [81] F. T. Leighton, "A graph coloring algorithm for large scheduling problems," *Journal of research of the national bureau of standards*, vol. 84, no. 6, pp. 489–506, 1979.
- [82] S. B. Akers, "Fault diagnosis as a graph coloring problem," *IEEE Transactions on Computers*, vol. 100, no. 7, pp. 706–713, 1974.
- [83] N. Zufferey, P. Amstutz, and P. Giaccari, "Graph colouring approaches for a satellite range scheduling problem," *Journal of Scheduling*, vol. 11, no. 4, pp. 263–277, 2008.
- [84] Z. Xizheng and W. Yaonan, "New mixed broadcast scheduling approach using neural networks and graph coloring in wireless sensor network," *Journal of Systems Engineering and Electronics*, vol. 20, no. 1, pp. 185–191, 2009.
- [85] T.-K. Woo, S. Y. Su, and R. Newman-Wolfe, "Resource allocation in a dynamically partitionable bus network using a graph coloring algorithm," *IEEE Transactions on Communications*, vol. 39, no. 12, pp. 1794–1801, 1991.
- [86] A. Jaiswal, R. Andrawis, and K. Roy, "Area-efficient nonvolatile flip-flop based on spin hall effect," *IEEE Magnetics Letters*, vol. 9, pp. 1–4, 2018.
- [87] "[online]. available: [Http://www.itrs.net/](http://www.itrs.net/),"
- [88] L. Atzori, A. Iera, and G. Morabito, "The internet of things: A survey," *Computer networks*, vol. 54, no. 15, pp. 2787–2805, 2010.
- [89] L. Wang, C. H. Yang, and J. Wen, "Physical principles and current status of emerging non-volatile solid state memories," *Electronic Materials Letters*, vol. 11, no. 4, pp. 505–543, 2015. DOI: [10.1007/s13391-015-4431-4](https://doi.org/10.1007/s13391-015-4431-4).
- [90] X. Deng and Y. Mo, "Boost bulk-driven sense-amplifier flip-flop operating in ultra-wide voltage range," *Electronics Letters*, vol. 51, no. 9, pp. 680–682, 2015, ISSN: 0013-5194. DOI: [10.1049/el.2014.3845](https://doi.org/10.1049/el.2014.3845).
- [91] N. Sakimura, T. Sugibayashi, R. Nebashi, and N. Kasai, "Nonvolatile magnetic flip-flop for standby-power-free socs," *IEEE Journal of Solid-State Circuits*, vol. 44, no. 8, pp. 2244–2250, 2009.

- [92] D. Chabi, W. Zhao, E. Deng, Y. Zhang, N. B. Romdhane, J.-O. Klein, and C. Chappert, "Ultra low power magnetic flip-flop based on checkpointing/power gating and self-enable mechanisms," *IEEE Transactions on Circuits and Systems I: Regular Papers*, vol. 61, no. 6, pp. 1755–1765, 2014.
- [93] K. Jabeur, G. Di Pendina, F. Bernard-Granger, and G. Prenat, "Spin orbit torque non-volatile flip-flop for high speed and low energy applications," *IEEE Electron Device Letters*, vol. 35, no. 3, pp. 408–410, 2014.
- [94] H. Noguchi, K. Ikegami, K. Abe, S. Fujita, Y. Shiota, T. Nozaki, S. Yuasa, and Y. Suzuki, "Novel voltage controlled MRAM (VCM) with fast read/write circuits for ultra large last level cache," in *2016 IEEE International Electron Devices Meeting (IEDM)*, IEEE, 2016, pp. 27.5.1–27.5.4. DOI: [10.1109/IEDM.2016.7838494](https://doi.org/10.1109/IEDM.2016.7838494).
- [95] L. Liu, C.-F. Pai, Y. Li, H. Tseng, D. Ralph, and R. Buhrman, "Spin-torque switching with the giant spin hall effect of Tantalum," *Science*, vol. 336, no. 6081, pp. 555–558, 2012, doi: [10.1126/science.1218197](https://doi.org/10.1126/science.1218197).
- [96] A. Lee, C.-P. Lo, C.-C. Lin, W.-H. Chen, K.-H. Hsu, Z. Wang, F. Su, Z. Yuan, Q. Wei, Y.-C. King, C.-J. Lin, H. Lee, P. Khalili Amiri, K.-L. Wang, Y. Wang, H. Yang, Y. Liu, and M.-F. Chang, "A ReRAM-Based Nonvolatile Flip-Flop With Self-Write-Termination Scheme for Frequent-OFF Fast-Wake-Up Nonvolatile Processors," *IEEE Journal of Solid-State Circuits*, vol. 52, no. 8, pp. 2194–2207, 2017, ISSN: 0018-9200. DOI: [10.1109/JSSC.2017.2700788](https://doi.org/10.1109/JSSC.2017.2700788).
- [97] H. B. Kang, *Phase change resistor cell and nonvolatile memory device using the same*, US Patent 7,038,938, May 2006.
- [98] W. Zhao, E. Belhaire, and C. Chappert, "Spin-MTJ based non-volatile flip-flop," in *IEEE-NANO 2007. 7th IEEE Conference on*, IEEE, 2007, pp. 399–402.
- [99] K. W. Kwon, S. H. Choday, Y. Kim, X. Fong, S. P. Park, and K. Roy, "SHE-NVFF: Spin hall effect-based nonvolatile flip-flop for power gating architecture," *IEEE Electron Device Letters*, vol. 35, no. 4, pp. 488–490, 2014. DOI: [10.1109/LED.2014.2304683](https://doi.org/10.1109/LED.2014.2304683).
- [100] W. Kang, Y. Ran, W. Lv, Y. Zhang, and W. Zhao, "High-speed, low-power, magnetic non-volatile flip-flop with voltage-controlled, magnetic anisotropy assistance," *IEEE Magnetism Letters*, vol. 7, pp. 1–5, 2016.
- [101] Y. Seo, X. Fong, and K. Roy, "Fast and Disturb-Free Nonvolatile Flip-Flop Using Complementary Polarizer MTJ," *IEEE Transactions on Very Large Scale Integration (VLSI) Systems*, vol. 25, no. 4, pp. 1573–1577, 2017, ISSN: 1063-8210. DOI: [10.1109/TVLSI.2016.2631981](https://doi.org/10.1109/TVLSI.2016.2631981).

- [102] L. Qu, Z. Zhao, Y. Wang, H. Li, H. Tang, Q. Deng, and P. Li, “High-speed disturbance-free nonvolatile flip-flop based on complementary polarizers,” in *Electron Devices and Solid-State Circuits (EDSSC), 2016 IEEE International Conference on*, IEEE, 2016, pp. 169–172.
- [103] Z. Wang, L. Zhang, M. Wang, Z. Wang, D. Zhu, Y. Zhang, and W. Zhao, “High-Density NAND-Like Spin Transfer Torque Memory With Spin Orbit Torque Erase Operation,” *IEEE Electron Device Letters*, vol. 39, no. 3, pp. 343–346, 2018, ISSN: 0741-3106. DOI: [10.1109/LED.2018.2795039](https://doi.org/10.1109/LED.2018.2795039).
- [104] T. Na, K. Ryu, J. Kim, S.-O. Jung, J. P. Kim, and S. H. Kang, “High-performance low-power magnetic tunnel junction based non-volatile flip-flop,” in *Circuits and Systems (ISCAS), 2014 IEEE International Symposium on*, IEEE, 2014, pp. 1953–1956.
- [105] M. Dyakonov, “Spin hall effect,” *International Journal of Modern Physics B*, vol. 23, no. 12n13, pp. 2556–2565, 2009.
- [106] Y. Kim, S. H. Choday, and K. Roy, “Dsh-mram: Differential spin hall mram for on-chip memories,” *IEEE Electron Device Letters*, vol. 34, no. 10, pp. 1259–1261, Oct. 2013, ISSN: 0741-3106. DOI: [10.1109/LED.2013.2279153](https://doi.org/10.1109/LED.2013.2279153).
- [107] S. Ikeda, K. Miura, H. Yamamoto, K. Mizunuma, H. Gan, M. Endo, S. Kanai, J. Hayakawa, F. Matsukura, and H. Ohno, “A perpendicular-anisotropy cobe–mgo magnetic tunnel junction,” *Nature materials*, vol. 9, no. 9, pp. 721–724, 2010.
- [108] X. Fong, S. K. Gupta, N. N. Mojumder, S. H. Choday, C. Augustine, and K. Roy, “KNACK: A hybrid spin-charge mixed-mode simulator for evaluating different genres of spin-transfer torque MRAM bit-cells,” in *International Conference on Simulation of Semiconductor Processes and Devices, SISPAD*, 2011, pp. 51–54, ISBN: 9781612844169. DOI: [10.1109/SISPAD.2011.6035047](https://doi.org/10.1109/SISPAD.2011.6035047).
- [109] A. Jaiswal, X. Fong, and K. Roy, “Comprehensive scaling analysis of current induced switching in magnetic memories based on in-plane and perpendicular anisotropies,” *IEEE Journal on Emerging and Selected Topics in Circuits and Systems*, vol. 6, no. 2, pp. 120–133, 2016.
- [110] S. Mukhopadhyay, H. Mahmoodi, and K. Roy, “Modeling of failure probability and statistical design of sram array for yield enhancement in nanoscaled cmos,” *IEEE transactions on computer-aided design of integrated circuits and systems*, vol. 24, no. 12, pp. 1859–1880, 2005.
- [111] Q.-K. K. Trinh, S. Ruocco, and M. Alioto, “Dynamic Reference Voltage Sensing Scheme for Read Margin Improvement in STT-MRAMs,” *IEEE Transactions on Circuits and Systems I: Regular Papers*, vol. 65, no. 4, pp. 1269–1278, 2018, ISSN: 15498328. DOI: [10.1109/TCSI.2017.2749522](https://doi.org/10.1109/TCSI.2017.2749522).

- [112] W. Zhao and Y. Cao, “New generation of predictive technology model for sub-45 nm early design exploration,” *IEEE Transactions on Electron Devices*, vol. 53, no. 11, pp. 2816–2823, 2006.
- [113] J. P. Duarte, S. Khandelwal, A. Medury, C. Hu, P. Kushwaha, H. Agarwal, A. Dasgupta, and Y. S. Chauhan, “Bsim-cmg: Standard finfet compact model for advanced circuit design,” in *European Solid-State Circuits Conference (ESSCIRC), ESSCIRC 2015-41st*, IEEE, 2015, pp. 196–201.
- [114] K.-W. Kwon, X. Fong, P. Wijesinghe, P. Panda, and K. Roy, “High-density and robust stt-mram array through device/circuit/architecture interactions,” *IEEE Transactions on Nanotechnology*, vol. 14, no. 6, pp. 1024–1034, 2015.
- [115] S. K. Gupta, S. P. Park, N. N. Mojumder, and K. Roy, “Layout-aware optimization of stt mrams,” in *Proceedings of the Conference on Design, Automation and Test in Europe*, EDA Consortium, 2012, pp. 1455–1458.
- [116] A. Jaiswal, R. Andrawis, A. Agrawal, and K. Roy, “Functional read enabling in-memory computations in 1transistor-1resistor memory arrays,” *IEEE Transactions on Circuits and Systems II: Express Briefs*, 2020.
- [117] M. M. Waldrop, “The chips are down for moore’s law,” *Nature News*, vol. 530, no. 7589, p. 144, 2016.
- [118] S. Borkar and A. A. Chien, “The future of microprocessors,” *Communications of the ACM*, vol. 54, no. 5, pp. 67–77, 2011.
- [119] J. M. Shalf and R. Leland, “Computing beyond moore’s law,” *Computer*, vol. 48, no. 12, pp. 14–23, 2015.
- [120] A. Chen, “A review of emerging non-volatile memory (nvm) technologies and applications,” *Solid-State Electronics*, vol. 125, pp. 25–38, 2016.
- [121] H.-S. P. Wong and S. Salahuddin, “Memory leads the way to better computing,” *Nature nanotechnology*, vol. 10, no. 3, p. 191, 2015.
- [122] P. G. Emma, “Understanding some simple processor-performance limits,” *IBM Journal of Research and Development*, vol. 41, no. 3, pp. 215–232, May 1997, ISSN: 0018-8646. DOI: [10.1147/rd.413.0215](https://doi.org/10.1147/rd.413.0215).
- [123] H. Noguchi, K. Ikegami, N. Shimomura, T. Tetsufumi, J. Ito, and S. Fujita, “Highly reliable and low-power nonvolatile cache memory with advanced perpendicular stt-mram for high-performance cpu,” in *VLSI Circuits Digest of Technical Papers, 2014 Symposium on*, IEEE, 2014, pp. 1–2.

- [124] H. Noguchi, K. Ikegami, K. Kushida, K. Abe, S. Itai, S. Takaya, N. Shimomura, J. Ito, A. Kawasumi, H. Hara, *et al.*, “7.5 a 3.3 ns-access-time 71.2 μ W/MHz 1Mb embedded stt-mram using physically eliminated read-disturb scheme and normally-off memory architecture,” in *Solid-State Circuits Conference-(ISSCC), 2015 IEEE International*, IEEE, 2015, pp. 1–3.
- [125] A. Agrawal, A. Jaiswal, C. Lee, and K. Roy, “X-sram: Enabling in-memory boolean computations in cmos static random access memories,” *IEEE Transactions on Circuits and Systems I: Regular Papers*, no. 99, pp. 1–14, 2018.
- [126] S. Jain, A. Ranjan, K. Roy, and A. Raghunathan, “Computing in memory with spin-transfer torque magnetic ram,” *IEEE Transactions on Very Large Scale Integration (VLSI) Systems*, vol. 26, no. 3, pp. 470–483, Mar. 2018, ISSN: 1063-8210. DOI: [10.1109/TVLSI.2017.2776954](https://doi.org/10.1109/TVLSI.2017.2776954).
- [127] A. Grossi, E. Nowak, C. Zambelli, C. Pellissier, S. Bernasconi, G. Cibrario, K. E. Hajjam, R. Crochemore, J. F. Nodin, P. Olivo, and L. Perniola, “Fundamental variability limits of filament-based rram,” in *2016 IEEE International Electron Devices Meeting (IEDM)*, Dec. 2016, pp. 4.7.1–4.7.4. DOI: [10.1109/IEDM.2016.7838348](https://doi.org/10.1109/IEDM.2016.7838348).
- [128] C. Lin, S. Kang, Y. Wang, K. Lee, X. Zhu, W. Chen, X. Li, W. Hsu, Y. Kao, M. Liu, *et al.*, “45nm low power cmos logic compatible embedded stt mram utilizing a reverse-connection 1T/1MTJ cell,” in *Electron Devices Meeting (IEDM), 2009 IEEE International*, IEEE, 2009, pp. 1–4.
- [129] Y. Zhang, Y. Li, Z. Sun, H. Li, Y. Chen, and A. K. Jones, “Read performance: The newest barrier in scaled stt-ram,” *IEEE Transactions on Very Large Scale Integration (VLSI) Systems*, vol. 23, no. 6, pp. 1170–1174, 2015.
- [130] L. Liu, O. Lee, T. Gudmundsen, D. Ralph, and R. Buhrman, “Current-induced switching of perpendicularly magnetized magnetic layers using spin torque from the spin hall effect,” *Physical review letters*, vol. 109, no. 9, p. 096 602, 2012, doi: [10.1103/PhysRevLett.109.096602](https://doi.org/10.1103/PhysRevLett.109.096602).
- [131] J. G. Alzate, P. K. Amiri, P. Upadhyaya, S. S. Cherepov, J. Zhu, M. Lewis, R. Dorrance, J. A. Katine, J. Langer, K. Galatsis, D. Markovic, I. Krivorotov, and K. L. Wang, “Voltage-induced switching of nanoscale magnetic tunnel junctions,” in *Technical Digest - International Electron Devices Meeting, IEDM*, 2012, pp. 29.5.1–29.5.4, ISBN: 9781467348706. DOI: [10.1109/IEDM.2012.6479130](https://doi.org/10.1109/IEDM.2012.6479130).
- [132] Y. H. Chu, L. W. Martin, M. B. Holcomb, M. Gajek, S. J. Han, Q. He, N. Balke, C. H. Yang, D. Lee, W. Hu, Q. Zhan, P. L. Yang, A. Fraile-Rodríguez, A. Scholl, S. X. Wang, and R. Ramesh, “Electric-field control of local ferromagnetism using a magnetoelectric multiferroic,” *Nature Materials*, 2008. DOI: [10.1038/nmat2184](https://doi.org/10.1038/nmat2184).

- [133] J. Kim, H. Zhao, Y. Jiang, A. Klemm, J. P. Wang, and C. H. Kim, "Scaling analysis of in-plane and perpendicular anisotropy magnetic tunnel junctions using a physics-based model," in *Device Research Conference - Conference Digest, DRC*, IEEE, Jun. 2014, pp. 155–156. DOI: [10.1109/DRC.2014.6872344](https://doi.org/10.1109/DRC.2014.6872344).
- [134] S. Sharmin, A. Jaiswal, and K. Roy, "Modeling and design space exploration for bit-cells based on voltage-assisted switching of magnetic tunnel junctions," *IEEE Transactions on Electron Devices*, vol. 63, no. 9, pp. 3493–3500, 2016.
- [135] A. Jaiswal, I. Chakraborty, and K. Roy, "Energy-efficient memories using magnetoelectric switching of ferromagnets," *IEEE Magnetism Letters*, 2017.
- [136] J. Kim, B. Tuohy, C. Ma, W. H. Choi, I. Ahmed, D. Lilja, and C. H. Kim, "Spin-hall effect mram based cache memory: A feasibility study," in *Device Research Conference (DRC), 2015 73rd Annual*, IEEE, 2015, pp. 117–118.
- [137] S. Wang, H. Lee, F. Ebrahimi, P. K. Amiri, K. L. Wang, and P. Gupta, "Comparative evaluation of spin-transfer-torque and magnetoelectric random access memory," *IEEE Journal on Emerging and Selected Topics in Circuits and Systems*, vol. 6, no. 2, pp. 134–145, 2016, doi: [10.1109/JETCAS.2016.2547681](https://doi.org/10.1109/JETCAS.2016.2547681).
- [138] R. Andrawis, A. Jaiswal, and K. Roy, "Design and comparative analysis of spintronic memories based on current and voltage driven switching," *IEEE Transactions on Electron Devices*, vol. 65, no. 7, pp. 2682–2693, 2018.
- [139] P. Bruno, "Physical origins and theoretical models of magnetic anisotropy," *Magnetismus von Festkörpern und grenzflächen*, vol. 24, pp. 1–28, 1993.
- [140] J. C. Slonczewski, "Conductance and exchange coupling of two ferromagnets separated by a insulating barrier, J.Slonczewski, PRB(1989).pdf," *Physical Review B*, vol. 39, no. 10, pp. 6995–7002, 1989.
- [141] X. Fong, Y. Kim, R. Venkatesan, S. H. Choday, A. Raghunathan, and K. Roy, "Spin-transfer torque memories: Devices, circuits, and systems," *Proceedings of the IEEE*, vol. 104, no. 7, pp. 1449–1488, 2016.
- [142] R. Koch, J. Katine, and J. Sun, "Time-resolved reversal of spin-transfer switching in a nanomagnet," *Physical review letters*, vol. 92, no. 8, p. 088 302, 2004.
- [143] J. Slonczewski, "Current-driven excitation of magnetic multilayers," *Journal of Magnetism and Magnetic Materials*, vol. 159, no. 1, pp. L1–L7, 1996, issn: 0304-8853.
- [144] E. C. Stoner and E. P. Wohlfarth, "A mechanism of magnetic hysteresis in heterogeneous alloys," *IEEE Transactions on Magnetism*, vol. 27, no. 4, pp. 3475–3518, 1991. DOI: [10.1109/TMAG.1991.1183750](https://doi.org/10.1109/TMAG.1991.1183750).

- [145] Z. Wang, G. Yu, X. Liu, B. Zhang, X. Chen, and W. Lu, “Magnetization characteristic of ferromagnetic thin strip by measuring anisotropic magnetoresistance and ferromagnetic resonance,” *Solid State Communications*, 2014, ISSN: 00381098. DOI: [10.1016/j.ssc.2013.11.034](https://doi.org/10.1016/j.ssc.2013.11.034).
- [146] J. Xiao, A. Zangwill, and M. D. Stiles, “Boltzmann test of slonczewski’s theory of spin-transfer torque,” *Physical Review B*, vol. 70, no. 17, p. 172 405, 2004.
- [147] M. Beleggia, M. De Graef, Y. Millev, D. Goode, and G. Rowlands, “Demagnetization factors for elliptic cylinders,” *Journal of Physics D: Applied Physics*, vol. 38, no. 18, p. 3333, 2005.
- [148] J. Velev, S. Jaswal, and E. Tsymbal, “Multi-ferroic and magnetoelectric materials and interfaces,” *Philosophical Transactions of the Royal Society of London A: Mathematical, Physical and Engineering Sciences*, vol. 369, no. 1948, pp. 3069–3097, 2011.
- [149] J. G. Alzate, P. Khalili Amiri, G. Yu, P. Upadhyaya, J. A. Katine, J. Langer, B. Ocker, I. N. Krivorotov, and K. L. Wang, “Temperature dependence of the voltage-controlled perpendicular anisotropy in nanoscale mgo|cofeb|ta magnetic tunnel junctions,” *Applied Physics Letters*, vol. 104, no. 11, p. 112 410, 2014, doi: [10.1063/1.4869152](https://doi.org/10.1063/1.4869152).
- [150] D. S. Matic, “A magnetic tunnel junction compact model for stt-ram and meram,” *Project for Master of Science in Electrical Engineering, UCLA*, 2013.
- [151] R. Dorrance, J. G. Alzate, S. S. Cherepov, P. Upadhyaya, I. N. Krivorotov, J. A. Katine, J. Langer, K. L. Wang, P. K. Amiri, and D. Marković, “Diode-mtj crossbar memory cell using voltage-induced unipolar switching for high-density mram,” *IEEE Electron Device Letters*, vol. 34, no. 6, pp. 753–755, 2013, doi: [10.1109/LED.2013.2255096](https://doi.org/10.1109/LED.2013.2255096).
- [152] S. Kanai, Y. Nakatani, M. Yamanouchi, S. Ikeda, H. Sato, F. Matsukura, and H. Ohno, “Magnetization switching in a cofeb/mgo magnetic tunnel junction by combining spin-transfer torque and electric field-effect,” *Applied Physics Letters*, vol. 104, no. 21, p. 212 406, 2014.
- [153] S. Manipatruni, D. E. Nikonov, and I. A. Young, “Energy-delay performance of giant spin hall effect switching for dense magnetic memory,” *Applied Physics Express*, vol. 7, no. 10, p. 103 001, 2014.
- [154] M. D’yakonov and V. Perel, “Possibility of orienting electron spins with current,” *Soviet Journal of Experimental and Theoretical Physics Letters*, vol. 13, p. 467, 1971.
- [155] J. Hirsch, “Spin hall effect,” *Physical Review Letters*, vol. 83, no. 9, p. 1834, 1999.
- [156] I. M. Miron, K. Garello, G. Gaudin, P.-J. Zermatten, M. V. Costache, S. Auffret, S. Bandiera, B. Rodmacq, A. Schuhl, and P. Gambardella, “Perpendicular switching of

- a single ferromagnetic layer induced by in-plane current injection,” *Nature*, vol. 476, no. 7359, p. 189, 2011, doi: [10.1038/nature10309](https://doi.org/10.1038/nature10309).
- [157] M. Kazemi, G. E. Rowlands, S. Shi, R. A. Buhrman, and E. G. Friedman, “All-spin-orbit switching of perpendicular magnetization,” *IEEE Transactions on Electron Devices*, vol. 63, no. 11, pp. 4499–4505, 2016, doi: [10.1109/TED.2016.2604215](https://doi.org/10.1109/TED.2016.2604215).
 - [158] S. Manipatruni, D. Nikonov, and I. Young, *Mtj spin hall mram bit-cell and array*, US Patent 9,620,188, Apr. 2017.
 - [159] M. Fiebig, “Revival of the magnetoelectric effect,” *Journal of Physics D: Applied Physics*, vol. 38, no. 8, R123, 2005.
 - [160] S. Z. Wu, J. Miao, X. G. Xu, W. Yan, R. Reeve, X. H. Zhang, and Y. Jiang, “Strain-mediated electric-field control of exchange bias in a Co₉₀Fe₁₀/BiFeO₃/SrRuO₃/PMN-PT heterostructure,” *Scientific Reports*, vol. 5, 2015. DOI: [10.1038/srep08905](https://doi.org/10.1038/srep08905).
 - [161] J. Heron, J. Bosse, Q. He, Y. Gao, M. Trassin, L. Ye, J. Clarkson, C. Wang, J. Liu, S. Salahuddin, *et al.*, “Deterministic switching of ferromagnetism at room temperature using an electric field,” *Nature*, vol. 516, no. 7531, p. 370, 2014.
 - [162] A. Jaiswal, I. Chakraborty, and K. Roy, “A non-volatile cascable magneto-electric material implication logic,” in *Device Research Conference (DRC), 2017 75th Annual*, IEEE, 2017, pp. 1–2.
 - [163] W. Eerenstein, N. Mathur, and J. F. Scott, “Multiferroic and magnetoelectric materials,” *nature*, vol. 442, no. 7104, p. 759, 2006.
 - [164] W. Zhao, C. Chappert, V. Javerliac, and J.-P. Noziere, “High speed, high stability and low power sensing amplifier for MTJ/CMOS hybrid logic circuits,” *IEEE Transactions on Magnetism*, vol. 45, no. 10, pp. 3784–3787, 2009, ISSN: 0018-9464.
 - [165] E. K. Au, W.-H. Ki, W. H. Mow, S. T. Hung, and C. Y. Wong, “A novel current-mode sensing scheme for magnetic tunnel junction mram,” *IEEE transactions on magnetism*, vol. 40, no. 2, pp. 483–488, 2004.
 - [166] T. Na, J. Kim, J. P. Kim, S. H. Kang, and S.-O. Jung, “An offset-canceling triple-stage sensing circuit for deep submicrometer stt-ram,” *IEEE Transactions on Very Large Scale Integration (VLSI) Systems*, vol. 22, no. 7, pp. 1620–1624, 2014.
 - [167] D. Halupka, S. Huda, W. Song, A. Sheikholeslami, K. Tsunoda, C. Yoshida, and M. Aoki, “Negative-resistance read and write schemes for stt-mram in 0.13 μm cmos,” in *Solid-State Circuits Conference Digest of Technical Papers (ISSCC), 2010 IEEE International*, IEEE, 2010, pp. 256–257.

- [168] C.-T. Cheng, Y.-C. Tsai, and K.-H. Cheng, “A high-speed current mode sense amplifier for spin-torque transfer magnetic random access memory,” in *Circuits and Systems (MWSCAS), 2010 53rd IEEE International Midwest Symposium on*, IEEE, 2010, pp. 181–184.
- [169] H. Noguchi, K. Kushida, K. Ikegami, K. Abe, E. Kitagawa, S. Kashiwada, C. Kamata, A. Kawasumi, H. Hara, and S. Fujita, “A 250-mhz 256b-i/o 1-mb stt-mram with advanced perpendicular mtj based dual cell for nonvolatile magnetic caches to reduce active power of processors,” in *VLSI Technology (VLSIT), 2013 Symposium on*, IEEE, 2013, pp. C108–C109.

VITA

Robert Andrawis, received his B.S. degree and M.S. degree from the Department of Electrical and Computer Engineering, Cairo University. Obtained a second M.S. degree in Physics from American University in Cairo (AUC) in 2013. He worked as R&D engineer in following places: Valeo, Vodafone and Intel Egypt. He also worked as teaching assistant at American University in Cairo. He joined Nano-electronics Research Lab in the Fall of 2016. His research interest is modeling and simulation of multiferroic and semiconductor devices.